

Electronic Thesis and Dissertation Repository

4-6-2021 2:00 PM

Ischemic Stroke Thrombus Characterization through Quantitative Magnetic Resonance Imaging

Spencer D. Christiansen, *The University of Western Ontario*

Supervisor: Drangova, Maria, *The University of Western Ontario*

A thesis submitted in partial fulfillment of the requirements for the Doctor of Philosophy degree in Medical Biophysics

© Spencer D. Christiansen 2021

Follow this and additional works at: <https://ir.lib.uwo.ca/etd>



Part of the [Biophysics Commons](#)

Recommended Citation

Christiansen, Spencer D., "Ischemic Stroke Thrombus Characterization through Quantitative Magnetic Resonance Imaging" (2021). *Electronic Thesis and Dissertation Repository*. 7737.
<https://ir.lib.uwo.ca/etd/7737>

This Dissertation/Thesis is brought to you for free and open access by Scholarship@Western. It has been accepted for inclusion in Electronic Thesis and Dissertation Repository by an authorized administrator of Scholarship@Western. For more information, please contact wlsadmin@uwo.ca.

Abstract

Stroke is a pervasive, devastating disease and remains one of the most challenging conditions to treat. In particular, risk of recurrence is dramatically heightened after a primary stroke and requires urgent preventative therapy to effectively mitigate. However, the appropriate preventative therapy depends on the underlying source of the stroke, known as etiology, which is challenging to determine promptly. Current diagnostic tests for determining etiology underwhelm in both sensitivity and specificity, and in as much as 35% of cases etiology is never determined. In ischemic stroke, the composition of the occluding thrombus, specifically its red blood cell (RBC) content, has been shown to be indicative of etiology but remains largely ignored within clinical practice. Currently, composition can only be quantified through histological analysis, an involved process that can be completed in only the minority of cases where a thrombus has been physically retrieved from the patient during treatment.

The goal of this thesis is to develop a quantitative MR imaging method which is capable of non-invasive prediction of ischemic stroke etiology through assessment of thrombus RBC content. To achieve this goal, we employed quantitative MR parameters that are sensitive to both RBC content and oxygenation, R_2^* and quantitative susceptibility mapping (QSM), as well as fat fraction (FF) mapping, and evaluated the ability of modern artificial intelligence techniques to form predictions of RBC content and etiology based on these quantitative MR parameters alone and in combination with patient clinical data.

First, we performed an *in vitro* blood clot imaging experiment, which sought to explicitly define the relationship between clot RBC content, oxygenation and our quantitative MR parameters. We show that both R_2^* and QSM are

sensitive to RBC content and oxygenation, as expected, and that the relationship between R_2^* and QSM can be used to predict clot RBC content independent of oxygenation status, a necessary step for stroke thrombus characterization where oxygenation is an unknown quantity.

Second, we trained a deep convolutional neural network to predict histological RBC content from *ex vivo* MR images of ischemic stroke thrombi. We demonstrate that a convolutional neural network is capable of RBC content prediction with 66% accuracy and 8% mean absolute error when trained on a limited thrombus dataset, and that prediction accuracy can be improved to up to 74% through data augmentation.

Finally, we used a random forest classifier to predict clinical stroke etiology using the same *ex vivo* thrombus MR image dataset. Here, quantitative thrombus R_2^* , QSM and FF image texture features were used to train the classifier, and we demonstrate that this method is capable of accurate etiology prediction from thrombus texture information alone (accuracy = 67%, area under the curve (AUC) = 0.68), but that when combined with patient clinical data the performance of the classifier improves dramatically to an accuracy and AUC of 93% and 0.89, respectively.

Together, the works presented in this thesis offer extensive *ex vivo* evidence that quantitative MR imaging is capable of effective stroke thrombus etiology characterization. Such a technique could enable clinical consideration of thrombus composition and bolster stroke etiology determination, thereby improving the management and care of acute ischemic stroke patients.

Keywords

Magnetic Resonance Imaging, Stroke, Thrombus, Quantitative Imaging, Machine Learning, Deep Learning

Lay Summary

Stroke is a devastating and prevalent disease. One of the largest challenges in stroke treatment is rapidly determining the cause, or etiology, of the stroke so that the risk recurrence can be mitigated. Currently, diagnostic tests for etiology determination are slow and unreliable, and in about one third of patients etiology is never determined. In ischemic stroke, thrombus composition, specifically red blood cell (RBC) content, has been shown through histological analysis to be predictive of stroke etiology. However, histological analysis is too slow to be performed in an acute clinical setting; non-invasive imaging techniques capable of rapid stroke etiology prediction hold immediate value in stroke care. Currently existing techniques use qualitative metrics and have produced underwhelming performance; the goal of this thesis was to develop a quantitative MR imaging method capable of accurate acute ischemic stroke etiology prediction.

In this thesis, I use the quantitative MR parameters R_2^* , quantitative susceptibility mapping (QSM) and fat fraction (FF) to characterize stroke thrombi. First, I showed that R_2^* and QSM can be used to derive a relationship with RBC content in blood clots *in vitro*. Following this, I applied deep learning to quantitative *ex vivo* thrombus MR images to predict histological thrombus RBC content. Finally, I used machine learning applied to texture features extracted from thrombus R_2^* , QSM and FF maps to predict stroke etiology using a random forest classifier. Separate models were built using patient clinical data and the combined set of thrombus texture and clinical data features. I found that the model built from imaging information alone was able to predict stroke etiology with comparable accuracy to previous qualitative models, but that when combined with patient clinical data the model's performance far exceeded that of previously derived predictors and generated highly accurate predictions of stroke

etiology in an independent test set. The works presented in this thesis offer extensive *ex vivo* evidence that quantitative MR imaging is capable of effective stroke thrombus etiology characterization. If implemented clinically, such a technique could enable consideration of thrombus composition and bolster stroke etiology determination, thereby improving management and care of acute ischemic stroke patients.

Co-Authorship Statement

This thesis is presented in an integrated article format, the Chapters of which are based on the following publications:

Chapter 2: Christiansen S.D., Liu J., Boffa M.B., and Drangova M. “Simultaneous R_2^* and quantitative susceptibility mapping measurement enables differentiation of thrombus hematocrit and age: an *in vitro* study at 3 T.” *Journal of Neurointerventional Surgery* 2019; 11.11: 1155-61.

My contributions to this work include study conception, preparation of blood clots and scanning phantom, MR imaging and data collection, data analysis and manuscript preparation. Dr. Junmin Liu designed the MR sequence used in all parts of this thesis, developed the B0-NICE code used for quantitative MR map generation, and contributed to study conception and manuscript preparation. Dr. Michael Boffa improved the blood clot preparation technique to more realistically mimic human thrombus and contributed to manuscript preparation. Dr. Maria Drangova contributed to study conception, data interpretation and analysis, and manuscript preparation.

Chapter 3: Christiansen S.D., Liu J., Bres Bullrich M., Sharma M., Pandey S.K., Boulton M., Sposato L.A., and Drangova M. “Quantitative prediction of stroke thrombus erythrocyte content from *ex vivo* multiparametric MRI using deep learning.” Submitted to *American Journal of Neuroradiology* March 2021.

My contributions to this work include study conception, preparation of scanning phantom, collection and MR imaging of stroke thrombi, data generation and analysis, development of the deep learning network architecture and code, and manuscript preparation. Dr. Junmin Liu designed the MR sequence, developed the B0-NICE code used for quantitative MR map

generation, and contributed to manuscript preparation. Dr. Maria Bres Bullrich was responsible for the recruitment and consenting of stroke patients into our study, as well as contributed to manuscript preparation. Drs. Sharma, Pandey and Boulton contributed to stroke patient recruitment and manuscript preparation. Dr. Luciano Sposato contributed to stroke patient recruitment, study design and was responsible for the collection of clinical data, as well as contributed to manuscript preparation. Dr. Maria Drangova contributed to study conception, data interpretation and manuscript preparation.

Chapter 4: Christiansen S.D., Liu J., Bres Bullrich M., Sharma M., Pandey S.K., Boulton M., Sposato L.A., and Drangova M. “*Ex vivo* thrombus MR imaging features and patient clinical data enable prediction of acute ischemic stroke etiology.” Submitted to *Stroke* April 2021.

My contributions to this work include study conception, preparation of scanning phantom, collection and MR imaging of stroke thrombi, data generation and analysis, modification of the machine learning code, and manuscript preparation. Dr. Junmin Liu designed the MR sequence, developed the B0-NICE code used for quantitative MR map generation, and contributed to manuscript preparation. Dr. Maria Bres Bullrich was responsible for the recruitment and consenting of stroke patients into our study, as well as contributed to manuscript preparation. Drs. Sharma, Pandey and Boulton contributed to stroke patient recruitment and manuscript preparation. Dr. Luciano Sposato contributed to stroke patient recruitment, study design and was responsible for the collection of clinical data, as well as contributed to manuscript preparation. Dr. Maria Drangova contributed to study conception, data interpretation and manuscript preparation.

Acknowledgements

First and foremost, I would like to thank Dr. Maria Drangova. This project could never have been completed without your mentorship and guidance. Your uncompromising drive is inspiring, and pushed me grow and improve myself in virtually every facet. You imbue passion, rigor and geniality in all those you interact, and I am honoured to have been one of your graduate students and grateful to learn so much from you.

I would next like to thank Dr. Junmin Liu, who beyond developing the MR sequence used in every part of my research, was immensely helpful in troubleshooting code and guiding me to generate my first sets of image data early on. You have remained a consistent and thoughtful supporter; a true innovator and endless source of insight.

I would also like to thank the remaining members of my advisory committee, Drs. Jean Théberge and Luciano Sposato, as well as Dr. Michael Boffa. You're calm, cogent natures led to countless enlightening meetings; your genuine support and encouragement will be forever appreciated.

I am grateful of all members of the Drangova lab I've had the privilege to work alongside, but in particular I acknowledge Dr. Zahra Hosseini, who welcomed me to the world of graduate school and mentored me by example. Joy Dunmore-Buyze and Dr. Ivailo Petrov continually remind me of all the things more important than work, through their empathy and humour. Trips to the abattoir dragged on but never outpaced your selfless characters. All other past and present members of the Drangova lab: Drs. Charmainne Cruje, Patricia Johnson, Daniel Gelman, Paul Picot, Jiro Inoue as well as Gregory Hong, Angad Bajwa, Miriam Hewlett, Tim Whelan, Emily Qin and Eric Grolman have each provided support to me in and outside of the lab in all your own unique ways.

I acknowledge, Justina Diaz Legaspe, Maria Bres Bullrich, Ada Manini, and all other members of the University Hospital Endovascular Treatment Team, for their tireless efforts to recruit patients and save stroke thrombi for me, you have done everything and more to make this project possible. Dave Reese and Dr. Trevor Wade, and Caroline O'Neil were invaluable for the MR imaging and histological portions of my research, respectively.

I finally would like to thank Greg and Dr. Raanan Marants for their friendship, along with every other member of our perpetually underachieving intramurals teams; I will cherish these years.

This work would not have been possible had it not been for the unwavering support of my parents, Wendy and Roy, and my sister, Kendra; your presence continues to inspire me each day. And to all my friends from Scarborough, whose enlivened passion imbues my world with colour. Finally, I am ever grateful to my partner, Elizabeth, for your radiant, ambitious love. Each day with you is a gift, and I need nothing more.

I do not know what I may appear to the world, but to myself I seem to have been only like a boy playing on the sea-shore, and diverting myself in now and then finding a smoother pebble or a prettier shell than ordinary, whilst the great ocean of truth lay all undiscovered before me.

-Sir Isaac Newton

Do not fear the shadowed truth
Nor the hallowed light of its ingest
At times themes sepulchral nakedly stalk
Find comfort in their nascence and purposeful exile

We can seem so small and blind
Naively clutching at our grains of sand
We navigate an endless implacable dessert
Unable to sculpt the dunes

But the universe in your hands is unraveling
Humbly we bare the threads
We tug at knots of truth and consequence
And silently demystify the ether

Ebullience crowds each knot untied
Revealing another deeper buried in its place
The humble pursuit of knowledge
Sustained at our hands, persists

Dedicated to my grandparents Roni, John and Elizabeth.
Each of whom passed on during these few short years.

Dedicated to my parents, Wendy and Roy.
For unwavering support and endearment.

Dedicated to Elizabeth.
My warmth, my light.

Table of Contents

Abstract	i
Keywords	ii
Lay Summary	iii
Co-Authorship Statement	v
Acknowledgments	vii
Dedication	x
Table of Contents	xi
List of Tables	xv
List of Figures	xvi
List of Appendices	xxiii
List of Abbreviations	xxiv
1 Introduction	1
1.1 Motivation and overview	1
1.2 Stroke mechanisms and treatment	3
1.3 Evolution of acute ischemic stroke care and the role of imaging	5
1.4 Stroke etiology and clinical diagnosis.....	10
1.4.1 Subtypes of acute ischemic stroke	10
1.4.2 Clinical determination of etiology	12
1.4.3 Weaknesses of the current paradigm	13
1.5 Thrombus composition and its relationship to stroke etiology.....	14
1.6 Imaging inference of thrombus composition and etiology	19

1.6.1 Qualitative thrombus MR characterization	20
1.6.2 Effective transverse relaxation time (R_2^*)	22
1.6.3 Quantitative susceptibility mapping	23
1.6.4 Quantitative thrombus MR characterization	24
1.7 Artificial intelligence and potential for advanced thrombus analysis	27
1.7.1 Machine Learning	28
1.7.2 Neural networks and deep learning.....	32
1.8 Thesis hypotheses and objectives.....	36
1.9 References	38
2 Simultaneous R_2^* and quantitative susceptibility mapping measurement enables differentiation of thrombus hematocrit and age: an <i>in vitro</i> study at 3T	50
2.1 Introduction	50
2.2 Materials and methods.....	52
2.2.1 Phantom preparation	52
2.2.2 Image acquisition	53
2.2.3 Image reconstruction and multi-parameter mapping	54
2.2.4 Image analysis.....	55
2.2.5 Data analysis.....	56
2.3 Results.....	56
2.3.1 Acute clot (≤ 6 hours)	56
2.3.2 Chronic clot (> 6 hours).....	57
2.3.3 Acute and chronic clot differentiation	58
2.3.4 Clot hematocrit prediction	58
2.3.5 Identification of lipid and calcifications within clot	61
2.4 Discussion	63
2.5 Conclusion.....	67
2.6 References	68

2.7 Supplementary material	72
2.7.1 Methods	72
2.7.2 Results	73
2.7.3 References.....	75
3 Quantitative prediction of stroke thrombus erythrocyte content from <i>ex vivo</i> multiparametric MRI using deep learning	76
3.1 Introduction	76
3.2 Materials and methods.....	78
3.2.1 Thrombus collection and storage.....	78
3.2.2 <i>Ex vivo</i> thrombus imaging.....	80
3.2.3 Image processing.....	80
3.2.4 Histological analysis	81
3.2.5 Deep learning network.....	81
3.2.5.1 Network architecture.....	81
3.2.5.2 Data augmentation.....	82
3.2.5.3 Network evaluation	84
3.2.6 Statistical analysis.....	85
3.3 Results.....	85
3.4 Discussion	89
3.5 Conclusion.....	92
3.6 References	94
3.7 Supplementary material	98
4 <i>Ex vivo</i> thrombus MR imaging features and patient clinical data enable prediction of acute ischemic stroke etiology	100
4.1 Introduction	100
4.2 Materials and methods.....	102
4.2.1 Study design and inclusion criteria.....	102

4.2.2 Thrombus storage and imaging	103
4.2.3 Image post processing	105
4.2.4 Radiomics analysis and machine learning models	105
4.2.4.1 Feature extraction and selection.....	106
4.2.4.2 Random forest analysis	107
4.2.5 Statistical analysis	108
4.3 Results.....	108
4.4 Discussion	112
4.5 Conclusion.....	115
4.6 References	116
4.7 Supplementary material	121
5 Conclusions and Future Directions	122
5.1 Conclusions	122
5.2 Limitations.....	124
5.2.1 Analysis of blood clot RBC, lipid and calcium content	124
5.2.2 Prediction of stroke thrombus RBC content	125
5.2.3 Prediction of stroke etiology	126
5.3 Future directions	126
5.3.1 <i>In vitro</i>	127
5.3.2 <i>Ex vivo</i>	128
5.3.3 <i>In vivo</i>	128
5.4 References	131
A Copyright Releases	133
B Ethics Approvals	141
C Curriculum Vitae	143

List of Tables

1-1 Studies assessing the relationship between ischemic stroke etiology and histological composition of thrombi retrieved by endovascular therapy	17
3-1 Clinical details of the patient cohort for each thrombus storage group ...	79
3-2 Performance of the CNN for thrombus histological RBC content prediction (T/F: true/false; ×n: training set duplication by a factor of n)	86
3-3 Performance of the CNN for thrombus histological RBC content prediction when limited to thrombi between 20 – 45% RBC content (T/F: true/false; ×n: training set duplication by a factor of n)	88
4-1 Summary of clinical details for each patient cohort	104
4-2 Clinical details of CE and LAA strokes within the training cohort	110
4-3 Thrombus MR imaging texture features selected by MLR for differentiating CE and LAA stroke within the training cohort	111
4-4 Performance of random forest classifiers for stroke etiology prediction	111
Supp. 4-1 Texture features used in this study; more detail available in Vallières et al. 2015	121

List of Figures

- 1-1** Gross photograph of a thrombus retrieved from an acute ischemic stroke patient. Shown below it is the stent retriever used to remove the thrombus from the cerebral vessels as a part of endovascular therapy, which is discussed in section 1.3. 5
- 1-2** Non-contrast CT of an acute ischemic stroke patient showing signs of infarction by hypoattenuation of the right lentiform nucleus (arrows). Subtle hypoattenuation present in the acute stroke image (left) acquired 22 minutes after stroke onset progresses to more distinct hypoattenuation at 1 (middle) and 7 (right) days after stroke onset. Figure from Von Kummer et al., reproduced with permission.²⁵ 7
- 1-3** Diffusion-perfusion MR images of an acute ischemic stroke patient showing mismatch in size between hyperintense lesions in the right caudate nucleus on DWI (left) and PWI (middle) images acquired 4.5 hours after stroke onset. A T₂-weighted image (right) acquired 7 days after onset shows a final ischemic lesion that has expanded beyond the DWI lesion within the region of the perfusion abnormality. Figure from Baird et al., reproduced with permission.²⁹ 8
- 1-4** Schematic drawing of the typical components constituting stroke thrombi. Activated platelets connect fibrin strands to form a webbing which encapsulates RBCs, WBCs, and holds the thrombus together. Isolated pockets of RBCs tend to form within platelet/fibrin-rich regions with WBCs on the border between them.⁶³ 15
- 1-5** Example thrombus H&E section at low (A) and high (B) magnification with RBCs in red, fibrin/platelets in pink and WBCs in dark blue. An example segmentation output used to quantify thrombus composition is

shown in (C). The typical thrombus has a composition of approximately 30, 60 and 10% RBCs, fibrin/platelets and WBCs, respectively. ¹⁰ Note the heterogeneous distribution of components, with distinct deposits of RBCs and fibrin/platelets arranged throughout the thrombus.	16
1-6 Neurological MR (left) and CT (right) images of stroke patients demonstrating qualitative thrombus imaging signs; SVS and HDAS, respectively. Figure from Liebeskind et al., reproduced with permission. ⁶⁶ ..	21
1-7 Example signal decay curve with an exponential curve fit. Higher R_2^* values correspond to a more rapidly decaying signal.	22
1-8 A uniform magnetic field in the presence and absence of magnetic material. Paramagnetic materials have a positive magnetic susceptibility and attract magnetic lines of force, while diamagnetic materials have a negative susceptibility and repel them.	23
1-9 MR R_2^* (A) and QSM (B) maps of a phantom containing pairs of deoxygenated blood clots prepared <i>in vitro</i> of 10-60% RBC content (yellow label) with the remainder being composed of fibrin and platelets.	25
1-10 Example thrombus (A) H&E histology slide (RBCs stain red; fibrin/platelets stain pink) along with a corresponding slice of its (B) GRE magnitude (TE = 31 ms), (C) R_2^* and (D) QSM maps. MR images are shown in a coronal view, with the vertical scanning vial walls indicated with ► and the thrombus outlined in cyan. Agar fills the space below the thrombus and outside the vials. * indicates the RBC-rich body of the thrombus which has a noticeably lower magnitude signal and higher R_2^* and QSM values than its fibrin-rich tail.	26
1-11 Schematic diagram of the random forest classifier.	29

- 1-12** Diagram showing an example of texture feature value calculation from a second-order statistical matrix. The total number of co-occurring pairs of pixels across one direction in an image is used to create a gray level co-occurrence matrix (GLCM), whose normalized values are used for the calculation of texture feature values. Figure from Brynolfsson et al., reproduced with permission.⁹⁹ 31
- 1-13** Schematic diagram of the simple perceptron. Each connection between the input layers and the hidden layer nodes is associated with a tuneable weight parameter (w_i). Each hidden layer node performs a weighted sum of all input features (Σ_i), which themselves are summed (Σ_j) by the output layer. The output is determined to be true or false based on a binary output function. 33
- 1-14** Architecture of a modern CNN. Three convolutional layers are separated by ReLu's and max pooling and/or batch normalization functions, followed by a fully connected layer with dropout before the final output layer. 35
- 2-1** Acute blood clot relaxation and magnetic susceptibility quantification; shown are the central coronal slices of the (A) R_2^* [0 s⁻¹, 80 s⁻¹] and (B) QSM [-0.5 ppm, 0.5 ppm] maps for the blood-only thrombus phantom at 6 hours post clotting. The mean (C) R_2^* and (D) QSM values of an individual clot from each pair (10 to 60% hematocrit) are shown over the first 6 hours post clotting; error bars were omitted for clarity. The mean and standard deviation of each clot pair with the same nominal hematocrit at the six hour time point are shown for (E) R_2^* and (F) QSM, demonstrating reproducibility. 57
- 2-2** Blood clot R_2^* and QSM of chronic clots throughout ageing; (A) R_2^* and (B) QSM values of blood-only clots from 6 up to 144 hours post clotting (the 6-hr time point is included in order to relate these results to those of the acute clots of Figure 2-1). Plotted are mean values of individual clots; standard

deviation error bars of only the 60% hematocrit clots are shown for clarity, error bars for QSM were smaller than the symbols. (C) Scatter plot and linear regression of R_2^* versus QSM values at all time points for clots of each hematocrit. 59

2-3 Relationship between hematocrit and measured quantitative imaging values in acute (≤ 6 hours) and chronic (> 6 hours) clot. (A) Acute clot hematocrit can be estimated linearly from measured QSM values, while (B) chronic clot hematocrit can be estimated from an exponential relation of the ratio of R_2^* / QSM . Shown are data points from the same 6 clots (one from each pair of 10 to 60% hematocrit) plotted in Figures 2-1 and 2-2. 60

2-4 Regions (1.2×1.4 mm) from representative sagittal slices through select clots (0, 20, 40% hematocrit) in the lard clot phantom demonstrating discriminability of the added component; shown are early and late echo magnitude images of clots within the phantom at (A) 7 hours and (B) 4 days post clotting. These images represent the current standard technique for thrombus characterization; lard is either visible within clot as a nondescript area of low signal (red arrows) or is undetectable because of signal void produced by chronic clot (B; 20 and 40% clots at 31 ms). R_2^* , QSM and fat fraction (FF) maps of the phantom are shown at (C) 7 hours and (D) 4 days post clotting. Lipid is readily distinguishable from clot by its elevated FF value in clots of all hematocrits whether acute or chronic. Noticeable differences in R_2^* and QSM values between clots of different hematocrit can also be observed in the chronic clots in (D). 62

2-5 Regions (1.2×1.4 mm) from representative sagittal slices through a single whole-blood clot with an added piece of agar containing 5M calcium carbonate (red arrows); shown are early and late echo magnitude images at (A) 2 hours and (B) 2 days post clotting. Similar to the appearance of the lard added to clot, calcium carbonate shows low signal on early and late

magnitude images, but differs with high R_2^* , low QSM and low FF values. The calcium carbonate is definitively identified within both acute and chronic clot by its negative QSM values (black in the QSM maps of (B)). 62

Supp. 2-1 Central coronal slices of the (A) B0-NICE fat fraction (FF) [0, 1], (B) MEDI quantitative susceptibility mapping (QSM) [-1.25 ppm, 3.25 ppm] and (c) B0-NICE R_2^* [0 s⁻¹, 350 s⁻¹] maps. For the FF phantom (A) the nominal fat fraction of each vial is identified; unlabeled vials contain both fat and Gadolinium (Gd) and were not analyzed. For the susceptibility phantom (B, C), labels show Gd concentration (mM); unlabeled vials contain oil/water emulsions. (D) B0-NICE FF plotted against FF measured using the IDEAL sequence; (E) measured QSM against expected sample susceptibility; (F) B0-NICE-derived R_2^* is plotted against Gd concentration. Error bars represent the standard deviation of all pixels within each region of interest. Note that the oil vial displays an artifactual diamagnetic susceptibility on the QSM map because of the varying fat-water phase shifts in the processed echoes. . 74

3-1 Schematic diagram of the CNN. Three-dimensional RGB images consisting of segmented, normalized thrombus R_2^* , QSM and GRE magnitude images are fed into a network consisting of 3 convolutions layers with average pooling layers in between and a dropout layer at the end, before a final fully-connected layer. Padding is employed to retain image size in the convolutional layers. 82

3-2 Representative training set thrombus RBC content distribution (A) before and (B) after input sampling equalization. 83

3-3 An example normalized, segmented thrombus RGB image slice is shown (A) before and (B) after random image transformation. R_2^* , QSM and GRE magnitude pixel values represent the red, green and blue image color channels, respectively. 84

3-4 Linear regression plots of the CNN predicted thrombus RBC content against the histological value for best-performing network iterations on the equalized, transformed dataset with (A) $\times 1$, (B) $\times 3$, and (C) $\times 5$ duplication, respectively. Plotted are the median predictions from all MR slices available for each thrombus. These same predictions replotted with only thrombi with histological RBC content between 20 – 45% are shown in (D), (E) and (F), respectively. 88

Supp. 3-1 Bland-Altman plot showing the difference between thrombus histological RBC content and that predicted through mean R_2^* and QSM values using the methods described in Chapter 2. Predicted RBC content consistently underestimated the histological values, yielding a mean error of $20 \pm 22\%$ and a mean absolute error of $25 \pm 16\%$ 98

Supp. 3-2 Effect of storage method and time between thrombus retrieval and MR imaging on mean thrombus (A) R_2^* and (B) QSM values. Thrombi were either stored at room temperature and scanned within the same workday, or stored in a fridge until the next available workday. Two-tailed T-tests between the two groups R_2^* and QSM values yielded significant differences with $p = 0.0005$ and $p = 0.02$, respectively. 98

Supp. 3-3 Thrombus multi-section histological results. Mean RBC content is shown at 3 or 4 evenly spaced intervals through the retrieved stroke thrombi. Red dots indicate the average RBC content values at each slice for all thrombi. 99

4-1 Representative segmented thrombus R_2^* (top), QSM (middle) and FF (bottom) images shown in (A) original form, (B) after equal-probability quantization with 64 bins and (C) after uniform quantization with 8 bins. These extraction parameters control the pixel distribution and coarseness under which features are extracted, respectively..... 107

4-2 ROC curves for the determination of CE vs. LAA stroke etiology within the training (A) and validation (B) cohorts using the imaging, clinical and combined random forest classifier models.	111
5-1 Axial time of flight (TOF) angiography, R_2^* , QSM and FF maps of an ischemic stroke patient with intracranial thrombus (arrow) of atherothrombotic origin. High R_2^* and QSM indicate a deoxygenated, RBC-rich thrombus, while a high FF suggests the presence of lipid (from plaque core).....	129

List of Appendices

Copyright Releases	133
Ethics Approvals	141
Curriculum Vitae	143

List of Abbreviations

3D	three-dimensional
AIS	acute ischemic stroke
AUC	area under the ROC curve
CE	cardioembolism
CNN	convolutional neural network
CT	computed tomography
CTP	computed tomography perfusion
DWI	diffusion-weighted imaging
EVT	endovascular therapy
FF	fat fraction
Gd	gadolinium
GRE	gradient recalled echo
H&E	hematoxylin and eosin
HDAS	hyperdense artery sign
HU	Hounsfield unit
LAA	large-artery atherosclerosis
MEDI	morphology enabled dipole inversion
MCA	middle cerebral artery
MLR	multivariate logistic regression
MR	magnetic resonance
PPP	platelet-poor plasma
PRP	platelet-rich plasma
PWI	perfusion-weighted imaging
QSM	quantitative susceptibility mapping
RBC	red blood cell
ReLU	rectified linear unit
RMSE	root mean square error
R_2^*	effective transverse relaxation time; $1/T_2^*$

ROC	receiver operator characteristic
ROI	region of interest
rtPA	recombinant tissue plasminogen activator
SVO	small-vessel occlusion
SVS	susceptibility vessel sign
T ₂ *	transverse relaxation rate
TE	echo time
TOAST	trial of ORG 10172 in acute stroke treatment
TOF	time of flight
TR	repetition time
WBC	white blood cell

CHAPTER 1

General Introduction

1.1 Motivation and overview

Stroke represents one of the most prevalent and devastating diseases across the world. In 2013, stroke was the second most common cause of death and third most common cause of disability worldwide.¹ In Canada, one stroke is said to occur every 10 minutes, and collectively stroke is responsible for an economic burden of over \$3.6 billion in direct costs annually.² While recent years have seen the incidence, mortality and disability burden of stroke decline,³ the number of people who are affected by stroke in any form (deaths, survivors, and those who remain disabled) is increasing.¹

Patients who have survived their first stroke are over 10 times more likely to have a second within 12 months compared to those with no stroke history,^{4,5} and these secondary strokes are more likely to be fatal or disabling than the first.⁶ With the number of stroke survivors in Canada expected to increase by 1.5 to 2 times between 2013 and 2038,⁷ there is a growing population of individuals with heightened stroke risk who require prophylactic therapy to minimize their risk of stroke recurrence. The optimal therapy for limiting recurrence is specific to the underlying etiology (cause) of the primary stroke, however etiology may take weeks to determine, and even following extensive clinical testing remains unknown in as much as 35% of cases.⁸

Medical imaging, through x-ray, ultrasound, computed tomography (CT) and magnetic resonance (MR) imaging, serves a vital role within acute stroke care. CT and MR imaging are currently the only techniques available to

identify whether a stroke is ischemic or hemorrhagic in nature, a critical disease characteristic which determines the course of stroke treatment.⁹ However, no attempt is currently made to use imaging techniques to deduce stroke etiology beyond the use of x-ray angiography and echocardiography to search for signs of atherosclerotic stenosis and arrhythmia, respectively; these have proven to be inconsistent and unreliable indicators. This approach fails to take advantage of all the information available from acute imaging, and in ischemic stroke in particular, ignores the information available from within the thrombus (blood clot) itself. Evidence is mounting to suggest that thrombus composition may be indicative of underlying stroke etiology.^{8,10,11} Presently, the only method to assess thrombus composition is histological analysis, but this can only be completed in cases where a thrombus has been physically retrieved from the patient during treatment. The benefit of an imaging method capable of non-invasively identifying thrombus composition is immeasurable, and there remains ample room for improvement amongst current experimental imaging techniques.

Admittedly, because stroke care is extremely time-sensitive, access to advanced imaging scanners, particularly for MR imaging, is a challenge for many centres and limits the ability to add new imaging techniques to stroke protocols. However, the increasing accessibility of MR and CT scanners, combined with recent recommendations from the American Heart Association that stroke patients presenting within 6 – 24 hours of symptom onset receive advanced imaging (MR or CT) to guide therapy,¹² means that the number of patients for which advanced imaging can be completed is only increasing.

This thesis describes the development and validation of novel MR imaging analysis techniques aimed at quantitatively predicting the composition and etiology of acute ischemic stroke thrombi. The work presented herein first demonstrates the sensitivity of the relevant quantitative MR imaging parameters to RBC content in a set of blood clots prepared *in vitro* (Chapter

2), followed by an evaluation of composition inference (Chapter 3) and etiology prediction (Chapter 4) using deep learning and machine learning, respectively, applied to quantitative MR images of retrieved acute stroke thrombi *ex vivo*. This introductory chapter provides a comprehensive overview to motivate the work presented in the following chapters, beginning with a description of the pathophysiologic mechanisms of stroke (1.2), followed by the evolution of acute stroke care (1.3), current stroke etiology determination techniques and their associated limitations (1.4), histological relationships between thrombus composition and etiology (1.5), previously developed imaging techniques for thrombus composition and etiology prediction (1.6), modern machine and deep learning image analysis techniques and their potential for improved thrombus characterization (1.7), and finally the hypothesis and objectives of this thesis (1.8).

1.2 Stroke mechanisms and treatment

A stroke occurs when brain cells are damaged due to improper blood flow, and may occur due to lack of blood from vessel blockage (ischemic) or compression from an internal bleed (hemorrhagic). For the former, treatment consists of restoration of blood flow to the affected tissue. The derived benefit from reperfusion depends strongly on the length of time the brain has faced oxygen deprivation. Assessment of the affected tissue's viability and prediction of the brain's response to reperfusion is the most important task faced by stroke interventionalists treating ischemic stroke.

A stroke occurs when brain tissue is injured by either a deprivation of oxygenated blood supply or hydrostatic pressure from an internal bleed, to an extent and duration upon which neurological symptoms of impairment begin to appear. Lack of oxygen results in neuronal cell energy metabolism

disruption leading to ion channel failure, sodium, chloride and then water influx, while internal bleeding results in the mechanical disruption and deformation of cells, mitochondrial dysfunction and membrane depolarisation.^{13,14} Both mechanisms result in cell swelling (cytotoxic edema) and, eventually, to irreversible cell death. Symptoms of stroke vary widely depending on the region facing injury, but most commonly manifest as acute one-sided weakness (hemiparesis), facial droop, difficulty understanding and formulating speech (aphasia), unclear speech (dysarthria), visual field deficits, headaches and/or lack of muscle coordination (ataxia).¹⁵ Strokes occurring as a result of hypoxia are referred to as ischemic while those due to internal bleeding are referred to as hemorrhagic. Ischemic strokes, the focus of this thesis, represent approximately 80% of all strokes,¹⁶ and are most commonly caused by thrombi which have embolized from a downstream artery and were halted within the narrowing cerebral vessels, disrupting blood flow. A photograph of a retrieved ischemic stroke thrombus is shown in Figure 1-1. Less commonly, thrombi may form *in situ* directly within cerebral arteries (lacunar stroke),¹⁷ or, less commonly still, stroke may be caused by the embolization of materials other than thrombus, including fat, calcium, air, infected (septic) tissue or tumour (usually myxoma).¹⁸

In all cases, the treatment for ischemic stroke is reperfusion therapy; restoration of blood flow to the ischemic areas. In principle, complete reperfusion of affected tissue can lead to the eradication of symptoms and near-instant recovery, if all affected tissue is still viable. In practice, complete reperfusion is rarely achieved, may serve no benefit to tissue which has already been irreversibly infarcted, and may actually cause damage to surrounding viable tissue through hemorrhage of areas reperfused with a blood brain barrier disrupted by ischemia.¹⁹ Failure to achieve reperfusion in viable tissue however can lead to permanent disability or death, and while the human brain is capable of recovery through the rewiring of neurons to a

phenomenal degree, a process known as neuroplasticity, a return to pre-stroke capability rarely occurs.²⁰ Determination of the amount of salvageable tissue, and the risks associated with treatment, is therefore the critical task for stroke interventionalists treating ischemic stroke. Methods for achieving reperfusion have thus developed in tandem with strategies to identify the patients most likely to derive benefit.

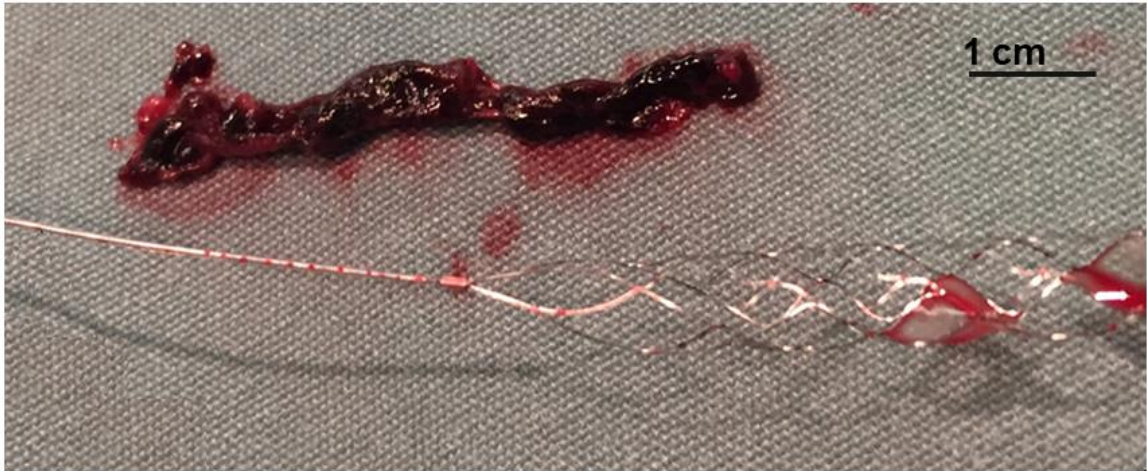


Figure 1-1: Gross photograph of a thrombus retrieved from an acute ischemic stroke patient. Shown below it is the stent retriever used to remove the thrombus from the cerebral vessels as a part of endovascular therapy, which is discussed in section 1.3.

1.3 Evolution of acute ischemic stroke care and the role of imaging

Our understanding of stroke and its optimal care continues to evolve. Reperfusion is currently the only treatment and two clinically approved techniques to achieve this exist today: thrombus lysis by recombinant tissue plasminogen activator and extraction by endovascular therapy. Each has seen its usefulness and impact expand since it was first approved, and in particular, the recently widened treatment time window for endovascular

therapy opens the door for increased involvement of advanced imaging techniques within acute stroke care.

The first recorded description of stroke came in the 4th century BCE from Hippocrates, who termed a set of symptoms that included sudden onset paralysis, loss of consciousness and death as “apoplexy,” meaning “struck down violently.”²¹ Since then, our understanding of the causes and mechanisms of stroke have grown enormously, and yet only recently has modern medicine been capable of direct treatment. Up until the 1990’s, stroke treatment consisted largely of supportive care and the prevention of complications.²¹ Following the results of a 1995 National Institute of Neurological Disorders and Stroke recombinant tissue plasminogen activator (rtPA) study,²² the Food and Drug Administration approved the use of intravenous rtPA for ischemic stroke patients within 3 hours of symptom onset in 1996.²³ rtPA is a synthetic version of the naturally occurring human clot-dissolving protein, tissue plasminogen activator, and was initially indicated for all ischemic stroke patients under 3 hours post-onset lacking contraindications to the drug. Further studies and clinical trials demonstrated that rtPA could be beneficial for patients up to 4.5 hours after onset if those presenting with severe infarction, and therefore low tissue viability, as determined by non-contrast CT were excluded.^{24,25}

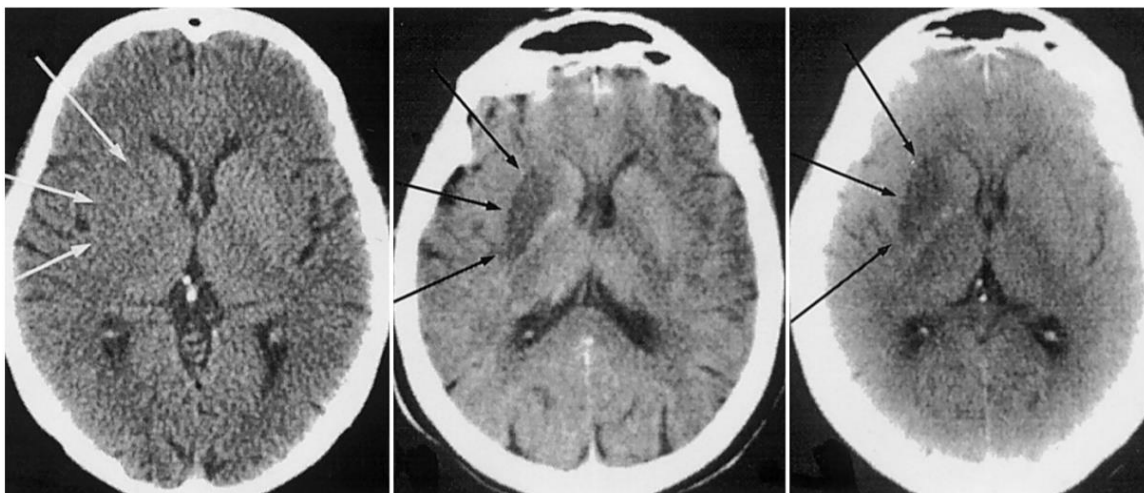


Figure 1-2: Non-contrast CT of an acute ischemic stroke patient showing signs of infarction by hypoattenuation of the right lentiform nucleus (arrows). Subtle hypoattenuation present in the acute stroke image (left) acquired 22 minutes after stroke onset progresses to more distinct hypoattenuation at 1 (middle) and 7 (right) days after stroke onset. Figure from Von Kummer et al., reproduced with permission.²⁶

CT is capable of detecting severe edema associated with infarction through hypoattenuation within brain parenchyma, as shown in Figure 1-2. The number and extent of hypointense lesions is associated with risk of hemorrhagic transform following rtPA administration.²⁷ However, non-contrast CT possesses a relatively poor sensitivity (~65%) for detecting acute stroke lesions,²⁶ and lacks the ability to identify tissue at risk of infarction but not yet beyond the threshold of irreversible damage. Hypoperfused tissue that is salvageable but will proceed to infarction if left untreated is referred to as the stroke “penumbra,” while ischemic tissue that has already past the point of irreversible damage and will infarct is deemed the “core.”²⁸ In conjunction with the rising prominence of rtPA treatment came MR studies demonstrating the potential for diffusion-weighted imaging (DWI) to visualize the infarct core along with perfusion-weighted imaging (PWI) to show the penumbra.^{29,30} A mismatch between DWI and PWI lesions indicates the presence of vulnerable penumbral tissue that will proceed to infarction if reperfusion is not achieved (Figure 1-3). A non-placebo-controlled study

(DEFUSE) demonstrated promise that DWI and PWI could be used to identify patients who would respond positively to rtPA for up to 6 hours after onset, showing that patients with mismatched DWI/PWI lesions responded better than those with similar lesion sizes at presentation.³¹ However, a later randomized controlled trial (EPITHET) into the use of DWI/PWI failed to show a difference in benefit between patients given rtPA with and without a mismatch.³² As a consequence, advanced imaging selection for rtPA administration was never widely adopted into the clinic and the 2018 Canadian stroke guidelines recommend no input from imaging for the decision beyond examining for hemorrhage and infarction severity on CT.³³

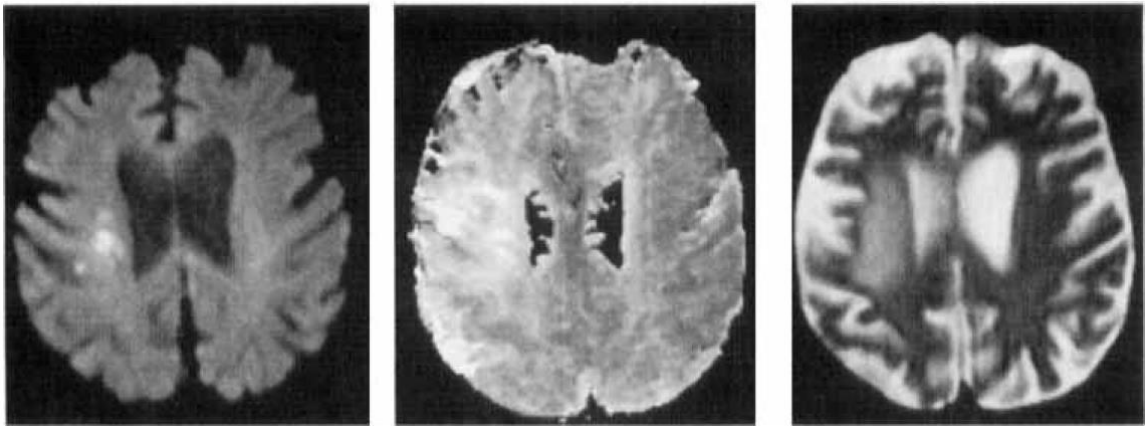


Figure 1-3: Diffusion-perfusion MR images of an acute ischemic stroke patient showing mismatch in size between hyperintense lesions in the right caudate nucleus on DWI (left) and PWI (middle) images acquired 4.5 hours after stroke onset. A T2-weighted image (right) acquired 7 days after onset shows a final ischemic lesion that has expanded beyond the DWI lesion within the region of the perfusion abnormality. Figure from Baird et al., reproduced with permission.³⁰

However, in recent years the use of imaging to illuminate penumbral and core tissue has seen a resurgence with the advent of endovascular therapy, the use of an inserted stent retriever (mechanical thrombectomy) or aspirator to physically remove the occluding thrombus. A 2012 prospective study showed benefit in the use of DWI/PWI for selection of patients receiving

endovascular therapy within 12 hours of onset.³⁴ Contemporaneously, CT perfusion (CTP) imaging was gaining prominence as a tool for penumbral stroke imaging, and was shown to provide a comparable assessment of ischemic core and penumbra as DWI and PWI.³⁵ A 2014 randomized clinical trial (EXTEND-IA) demonstrated benefit for endovascular therapy in patients stratified by CTP-based perfusion mismatch assessments within 8 hours of symptom onset.³⁶ By the mid-2010's, the utility of advanced (MR or CT) imaging for selecting patients suitable for endovascular therapy was well documented, but given the relatively short accepted time window for which patients could be treated (6 – 8 hours in most centres), only a fraction of stroke patients were eligible and in Canada advanced imaging selection was not formally recommended unless it could be done without any delay of treatment administration.³⁷ Recently, two randomized, controlled trials (DAWN, DEFUSE 3) demonstrated clear evidence in favour of using advanced, perfusion-based imaging (MR or CTP) to identify patients most likely to benefit from endovascular therapy, and notably this was demonstrated in patients at up to 24 hours after stroke onset.^{38,39} Following the release of these trials, stroke guidelines were updated and today advanced imaging is recommended for ischemic stroke patients arriving between 6 – 24 hours after symptom onset to select patients likely to benefit from therapy; stroke centres are expected to see a significant increase in the number of patients eligible for advanced imaging and endovascular therapy subsequent to the implementation of these guidelines.⁹ Such an increase also creates opportunity for adoption of novel imaging acquisitions, which expand the information available to clinicians during acute stroke treatment. Beyond selecting patients appropriate for acute treatment, imaging also offers potential for improving patient care during their recovery; namely in identifying the underlying cause of the primary stroke so that the risk of recurrence can be mitigated.

1.4 Stroke etiology and clinical diagnosis

A number of potential mechanisms can be responsible for ischemic stroke. The need to identify the underlying cause, or etiology, of a stroke is critical given the elevated risk of recurrence after primary stroke as the most effective risk-mitigating therapy differs between etiologies. In particular, cardioembolic and large artery atherosclerotic stroke are the most common etiologies and require different antithrombotic drugs to optimally limit their chance of recurrence; cardioembolic strokes are most often caused by arrhythmias, which can be challenging to detect within the post-stroke window of elevated secondary stroke risk.

Stroke is a unique disease in that the risk of recurrence is vastly increased after an initial stroke has occurred; within one year the risk of recurrence is approximately 13%, over 10 times the risk in the general population.⁴⁰ Compounding this is the unfortunate fact that secondary strokes are typically more devastating than the first. Accordingly, identifying the underlying cause, or etiology, of a stroke so that the patient may be treated to optimally mitigate the risk of recurrence is a critical component of stroke care. There are myriad different causes, known as subtypes, of ischemic stroke and these will be detailed in the following section before current strategies for etiology determination, and their associated weaknesses, are discussed.

1.4.1 Subtypes of acute ischemic stroke

The Trial of Org 10172 in Acute Stroke Treatment (TOAST) classification system,⁴¹ developed in the 1990's, remains the most widely used system to categorize stroke subtype in clinics today, largely due to its simplicity relative to later proposed schemes.⁴² TOAST stratifies ischemic stroke into one of 5 subtypes: large-artery atherosclerosis (LAA), cardioembolism (CE), small-

vessel occlusion (SVO), stroke of other determined etiology and stroke of undetermined etiology.

LAA is diagnosed in approximately 25% of all ischemic strokes,⁴³ and occurs subsequent to an immunoinflammatory reaction to circulating blood cholesterol resulting in atherosclerotic plaque formation within the vessel wall of a major feeding artery to the brain (typically the internal carotid artery).⁴⁴ The growing plaque expands into the vessel lumen and often, but not always, ruptures prior to inducing thrombosis on its surface; the nascent thrombus eventually embolizes to the intracranial arteries.⁴⁵ Almost everyone develops detectable atherosclerosis within intracranial vessels as they age,⁴⁶ and the risk of LAA stroke has been correlated to its severity.⁴⁷

CE is diagnosed in between 20 to 40% of ischemic strokes and is resultant from a vast number of potential mechanisms, the original TOAST paper lists over 20 possible sources,⁴¹ but most commonly occurs from complications of atrial fibrillation. Atrial fibrillation is a sporadic, often asymptomatic arrhythmia of the heart that causes blood to flow poorly and stagnate within its chambers, eventually leading to thrombus formation. When no concomitant valvular disease is present (70-96% of AF cases),⁴⁸ 90% of AF-induced thrombi form within the left atrial appendage,⁴⁹ where they can sit for weeks or perhaps months at a time prior to embolization.⁵⁰ AF is present in only 1% of adults (9% of those 80 and older), but entails a 5-fold overall increase in stroke risk compared to those in normal sinus rhythm.⁵¹

SVO, also known as lacunar stroke, is diagnosed in approximately 15% of ischemic strokes and is defined as a stroke that occurs within the subcortical vessels of the brain. SVO occurs either through lipohyalinosis, a fibrotic vessel wall thickening, or intracranial atherosclerosis through a process originally thought to be distinct from the cervicocranial atherosclerosis responsible for LAA,⁵² being associated specifically with vascular conditions

including diabetes and hypertension.⁴¹ However, more recent work has demonstrated no difference in the risk factor profiles between SVO stroke patients and those of other types.⁵³ SVO strokes are comparably less severe than those from LAA and CE,⁵⁴ as they necessarily involve smaller vessels with less overall impact on cerebral perfusion, and will not be discussed further in this thesis.

Strokes of other determined etiology represent approximately 5% of ischemic stroke cases and consist of the miscellaneous, uncommon causes of stroke including dissection, other nonatherosclerotic vasculopathies, hypercoagulable states and hematologic disorders.⁴¹

Strokes of undetermined etiology account for approximately 35% of ischemic strokes, though this number varies widely between stroke sites due to differences in clinical practice and resources. This subtype includes both strokes whose cause could not be identified following clinical evaluation, and those in which two or more potential, conflicting causes were identified. There is evidence to suggest that the majority of undetermined strokes are CE in origin, following the missed diagnosis of arrhythmia.⁸

1.4.2 Clinical determination of etiology

The current clinical approach for identifying stroke etiology follows from that prescribed by the original TOAST criteria; LAA is considered if significant stenosis (>50%) can be found in any major ipsilateral carotid artery, in absence of the 20+ risk factors that indicate CE, and vice versa.⁴¹ Stenosis is typically evaluated through an x-ray angiogram, while AF, if not previously diagnosed, is searched for through echocardiographic and electrocardiographic (ECG) monitoring during a patient's hospital stay prior to long-term observation at home with an external ECG monitor for at least 2 weeks if necessary.⁵⁵ Additional causes of embolic stroke are identified

through a wide variety of means, including ultrasound imaging, laboratory blood tests and examining clinical history. These etiologies vary in their difficulty to identify, but are uncommon and their clinical impact is relatively minor compared to that of the LAA and CE subtypes.

1.4.3 Weaknesses of the current paradigm

Following an ischemic stroke, antiplatelet drugs are routinely given to reduce the risk of stroke recurrence. However, for CE strokes caused by AF, antiplatelets are only moderately effective compared to anticoagulant drugs^{56,57} but these can only be given after a diagnosis of AF is made.⁵⁵ Because AF can be paroxysmal, it is often not detected during a patient's short term hospital stay and patients are sent home to complete long-term cardiac monitoring with an ineffective therapy, thereby unnecessarily heightening their risk of stroke recurrence. Beyond this, in as many as 1 in 3 patients with AF the arrhythmia is not detected even after 30 days of at-home monitoring.⁵⁸

For LAA strokes, the arbitrary cutoff of >50% stenosis for diagnosis has been criticized as it incorrectly classifies those with less than 50% as a stroke of undetermined etiology, and may confound other classifications such as CE if a stenosis is found but is asymptomatic and unrelated to the stroke.⁵⁹ One study has found significant (>50%) stenosis in nearly 25% of ischemic stroke patients with AF; in these cases the stroke would also be classified stroke of undetermined etiology, due to multiple identified causes.⁶⁰

Overall, the methods used by clinicians today to deduce etiology are insensitive and unspecific; decisive criteria are neither definitive nor mutually exclusive and the origin of many strokes is never determined. As such, there is ample room for clinicians to consider additional information that may help inform their etiological diagnosis. A vast amount of

information contained within stroke thrombi, the underlying cause of ischemic stroke itself, is available to be leveraged but currently remains ignored within clinical practice.

1.5 Thrombus composition and its relationship to stroke etiology

There remains significant room for improvement in the determination of ischemic stroke etiology, and an area that has thus far being inadequately explored is the information present within the thrombus itself; its composition. An accumulation of histological studies have demonstrated a link between thrombus RBC content and stroke subtype. Knowledge of thrombus RBC content has the potential to guide and improve acute stroke care, but histological analysis is not possible to perform in the many cases where a thrombus is not retrieved. Rapid, non-invasive assessment through medical imaging is required for thrombus composition to be considered within acute stroke care.

Four major components constitute the vast majority of all thrombi: red blood cells (RBCs), fibrin, platelets, and white blood cells (WBCs). A schematic diagram depicting these components within stroke thrombi is shown in Figure 1-4. Thrombus formation is initiated by thrombin generation through either the collagen- (intrinsic) or tissue factor- (extrinsic) dependent pathways, which cause the development of fibrin strands from circulating fibrinogen segments as well as the activation of platelets that bind to and connect fibrin strands together to form a mesh-like structure.⁶¹ Platelet activation causes the recruitment of WBCs into the nascent thrombus, initiating an immunoinflammatory response which accompanies and regulates thrombus formation and dissolution.⁶² RBCs are incorporated into

thrombi via passive entrapment in the fibrin mesh, and the scope of their influence over thrombosis is still not fully understood.⁶³ Occasionally, additional components present at the site of thrombus formation, such as lipid in the form of cholesterol crystals and calcium hydroxyapatite from intravascular calcifications, may be incorporated into a thrombus as well.

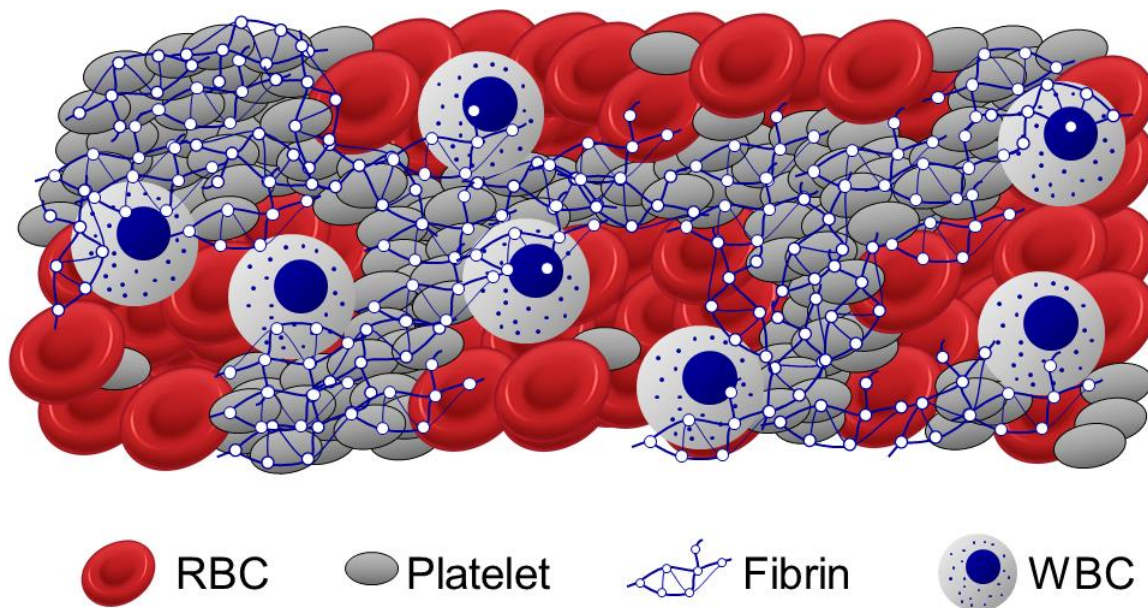


Figure 1-4: Schematic drawing of the typical components constituting stroke thrombi. Activated platelets connect fibrin strands to form a webbing which encapsulates RBCs, WBCs, and holds the thrombus together. Isolated pockets of RBCs tend to form within platelet/fibrin-rich regions with WBCs on the border between them.⁶⁴

The relative proportion of each of these components varies widely between thrombi, as they are influenced by the specific conditions under which thrombosis occurred. Variability in blood flow within stenotic vessels has been linked to heterogeneous deposition of platelets, for example.⁶⁵ Consequently, the composition of an embolic thrombus may be indicative of its source. Numerous studies have attempted to derive relationships between thrombus composition and stroke etiology; to do so histological analysis is used.

Histological examination involves the dehydration, embedding, slicing and staining of tissue samples for examination under a microscope. It provides the gold-standard assessment of tissue composition through microscopic resolution images of slides, which are stained to illuminate a wide array of cellular and non-cellular components. Hematoxylin and eosin (H&E) is the most common stain used for thrombus histological analysis; it uniquely identifies RBC and WBC components but cannot distinguish between fibrin and platelets. These stain images can be segmented to quantitatively assess the proportion of all components within a thrombus section. An example thrombus H&E stain image and segmentation is shown in Figure 1-5.

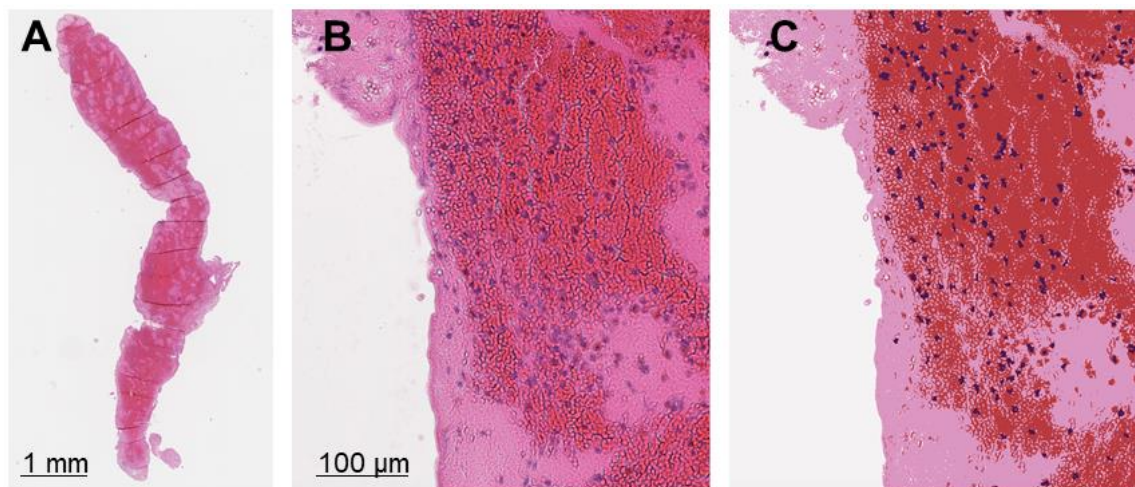


Figure 1-5: Example thrombus H&E section at low (A) and high (B) magnification with RBCs in red, fibrin/platelets in pink and WBCs in dark blue. An example segmentation output used to quantify thrombus composition is shown in (C). The typical thrombus has a composition of approximately 30, 60 and 10% RBCs, fibrin/platelets and WBCs, respectively.¹⁰ Note the heterogeneous distribution of components, with distinct deposits of RBCs and fibrin/platelets arranged throughout the thrombus.

With the advent of endovascular therapy greatly expanding the number of thrombi available for histological analysis, recent years have seen a dramatic increase in the number of studies examining the clinical implications of thrombus composition. A summary of the results of all current histological

studies examining the relationship between thrombus composition and stroke etiology are shown in the table below:

Table 1-1: Studies assessing the relationship between ischemic stroke etiology and histological composition of thrombi retrieved by endovascular therapy

Primary author	Year	No of patients	Analysis method	Differences between CE – LAA thrombi*
Marder ⁶⁶	2006	25	Qualitative categorization	None
Liebeskind ⁶⁷	2011	50	Semiautomated quantification	None
Sato ⁶⁸	2012	17 [†]	Semiautomated quantification	CE: ↑RBC; LAA: ↑fibrin
Boekh-Behrens ⁶⁹	2014	34	Semiautomated quantification	CE: ↑WBC
Niesten ⁷⁰	2014	22	Visual quantification	LAA: ↑RBC
Sallustio ⁷¹	2014	28	Qualitative categorization	None
Kim ⁷²	2015	37	Semiautomated quantification	CE: ↑RBC; LAA: ↑fibrin
Simons ⁷³	2015	40	Qualitative categorization	None
Ahn ¹¹	2016	36	Semiautomated quantification	CE: ↑fibrin; LAA: ↑RBC
Boeckh-Behrens ⁸	2016	137	Semiautomated quantification	CE: ↑fibrin/platelet,‡ ↑WBC; LAA: ↑RBC
Sporns ¹⁰	2017	187	Semiautomated quantification	CE: ↑fibrin/platelet,‡ ↑WBC; LAA: ↑RBC
Maekawa ⁷⁴	2018	43	Semiautomated quantification	CE: ↑fibrin; LAA: ↑RBC
Fitzgerald ⁷⁵	2019	105	Semiautomated quantification	LAA: ↑platelet

*Significant difference in thrombus area (%) between CE and LAA subtypes (p < 0.05); †Thrombi collected at autopsy; ‡Fibrin and platelets not differentiated in examination. CE, cardioembolism; LAA, large artery atherosclerosis; RBC, red blood cells; WBC, white blood cells.

Despite the lack of consensus, methodological differences in the approach of these histological studies are instructive. Of note is that the majority (3/4) of studies finding no difference in thrombus composition between subtypes performed only qualitative classification of thrombi (categorized into “fibrin enriched,” “serpentine,” “erythrocytic”, “layered” etc.), rather than employing some form of automated quantification of each component’s proportion. Among those that did perform quantitative assessment, the trends of early studies indicating CE thrombi having a higher proportion of RBCs directly oppose those of more recent studies indicating a higher proportion of fibrin, and less RBCs, in that same subtype. This shift could be explained by improvement in endovascular therapy devices and general operator experience increasing the proportion of thrombi retrieved as the therapy became more widespread. Early studies also tended to have smaller sample sizes than more recent ones. The consensus within recent studies suggests that a lower RBC and higher fibrin proportion is expected in thrombi caused by CE compared to those caused by LAA. It is worth noting that all studies in general found a trend of higher RBC levels in thrombi with low fibrin content, and vice-versa, indicating that these components are inversely related and are the principle sources of variation within stroke thrombus composition.

Beyond the primary thrombus components, a few studies have identified the presence of lipid^{45,76} or calcium^{77,78} within thrombi and drawn relations to etiology. Lipid was found only in thrombi derived from LAA, while calcium was found only in thrombi derived from LAA or following an invasive cardiac procedure (suggesting disruption of a calcified cardiac valve), indicating that the presence of either of these components may be directly predictive of LAA stroke etiology in the absence of a preceding surgical procedure.

There is strong evidence to support that thrombus composition may be a useful property for determining stroke etiology. However, histological

analysis is an involved process and can only be completed for patients in which a thrombus is retrieved, making it inappropriate for wide use within clinical care. Only 30-40% of ischemic stroke patients present with an occlusion large enough for endovascular therapy to be feasible, and just 25% of these patients are ultimately eligible for the therapy.^{79,80} Within these eligible patients 80% will have thrombi retrieved, meaning only 7% of ischemic stroke patients overall have thrombi available for histological study.⁸¹ Medical imaging offers the potential to noninvasively infer thrombus properties regardless of retrievability including but not limited to thrombus composition, however it presents its own unique set of challenges. The following section examines past attempts to leverage medical imaging to predict ischemic stroke thrombus composition and etiology, as well as the limitations associated with each technique.

1.6 Imaging inference of thrombus composition and etiology

Both MR and CT imaging are capable of assessing thrombus RBC content via their sensitivity to iron within the hemoglobin molecule. A number of previous studies have used qualitative MR or CT imaging signs to characterize thrombi and have demonstrated an association with RBC content. However, these signs have collectively proven unable to predict stroke etiology. With MR imaging, sensitivity to RBC oxygenation may confound qualitative predictions; quantitative MR approaches including R_2^ and quantitative susceptibility mapping may provide a basis to assess RBC content independent of oxygenation. However, typical statistical measures derived from quantitative thrombus images may not be sufficient for etiology*

prediction, and more advanced techniques that account for intra-thrombus heterogeneity may be required.

Coincident with stroke thrombus histological studies, medical imaging studies have been performed examining the relationship between thrombus imaging properties, composition and etiology. Both MR and CT imaging are sensitive to the iron atoms inside RBC hemoglobin, allowing non-invasive interrogation of RBC content.^{82,83} Qualitative and quantitative imaging characterization techniques have been developed and are described in the following subsections.

1.6.1 Qualitative thrombus MR characterization

In MR imaging, the hemoglobin iron atom possesses a high magnetic susceptibility which causes local field inhomogeneity, spin dephasing and ultimately signal loss. Importantly, this effect occurs only when hemoglobin is not bound to oxygen; this increases MR sensitivity to stroke thrombi relative to circulating blood, as tissue ischemia leads to reduced oxygen content in thrombi relative to oxygenated arterial blood.⁸² The presentation of a dark signal void resultant from deoxyhemoglobin within a stroke thrombus on gradient echo (GRE) imaging is referred to as a susceptibility vessel sign (SVS) (Figure 1-6).⁸⁴

In non-contrast CT imaging, iron's high electron density leads to elevated photon attenuation relative to tissue, resulting in higher signal. CT signal intensity is measured in Hounsfield units (HU), and RBC content has been correlated to CT HU values in blood clots *in vitro*.⁸⁵ However, unlike MR imaging, CT's sensitivity to hemoglobin is independent of RBC oxygenation state, and it is therefore equally sensitive to iron inside thrombi as in circulating blood, resulting in a lower relative sensitivity to stroke thrombi than that of MR.⁸⁶ The presence of bright signal inside a stroke thrombus on

non-contrast CT imaging is referred to as a hyperdense artery sign (HDAS) (Figure 1-6).⁸⁷ Numerous studies have demonstrated a relationship between the presence of both the SVS and HDAS and stroke thrombus RBC content.^{67,88,89}

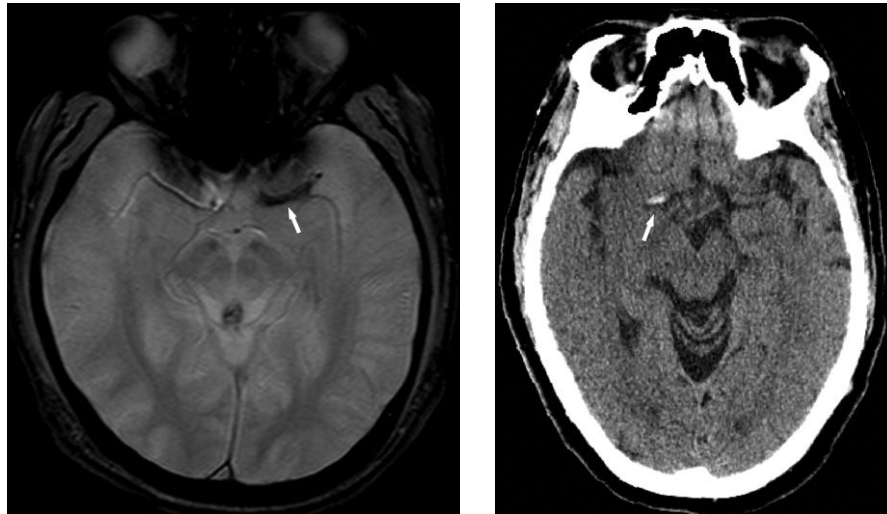


Figure 1-6: Neurological MR (left) and CT (right) images of stroke patients demonstrating qualitative thrombus imaging signs; SVS and HDAS, respectively. Figures from Liebeskind et al., reproduced with permission.⁶⁷

A number of studies have employed these qualitative imaging signs to search for a relationship with stroke etiology.⁹⁰⁻⁹² While certain studies have derived significant associations, with most linking positive imaging signs to CE stroke, a recent meta-analysis of these studies found no statistically significant relationship overall between either SVS or HDAS and stroke etiology.⁹³ These qualitative imaging assessments are limited by their ability to provide only binary information, and have demonstrated issues with intra-observer and intra-scanner variability.⁹⁴ Quantitative MR imaging methods have been investigated as a means to provide more advanced imaging characterization of stroke thrombi, while reducing reliance on individual interpretation. The quantitative MR metrics employed for thrombus characterization in this thesis include effective transverse relaxation time (R_2^*) and quantitative susceptibility mapping (QSM).

1.6.2 Effective transverse relaxation time (R_2^*)

Disruption of the main MR magnetic field (B_0) homogeneity by RBC deoxyhemoglobin leads to transverse signal dephasing and signal loss. This effect is quantifiable by measurement of the rate of signal loss in a signal decay curve, a plot of voxel magnitude values obtained across multiple echo times. In GRE imaging the signal decay rate corresponds inversely to the effective transverse relaxation time, known as R_2^* ($=1/T_2^*$), and is commonly derived through an exponential fit of the signal decay curve (Figure 1-7).

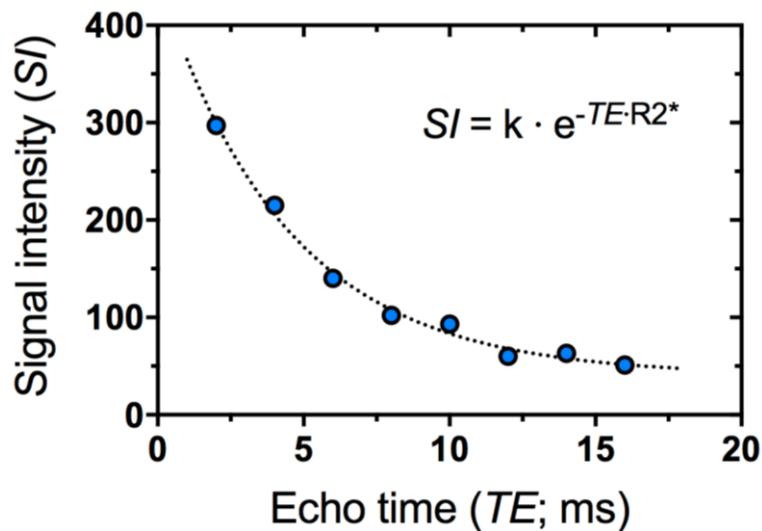


Figure 1-7: Example signal decay curve with an exponential curve fit. Higher R_2^* values correspond to more rapidly decaying signal.

While straightforward to perform, the exponential fit technique can lead to erroneous R_2^* values in voxels with very rapid signal decay, and the observed signal evolution can be influenced by several other factors including underlying B_0 inhomogeneity and the presence of fat tissue. Because of this, more advanced signal processing methods have been developed which model R_2^* , B_0 inhomogeneity and fat fraction (FF) simultaneously, though accurate FF mapping was the primary focus of these techniques rather than R_2^* .^{95,96} The B_0 -NICE method, developed in the Drangova lab, also models R_2^* , B_0 field and FF and was designed to output accurate measurements of all

three.⁹⁷ B0-NICE uses a non-iterative lookup table approach to R_2^* mapping which is less susceptible to underestimation of R_2^* values in voxels with rapid signal loss, and is the algorithm used to quantify thrombus R_2^* in this thesis. The B0-NICE FF maps were additionally used to assess thrombus lipid content.

1.6.3 Quantitative susceptibility mapping

The mechanism through which the deoxyhemoglobin iron atom disrupts the B0 field is through a bending of its magnetic field force lines, changing the strength of the field inside and around it (Figure 1-8). All materials interact with and alter magnetic field lines to some extent; the parameter that quantifies the degree of this alteration is known as magnetic susceptibility. Materials which increase the strength of the local field are known as paramagnetic while those that decrease it are known as diamagnetic. Water, the main component of human tissue, has a diamagnetic susceptibility of -9.04 ppm, while RBC deoxyhemoglobin is paramagnetic relative to water with a magnetic susceptibility of -5.61 ppm, commonly written as a +3.43 ppm relative shift.⁹⁸ Oxyhemoglobin has a comparatively negligible -0.1 ppm diamagnetic shift relative to water.

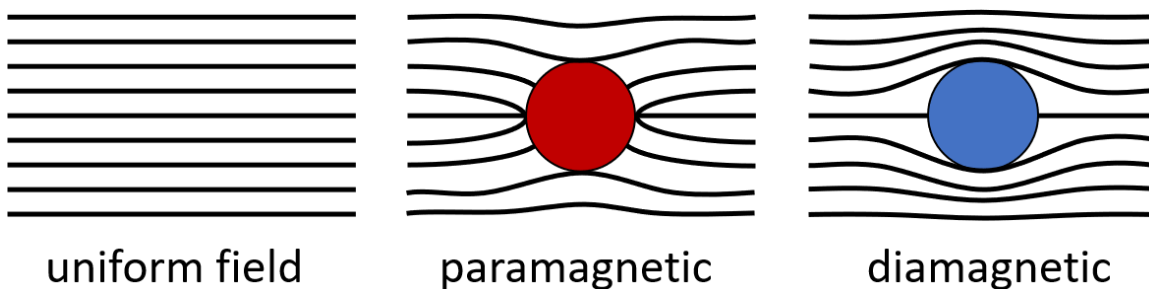


Figure 1-8: A uniform magnetic field in the presence and absence of magnetic material. Paramagnetic materials have a positive magnetic susceptibility and attract magnetic lines of force, while diamagnetic materials have a negative susceptibility and repel them.

A material's magnetic susceptibility directly influences the strength of the magnetic field it observes in addition to those of the atoms surrounding it. While high intravoxel susceptibility variation leads to the signal loss quantifiable by R_2^* mapping, direct estimation of a material's magnetic susceptibility is also possible through a technique known as quantitative susceptibility mapping. Background field contributions to local phase are first removed to produce a local frequency shift map which is converted to a QSM map through an inversion process involving deconvolution of the dipole kernel. This inversion process is ill-posed however in that certain regions of the dipole kernel are undefined, meaning there are an infinite number of potential inversion solutions. QSM algorithms overcome this by incorporating prior information into the inversion; strategies differ across the multitude of QSM algorithms that have been developed though enforcing spatial smoothness in the estimated QSM map through regularization is the typical added condition.^{99,100} One of the most widely used QSM algorithms, known as morphology enabled dipole inversion (MEDI), explicitly matches spatial gradients within input magnitude images to gradients in the estimated QSM map, penalizing the formation of streaking artifact edges that plague many QSM reconstructions.¹⁰¹ MEDI is the QSM algorithm used to analyze thrombus magnetic susceptibility in this thesis.

1.6.4 Quantitative thrombus MR characterization

Direct assessment of R_2^* and QSM from multi-echo GRE acquisitions has been previously performed on prepared blood clots *in vitro* and demonstrated sensitivity to both blood clot RBC content and oxygenation, as expected (example shown in Figure 1-9).^{102,103} However, no study has quantified these MR values on blood clots of simultaneously varied composition and oxygenation, meaning that any translation of the derived relationships to stroke thrombi will be confounded by the codependence of R_2^* and QSM on both factors. The second chapter of this thesis describes an *in vitro* study

designed to bridge this gap by deriving a quantitative relationship between blood clot R_2^* and QSM that can be used to predict clot RBC content independent of oxygenation.

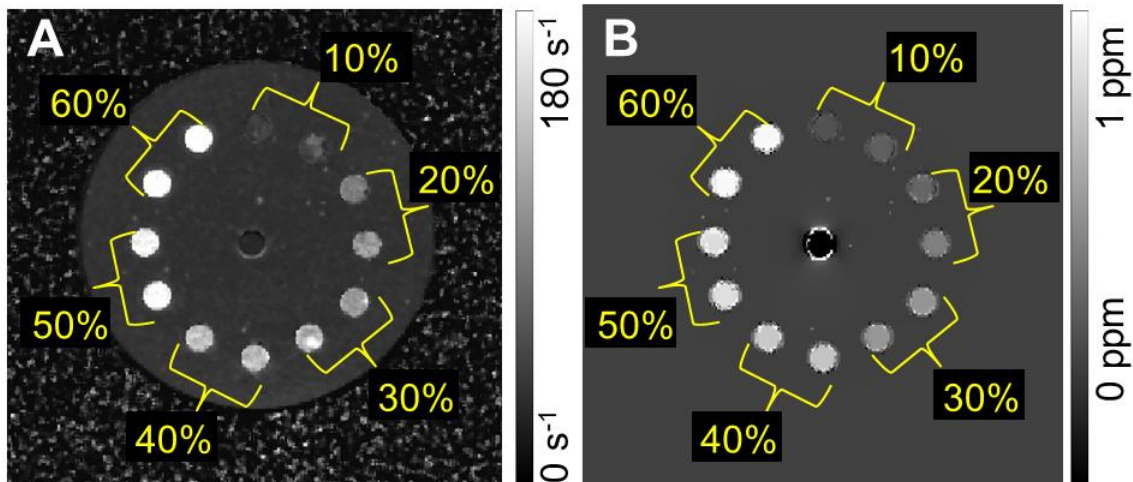


Figure 1-9: MR R_2^* (A) and QSM (B) maps of a phantom containing pairs of deoxygenated blood clots prepared *in vitro* of 10-60% RBC content (yellow label) with the remainder being composed of fibrin and platelets.

Assessment of the relationship between thrombus R_2^* and QSM and stroke etiology remains limited. A single study has been completed that found no significant difference in mean thrombus R_2^* between stroke etiologies.¹⁰⁴ These inconclusive findings may be the result of small sample size (only 4 LAA thrombi studied), but may also be indicative of a more fundamental weakness. Traditionally, quantitative imaging studies have used a single imaging value or metric to represent an entire sample, while histological studies of stroke thrombi have consistently shown that they are heterogeneously composed, with varied concentrations of their components throughout their structure. Intrathrombus compositional heterogeneity is observable with quantitative MR maps (Figure 1-10), at the scale of the acquired image resolution, and as such more complex image analysis methods sensitive to thrombus texture and morphology may allow more effective characterization of stroke thrombi. The following section describes artificial intelligence techniques, specifically machine and deep learning, and

their potential to extract detailed intra-thrombus information from quantitative MR images for improved prediction of stroke thrombus composition and etiology.

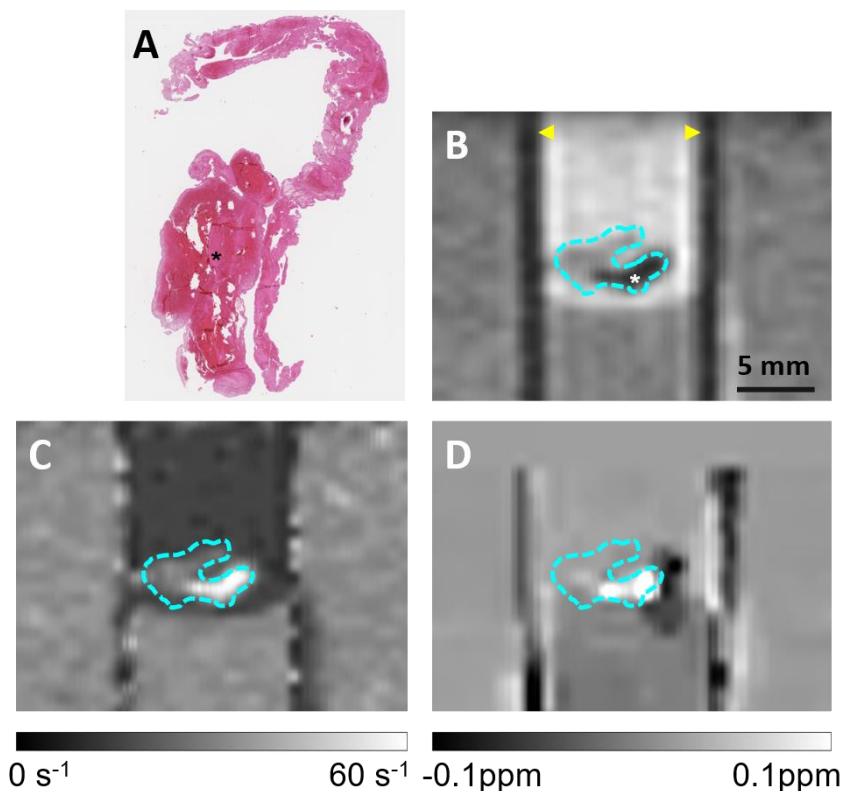


Figure 1-10: Example thrombus (A) H&E histology slide (RBCs stain red; fibrin/platelets stain pink) along with a corresponding slice of its (B) GRE magnitude (TE = 31 ms), (C) R_2^* and (D) QSM maps. MR images are shown in a coronal view, with the vertical scanning vial walls indicated with ► and the thrombus outlined in cyan. Agar fills the space below the thrombus and outside the vials. * indicates the RBC-rich body of the thrombus which has a noticeably lower magnitude signal and higher R_2^* and QSM values than its fibrin-rich tail.

1.7 Artificial intelligence and potential for advanced thrombus analysis

Artificial intelligence is a powerful tool that may be able to retrieve a greater level of information from images of thrombi than traditional imaging metrics can provide, specifically by interpreting intra-thrombus texture and morphological information. Machine learning and deep learning are two fields within artificial intelligence that have seen rapid growth in recent years due to improved computing resources, as well as mounting proof of utility within the medical imaging field. Machine learning makes explicit use of imaging-derived texture features, while deep convolutional neural networks are capable of deriving their own abstract features from raw images as input. These complimentary techniques have each demonstrated capability for providing valuable information related to stroke, but have seen very little, if any, application towards the study of stroke thrombi. Evidence suggests that they are powerful tools which may allow for more accurate characterization of thrombi than that possible using traditional techniques.

Artificial intelligence describes the use of machines to perform tasks normally considered to require human intelligence, such as visual perception, decision-making, or problem solving. In the context of medical imaging, artificial intelligence allows the extraction of rich sets of information from quantitative imaging data beyond simple statistical measures such as mean, variance, inter-quartile ratio etc., such as measures related to object texture and morphology. As mentioned in the previous section, there is histological justification for consideration of thrombus texture, given the heterogeneous composition of most stroke thrombi. As thrombus composition is known to be influenced by the environmental conditions under which they are formed, interpretation of intra-thrombus information may yield deeper insight into their history. Lines of Zahn, alternating wave-like laminations of platelets

and fibrin interspersed between waves of RBCs, and outer shells of condensed fibrin and aggregated platelets, have each been hypothesized to relate to changes in blood flow and pressure as a thrombus forms.^{65,105} Subject to the resolution limits of the input, artificial intelligence algorithms may be able to interpret subtle thrombus texture or shape features which are informative of its formation, and in doing so may allow both a finer characterization of thrombus RBC content and better prediction of etiology. The following sections describe in more detail two important forms of artificial intelligence, machine and deep learning, and their respective properties suited for thrombus analysis.

1.7.1 Machine learning

A subset of artificial intelligence, known as machine learning, refers to the use of computer algorithms, which automatically improve through experience. Typically, machine learning is applied in the context of supervised learning for classification or regression problems, wherein a computer is trained on labelled data with the aim of deriving a model, which can accurately predict a desired class or value from new, unseen data. A vast array of machine learning algorithms have been developed; a recent, exhaustive review evaluated 179 algorithms within 17 different families (discriminant analysis, Bayesian, neural networks, support vector machines, decision trees, rule-based classifiers, boosting, bagging, stacking, random forests, generalized linear models, nearest neighbours, partial least squares and principal component regression, logistic and multinomial regression, multiple adaptive regression splines and other methods) for performing classification on 121 datasets.¹⁰⁶ The review found the random forest classifier provided the best general performance and this algorithm will be described in further detail in this section, while neural networks will be described in the following section as a segue into deep learning.

Random forests consist of an ensemble of decision trees, which are tree-like chains of ordered binary decision nodes designed to learn to deduce a desired output value from input features derived from the dataset (e.g. age, colour, price). Decision trees generate criteria at each node using the input features to create a binary logic model; the computer derives the tree that most accurately categorizes the training dataset to align with its desired outcome variable. A random forest is created from multiple decision trees each trained on a randomly sampled subset of the dataset. In doing so, random forests overcome the tendency for single decision trees to overfit to its training data.¹⁰⁷ When forming predictions on unseen testing data, the result of each decision tree is utilized to ‘vote’ on the predicted class or value; the random forest outputs the most voted for class or average value for each observation within the dataset (Figure 1-11).

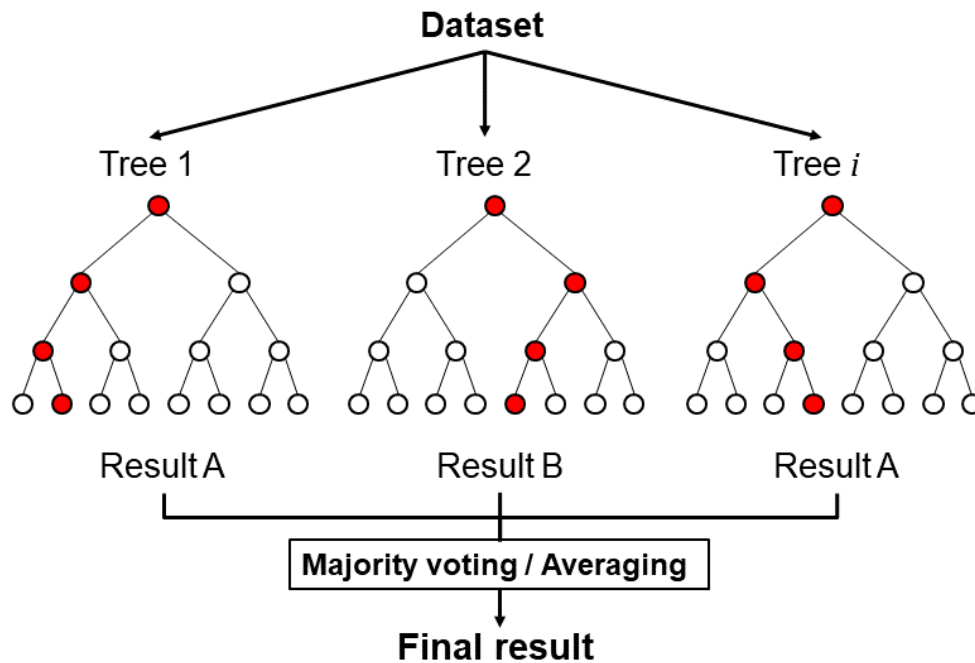


Figure 1-11: Schematic diagram of the random forest classifier.

Regardless of the algorithm used, machine learning is dependent on the quality of the input features for deriving a useful model capable of generating accurate predictions. The ideal input dataset contains a rich feature set of

multiple independent predictors of the desired outcome variable; in practice, the independence and predictivity of each input feature is almost always unknown and consequently large initial feature sets are desirable. From this initial, unrefined feature set a process termed feature selection is performed to identify the subset of features most predictive of the outcome variable. Typically, some form of linear regression, wherein features are correlated to each other and to the outcome variable to identify the features which are most independent and predictive, is used.

Within the field of medical imaging, the extraction of quantitative features from images is known as radiomics.¹⁰⁸ Radiomics features can consist of relatively simple, first-order statistical descriptors such intensity, size or shape measurements, but these features don't tend to provide information that isn't already perceivable by a trained observer. In contrast, texture features, second-order descriptors, which quantify the statistical interrelationships between voxels, can identify trends and relationships imperceptible to the human eye. Texture features are calculated from statistical matrices, most typically those tabulating the co-occurrence of pairs of pixel values (gray level co-occurrence; example in Figure 1-12), or commonality of runs of a particular pixel value (gray level run length). A near endless amount of texture features may be generated from these matrices but the typical starting point are the Haralick texture features, the first set of texture features applied for image analysis and described by Haralick in 1973.¹⁰⁹

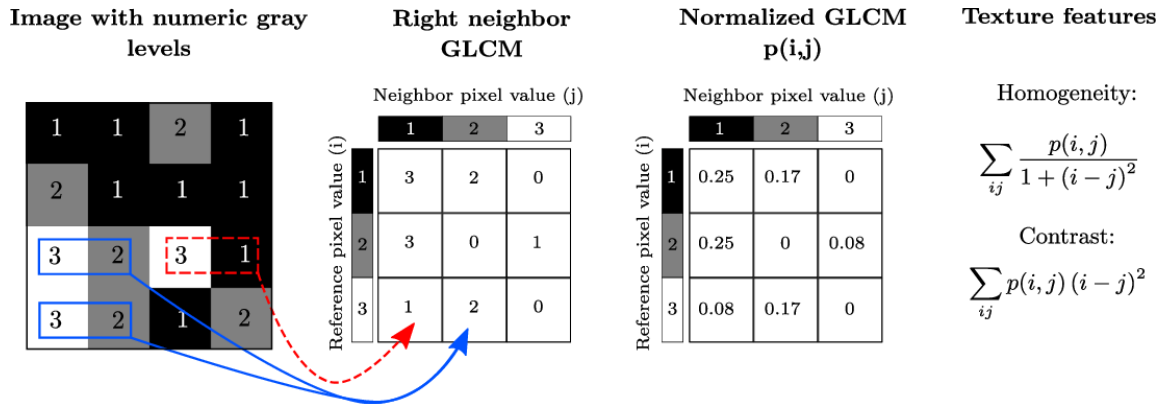


Figure 1-12 Diagram showing an example of texture feature value calculation from a second-order statistical matrix. The total number of co-occurring pairs of pixels across one direction in an image is used to create a gray level co-occurrence matrix (GLCM), whose normalized values are used for the calculation of texture feature values. Figure from Brynolfsson et al., reproduced with permission.¹¹⁰

Machine learning algorithms applied to radiomics texture features extracted from medical images have shown utility in a wide array of pathologies, but have shown particular usefulness in the field of oncology. Texture features have been used to predict tumour phenotype, histological grade, metastasis, and patient outcome, using random forest classifiers and multivariate Cox regression models.¹¹¹⁻¹¹⁴ Texture features have also demonstrated utility in stroke, where they have been used as input for machine learning algorithms to predict post-stroke impairment and detect lesions using support vector machine classifiers.^{115,116} Though currently limited in scope, research has been produced showing promise for texture features in thrombus analysis; two studies applied them to predict blood clot RBC content *in vitro*, with one study using decision trees and another directly correlating features to RBC content.^{117,118} Two studies have applied this technique to acute stroke thrombi, and showed ability to predict response to rtPA and endovascular therapies, respectively, from patient CT images *in vivo* using support vector machine classifiers.^{119,120}

Texture features quantify image heterogeneity, and despite promising results from algorithms applied to thrombus CT data, machine learning algorithms have not been previously applied to stroke thrombi for the prediction of etiology, a task where measures of intra-thrombus heterogeneity seem particularly suited. A study utilizing a random forest classifier on texture features derived from *ex vivo* MR images of acute ischemic stroke thrombi for etiology prediction is described in the 4th chapter of this thesis. The following section describes a subset of machine learning which has seen an explosion of interest in recent years following advancements in computing technology, deep learning, and the unique properties it possesses that make it a complementary tool to machine learning for thrombus characterization. To introduce the topic a description of the machine-learning algorithm that forms the nexus of deep learning, the neural network, is first given.

1.7.2 Neural networks and deep learning

Originally described by Frank Rosenblott in the 1950's, the single layer perceptron was the earliest form of neural network; a modelling system designed to mimic the structure of neurons within the human brain.¹²¹ Beginning with an input layer built of separate neurons for each input feature, the perceptron's input neurons are fully connected to a hidden layer of neurons themselves connected to a binary output layer (Figure 1-13). Associated with each connection is a weight parameter that quantifies the level of influence each neuron has on the output of those it is connected to. In iteratively updating these weight parameters based on the difference between the desired and predicted output, a process known as network tuning, the perceptron learns to separate between two classes of data. A single layer perceptron is a binary linear predictor function, and is therefore capable of differentiating only between linearly separable data classes.

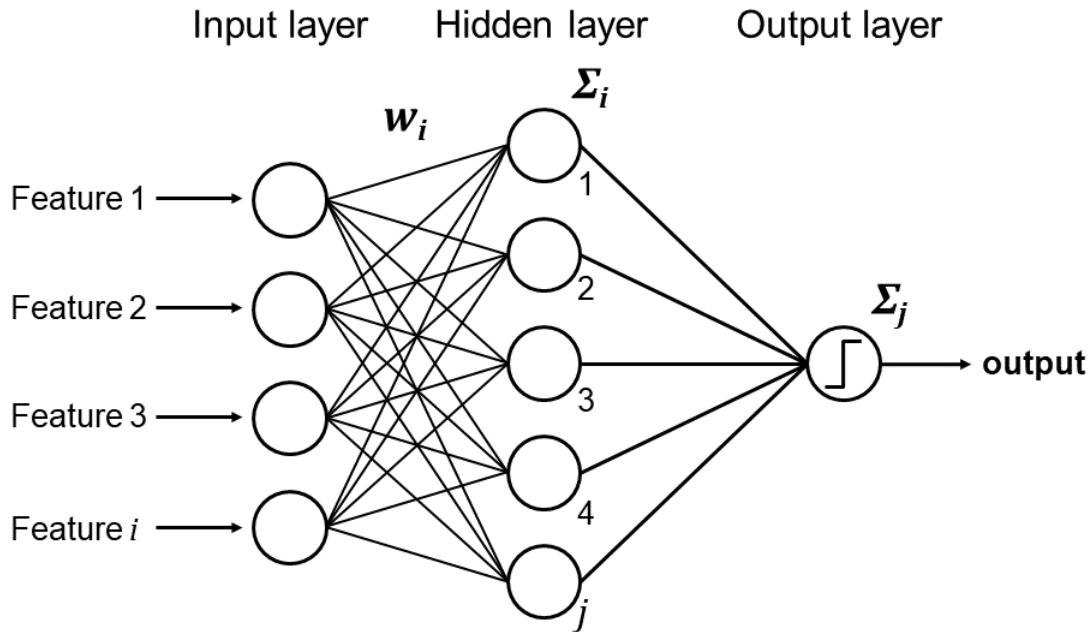


Figure 1-13: Schematic diagram of the simple perceptron. Each connection between the input layers and the hidden layer nodes is associated with a tuneable weight parameter (w_i). Each hidden layer node performs a weighted sum of all input features (Σ_i), which themselves are summed (Σ_j) by the output layer. The output is determined to be true or false based on a binary output function.

From this relatively simple starting point, more complicated neural networks capable of performing drastically more complex operations have evolved, becoming known as deep neural networks. While there this is no formal definition specifying precisely when a neural network becomes complex enough to be considered ‘deep’, certain advancements made in neural network design since the perceptron was first described have today become their essential properties. The inclusion of more than one hidden layer has become the *de facto* defining property of deep networks, as it is necessary to allow non-linear separation of data classes and enables more complex feature extraction, while backpropagation allows for drastically more efficient network tuning by allowing information from the gradient of the error function at deeper levels to be reused by more superficial ones. Increasingly deeper networks are capable of learning more abstract features from input

data, to the point that handpicked, predictive input features sets are no longer required and networks are capable of deriving their own predictive features from comparatively raw data. Modern improvements to computing resources and greater access to large datasets for training have, in recent years, enabled deep neural networks to become drastically more practical and powerful.

Within the rapid expansion of the deep learning field over the past decade, deep learning networks designed to handle images in particular have risen in prominence. These networks are called deep convolutional neural networks (CNNs), as they use learnable convolutional filters, which extract increasingly more complex patterns and features from image data. In doing so, they learn to perform a mapping of high dimensional input data (image) to a desired output. Over the past few years, a number of tools were developed to improve CNN performance that have since become standard in modern implementations. Non-linear activation functions (typically rectified linear units (ReLU)) allow CNNs to learn features complex enough to effectively interpret high dimensional input. Pooling and padding allow a reduction or increase, respectively, in the dimensionality of the feature maps allowing greater network flexibility. Batch normalization is the process of normalizing the output of each activation layer and allows the network to learn more quickly and avoid divergence. Dropout is the random removal of certain output nodes, which regularizes the network, increasing generalizability and preventing overfitting. The structure of a typical modern CNN is depicted in Figure 1-14. Improvements in CNN design have greatly increased their capability, and spurred translation of the technique from traditional computer vision tasks such as character recognition,¹²² object detection¹²³ and image classification¹²⁴ into the field of medical imaging.

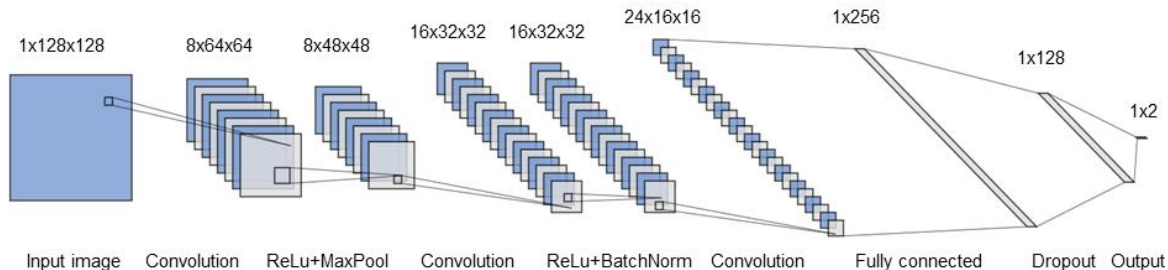


Figure 1-14: Architecture of a modern CNN. Three convolutional layers are separated by ReLu's and max pooling and/or batch normalization functions, followed by a fully connected layer with dropout before the final output layer.

CNNs have been used for a diverse array of medical imaging applications, ranging from detecting metastases in the brain to classifying ulcers in the feet.^{125,126} In the field of stroke imaging, interest has piqued in the use of CNNs for analysis of neurological stroke images, for the detection and segmentation of stroke lesions and identification of penumbral tissue, for example.^{127,128} The singular strength of deep neural networks comes from their ability to derive their own abstract features, making them particularly suited for problems where relevant imaging features are difficult to define. To this end, CNNs have been used to abstrusely predict stroke patient prognosis, ischemic tissue outcome, and stroke onset time.¹²⁹⁻¹³¹

Characterization of stroke thrombi is another area where relevant imaging features are challenging to define, and hence is suited to analysis by deep learning networks. The interaction between RBC content and oxygenation on quantitative MR imaging values is complex and may be difficult to capture with traditional machine learning texture features in the context of thrombus composition inference. Deep learning has not been previously applied towards the analysis of human stroke thrombi, and the application of a deep CNN for the prediction of acute stroke thrombus RBC content using *ex vivo* MR images is presented in the 3rd chapter of this thesis.

1.8 Thesis hypotheses and objectives

Despite marked improvement in stroke diagnosis and treatment in recent years, acute ischemic stroke remains a major source of disability and mortality across the world. Improvement in any facet of stroke care is always desirable, but a particularly significant gap exists in the determination of stroke etiology, a critical characteristic necessary for optimal post-stroke management. Medical imaging is today a cornerstone of stroke care, but is underutilized relative to its potential to compensate for weaknesses in the current paradigm. Histological studies have identified compositional patterns that link stroke thrombi to its underlying etiology, and while medical imaging techniques have demonstrated a qualitative sensitivity to RBC content, they have been thus far unable to provide accurate, quantitative prediction of thrombus RBC content or etiology. The hypothesis of this thesis is that quantitative MR imaging, specifically that focused on R_2^* and QSM mapping, is capable of accurately characterizing ischemic stroke thrombus RBC content and etiology through the application of machine and deep learning image analysis algorithms. This thesis consists of 5 Chapters designed to explore and support this hypothesis, the 1st consisting of this introductory description of the field.

In the 2nd chapter, an *in vitro* study is presented which consists of a cohort of blood clots prepared with varied RBC content and scanned serially over 6 days as their oxygenation status evolves. The objective of this work was to demonstrate that MR R_2^* and QSM parameters are each sensitive to RBC content and may be used in conjunction to allow prediction of RBC content independent of oxygenation state. The second objective of this work was to show that QSM and fat fraction (FF) mapping are capable of detecting calcified and lipidic components inside thrombi.

In the 3rd chapter, a deep learning study is presented which involves the use of a deep CNN trained to predict RBC content using *ex vivo* MR images of retrieved acute ischemic stroke thrombi. The objective of this work was to demonstrate that CNNs are capable of learning to accurately predict RBC content in human thrombi from R_2^* and QSM thrombus maps, and support the notion that further improvements in prediction accuracy are achievable with sufficient sample size and data augmentation.

In the 4th chapter, a machine learning study is presented which utilizes radiomics texture features extracted from *ex vivo* MR images of retrieved acute ischemic stroke thrombi to predict stroke etiology using a random forest classifier. The objective of this work was to demonstrate that accurate prediction of stroke etiology is possible through machine learning analysis of texture features extracted from thrombus R_2^* , QSM and FF maps, and investigate whether predictions can be improved through the incorporation of clinical patient data.

The thesis concludes with a brief summary and suggestions for future work.

1.9 References

1. Feigin VL, Norrving B, Mensah GA. Global burden of stroke. *Circul Res* 2017;120:439-448.
2. Heart_and_Stroke_Foundation. 2014 Stroke Report. 2014. Available at http://www.strokebestpractices.ca/wp-content/uploads/2014/06/HSF_SMReport2014E_Final.pdf (accessed August 2018).
3. Sposato LA, Kapral MK, Fang J, et al. Declining incidence of stroke and dementia: coincidence or prevention opportunity? *JAMA neurology* 2015;72:1529-1531.
4. Boysen G, Truelsen T. Prevention of recurrent stroke. *Neurol Sci* 2000;21:67-72.
5. Mohan KM, Wolfe CD, Rudd AG, Heuschmann PU, Kolominsky-Rabas PL, Grieve AP. Risk and cumulative risk of stroke recurrence: a systematic review and meta-analysis. *Stroke* 2011;42:1489-1494.
6. Coull AJ, Rothwell PM. Underestimation of the early risk of recurrent stroke: evidence of the need for a standard definition. *Stroke* 2004;35:1925-1929.
7. Krueger H, Koot J, Hall RE, O'callaghan C, Bayley M, Corbett D. Prevalence of individuals experiencing the effects of stroke in Canada: trends and projections. *Stroke* 2015;46:2226-2231.
8. Boeckh-Behrens T, Kleine JF, Zimmer C, et al. Thrombus histology suggests cardioembolic cause in cryptogenic stroke. *Stroke* 2016;47:1864-1871.
9. Rudkin S, Cerejo R, Tayal A, Goldberg MF. Imaging of acute ischemic stroke. *Emerg Radiol* 2018;25:659-672.
10. Sporns PB, Hanning U, Schwindt W, et al. Ischemic Stroke: What Does the Histological Composition Tell Us About the Origin of the Thrombus? *Stroke* 2017;48:2206-2210.
11. Ahn SH, Hong R, Choo IS, et al. Histologic features of acute thrombi retrieved from stroke patients during mechanical reperfusion therapy. *Int J Stroke* 2016;11:1036-1044.

12. Powers WJ, Rabinstein AA, Ackerson T, et al. 2018 guidelines for the early management of patients with acute ischemic stroke: a guideline for healthcare professionals from the American Heart Association/American Stroke Association. *Stroke* 2018;49:e46-e99.
13. Astrup J. Thresholds in cerebral ischemia: the ischemic penumbra. *Stroke* 1981;12:723-725.
14. Qureshi AI, Mendelow AD, Hanley DF. Intracerebral haemorrhage. *Lancet* 2009;373:1632-1644.
15. Jauch EC, Al Kasab S, Stettler B. Ischemic Stroke. New York, NY, Medscape, 2018. Available at <https://emedicine.medscape.com/article/1916852-overview> (accessed August 2018).
16. Williams GR, Jiang JG, Matchar DB, Samsa GP. Incidence and occurrence of total (first-ever and recurrent) stroke. *Stroke* 1999;30:2523-2528.
17. Shi Y, Wardlaw JM. Update on cerebral small vessel disease: a dynamic whole-brain disease. *Stroke Vasc Neurol* 2016;1:83-92.
18. Zakhari N, Castillo M, Torres C. Unusual cerebral emboli. *Neuroimaging Clin N Am* 2016;26:147-163.
19. Dijkhuizen RM, Rosen BR, Lo EH. Rapid breakdown of microvascular barriers and subsequent hemorrhagic transformation after delayed recombinant tissue plasminogen activator treatment in a rat embolic stroke model. *Stroke* 2002;33:2100-2104.
20. Murphy TH, Corbett D. Plasticity during stroke recovery: from synapse to behaviour. *Nature reviews neuroscience* 2009;10:861-872.
21. Theofanidis D. From apoplexy to brain attack, a historical perspective on stroke to date. *J Nurs Care* 2015;04:e121.
22. Disorders NIoN, Group Sr-PSS. Tissue plasminogen activator for acute ischemic stroke. *New Engl J Med* 1995;333:1581-1588.
23. Nilsen ML. A historical account of stroke and the evolution of nursing care for stroke patients. *J Neurosci Nurs* 2010;42:19-27.
24. Hacke W, Donnan G, Fieschi C, et al. Association of outcome with early stroke treatment: pooled analysis of ATLANTIS, ECASS, and NINDS rt-PA stroke trials. *Lancet* 2004;363:768-774.

25. Hacke W, Kaste M, Bluhmki E, et al. Thrombolysis with alteplase 3 to 4.5 hours after acute ischemic stroke. *New Engl J Med* 2008;359:1317-1329.
26. Von Kummer R, Bourquain H, Bastianello S, et al. Early prediction of irreversible brain damage after ischemic stroke at CT. *Radiology* 2001;219:95-100.
27. Larrue V, von Kummer R, Muller A, Bluhmki E. Risk factors for severe hemorrhagic transformation in ischemic stroke patients treated with recombinant tissue plasminogen activator: a secondary analysis of the European-Australasian Acute Stroke Study (ECASS II). *Stroke* 2001;32:438-441.
28. Schlaug G, Benfield A, Baird A, et al. The ischemic penumbra operationally defined by diffusion and perfusion MRI. *Neurology* 1999;53:1528-1528.
29. Sorensen AG, Buonanno FS, Gonzalez RG, et al. Hyperacute stroke: evaluation with combined multisection diffusion-weighted and hemodynamically weighted echo-planar MR imaging. *Radiology* 1996;199:391-401.
30. Baird AE, Benfield A, Schlaug G, et al. Enlargement of human cerebral ischemic lesion volumes measured by diffusion-weighted magnetic resonance imaging. *Ann Neurol* 1997;41:581-589.
31. Albers GW, Thijs VN, Wechsler L, et al. Magnetic resonance imaging profiles predict clinical response to early reperfusion: the diffusion and perfusion imaging evaluation for understanding stroke evolution (DEFUSE) study. *Ann Neurol* 2006;60:508-517.
32. Davis SM, Donnan GA, Parsons MW, et al. Effects of alteplase beyond 3 h after stroke in the Echoplanar Imaging Thrombolytic Evaluation Trial (EPITHET): a placebo-controlled randomised trial. *Lancet Neurol* 2008;7:299-309.
33. Boulanger J, Lindsay M, Gubitz G, et al. Canadian stroke best practice recommendations for acute stroke management: prehospital, emergency department, and acute inpatient stroke care, update 2018. *Int J Stroke* 2018;13:949-984.
34. Lansberg MG, Straka M, Kemp S, et al. MRI profile and response to endovascular reperfusion after stroke (DEFUSE 2): a prospective cohort study. *Lancet Neurol* 2012;11:860-867.

35. Campbell BCV, Christensen S, Levi CR, et al. Comparison of computed tomography perfusion and magnetic resonance imaging perfusion-diffusion mismatch in ischemic stroke. *Stroke* 2012;43:2648-2653.
36. Campbell BC, Mitchell PJ, Yan B, et al. A multicenter, randomized, controlled study to investigate EXtending the time for Thrombolysis in Emergency Neurological Deficits with Intra-Arterial therapy (EXTEND-IA). *Int J Stroke* 2014;9:126-132.
37. Casaubon LK, Boulanger J-M, Blacquièrè D, et al. Canadian stroke best practice recommendations: hyperacute stroke care guidelines, update 2015. *Int J Stroke* 2015;10:924-940.
38. Nogueira RG, Jadhav AP, Haussen DC, et al. Thrombectomy 6 to 24 hours after stroke with a mismatch between deficit and infarct. *New Engl J Med* 2018;378:11-21.
39. Albers GW, Marks MP, Kemp S, et al. Thrombectomy for stroke at 6 to 16 hours with selection by perfusion imaging. *New Engl J Med* 2018;378:708-718.
40. Burn J, Dennis M, Bamford J, Sandercock P, Wade D, Warlow C. Long-term risk of recurrent stroke after a first-ever stroke. The Oxfordshire Community Stroke Project. *Stroke* 1994;25:333-337.
41. Adams HP, Bendixen BH, Kappelle LJ, et al. Classification of subtype of acute ischemic stroke. Definitions for use in a multicenter clinical trial. TOAST. Trial of Org 10172 in Acute Stroke Treatment. *Stroke* 1993;24:35-41.
42. Radu RA, Terecoasă EO, Băjenaru OA, Tiu C. Etiologic classification of ischemic stroke: where do we stand? *Clin Neurol Neurosurg* 2017;159:93-106.
43. Nam HS, Kim HC, Kim YD, et al. Long-term mortality in patients with stroke of undetermined etiology. *Stroke* 2012;43:2948-2956.
44. Libby P. Current concepts of the pathogenesis of the acute coronary syndromes. *Circulation* 2001;104:365-372.
45. Ogata J, Yutani C, Otsubo R, et al. Heart and vessel pathology underlying brain infarction in 142 stroke patients. *Ann Neurol* 2008;63:770-781.

46. Bos D, van der Rijk MJ, Geeraedts TE, et al. Intracranial carotid artery atherosclerosis: prevalence and risk factors in the general population. *Stroke* 2012;43:1878-1884.
47. Sobiczewski W, Wirtwein M, Trybala E, Gruchala M. Severity of coronary atherosclerosis and stroke incidence in 7-year follow-up. *J Neurol* 2013;260:1855-1858.
48. Molteni M, Polo Friz H, Primitz L, Marano G, Boracchi P, Cimminiello C. The definition of valvular and non-valvular atrial fibrillation: results of a physicians' survey. *Europace* 2014;16:1720-1725.
49. Blackshear JL, Odell JA. Appendage obliteration to reduce stroke in cardiac surgical patients with atrial fibrillation. *Ann Thorac Surg* 1996;61:755-759.
50. Corrado G, Tadeo G, Beretta S, et al. Atrial thrombi resolution after prolonged anticoagulation in patients with atrial fibrillation: a transesophageal echocardiographic study. *Chest* 1999;115:140-143.
51. Hannon N, Sheehan O, Kelly L, et al. Stroke associated with atrial fibrillation – incidence and early outcomes in the North Dublin population stroke study. *Cerebrovasc Dis* 2009;29:43-49.
52. Lammie GA. Pathology of small vessel stroke. *Br Med Bull* 2000;56:296-306.
53. Jackson C, Sudlow C. Are lacunar strokes really different? A systematic review of differences in risk factor profiles between lacunar and nonlacunar infarcts. *Stroke* 2005;36:891-901.
54. De Jong G, Van Raak L, Kessels F, Lodder J. Stroke subtype and mortality: a follow-up study in 998 patients with a first cerebral infarct. *J Clin Epidemiol* 2003;56:262-268.
55. Wein T, Lindsay MP, Côté R, et al. Canadian stroke best practice recommendations: secondary prevention of stroke, practice guidelines, update 2017. *Int J Stroke* 2018;13:420-443.
56. Evans A, Perez I, Yu G, Kalra L. Should stroke subtype influence anticoagulation decisions to prevent recurrence in stroke patients with atrial fibrillation? *Stroke* 2001;32:2828-2832.
57. Hart RG, Pearce LA, Aguilar MI. Meta-analysis: antithrombotic therapy to prevent stroke in patients who have nonvalvular atrial fibrillation. *Ann Intern Med* 2007;146:857-867.

58. Ziegler PD, Koehler JL, Mehra R. Comparison of continuous versus intermittent monitoring of atrial arrhythmias. *Heart Rhythm* 2006;3:1445-1452.
59. Landau WM, Nassief A. Editorial comment—time to burn the TOAST. *Stroke* 2005;36:902-904.
60. Chang Y-J, Ryu S-J, Lin S-K. Carotid artery stenosis in ischemic stroke patients with nonvalvular atrial fibrillation. *Cerebrovasc Dis* 2002;13:16-20.
61. Furie B, Furie BC. Mechanisms of thrombus formation. *New Engl J Med* 2008;359:938-949.
62. Swystun LL, Liaw PC. The role of leukocytes in thrombosis. *Blood* 2016;128:753-762.
63. Litvinov RI, Weisel JW. Role of red blood cells in haemostasis and thrombosis. *ISBT Science Series* 2017;12:176-183.
64. Staessens S, Denorme F, François O, et al. Structural analysis of ischemic stroke thrombi: histological indications for therapy resistance. *Haematologica* 2020;105:498-507.
65. Bajd F, Vidmar J, Fabjan A, et al. Impact of altered venous hemodynamic conditions on the formation of platelet layers in thromboemboli. *Thromb Res* 2012;129:158-163.
66. Marder VJ, Chute DJ, Starkman S, et al. Analysis of thrombi retrieved from cerebral arteries of patients with acute ischemic stroke. *Stroke* 2006;37:2086-2093.
67. Liebeskind DS, Sanossian N, Yong WH, et al. CT and MRI early vessel signs reflect clot composition in acute stroke. *Stroke* 2011;42:1237-1243.
68. Sato Y, Ishibashi-Ueda H, Iwakiri T, et al. Thrombus components in cardioembolic and atherothrombotic strokes. *Thromb Res* 2012;130:278-280.
69. Boeckh-Behrens T, Schubert M, Förschler A, et al. The impact of histological clot composition in embolic stroke. *Clin Neuroradiol* 2014;26:189-197.
70. Niesten JM, van der Schaaf IC, van Dam L, et al. Histopathologic composition of cerebral thrombi of acute stroke patients is correlated

with stroke subtype and thrombus attenuation. *PLoS One* 2014;9:e88882.

71. Sallustio F, Arnò N, Legge SD, et al. Histological features of intracranial thrombo-emboli predict response to endovascular therapy for acute ischemic stroke. *J Neurol Disord Stroke* 2015;3:1105.
72. Kim S, Yoon W, Kim T, Kim H, Heo T, Park M. Histologic analysis of retrieved clots in acute ischemic stroke: correlation with stroke etiology and gradient-echo MRI. *AJNR Am J Neuroradiol* 2015;36:1756-1762.
73. Simons N, Mitchell P, Dowling R, Gonzales M, Yan B. Thrombus composition in acute ischemic stroke: A histopathological study of thrombus extracted by endovascular retrieval. *J Neuroradiol* 2015;42:86-92.
74. Maekawa K, Shibata M, Nakajima H, et al. Erythrocyte-rich thrombus is associated with reduced number of maneuvers and procedure time in patients with acute ischemic stroke undergoing mechanical thrombectomy. *Cerebrovasc Dis Extra* 2018;8:39-49.
75. Fitzgerald S, Dai D, Wang S, et al. Platelet-rich emboli in cerebral large vessel occlusion are associated with a large artery atherosclerosis source. *Stroke* 2019;50:1907-1910.
76. Chueh J, Wakhloo A, Hendricks G, Silva C, Weaver J, Gounis M. Mechanical characterization of thromboemboli in acute ischemic stroke and laboratory embolus analogs. *AJNR Am J Neuroradiol* 2011;32:1237-1244.
77. Almekhlafi MA, Hu WY, Hill MD, Auer RN. Calcification and endothelialization of thrombi in acute stroke. *Ann Neurol* 2008;64:344-347.
78. Dobrocky T, Piechowiak E, Cianfoni A, et al. Thrombectomy of calcified emboli in stroke. Does histology of thrombi influence the effectiveness of thrombectomy? *J Neurointerv Surg* 2017;10:345-350.
79. McMeekin P, White P, James MA, Price CI, Flynn D, Ford GA. Estimating the number of UK stroke patients eligible for endovascular thrombectomy. *Eur Stroke J* 2017;2:319-326.
80. Duloquin G, Graber M, Garnier L, et al. Incidence of acute ischemic stroke with visible arterial occlusion: a population-based study (Dijon Stroke Registry). *Stroke* 2020;51:2122-2130.

81. Baek J-H, Kim BM, Heo JH, et al. Number of stent retriever passes associated with futile recanalization in acute stroke. *Stroke* 2018;49:2088-2095.
82. Gomori JM, Grossman RI. Mechanisms responsible for the MR appearance and evolution of intracranial hemorrhage. *Radiographics* 1988;8:427-440.
83. Kirchhof K, Welzel T, Mecke C, Zoubaa S, Sartor K. Differentiation of white, mixed, and red thrombi: value of CT in estimation of the prognosis of thrombolysis phantom study. *Radiology* 2003;228:126-130.
84. Rovira A, Orellana P, Alvarez-Sabin J, et al. Hyperacute ischemic stroke: middle cerebral artery susceptibility sign at echo-planar gradient-echo MR imaging. *Radiology* 2004;232:466-473.
85. Brinjikji W, Michalak G, Kadirvel R, et al. Utility of single-energy and dual-energy computed tomography in clot characterization: an in-vitro study. *Interv Neuroradiol* 2017;23:279-284.
86. Flacke S, Urbach H, Keller E, et al. Middle cerebral artery (MCA) susceptibility sign at susceptibility-based perfusion MR imaging: clinical importance and comparison with hyperdense MCA sign at CT 1. *Radiology* 2000;215:476-482.
87. Mair G, Boyd EV, Chappell FM, et al. Sensitivity and specificity of the hyperdense artery sign for arterial obstruction in acute ischemic stroke. *Stroke* 2015;46:102-107.
88. Shin JW, Jeong HS, Kwon H-J, Song KS, Kim J. High red blood cell composition in clots is associated with successful recanalization during intra-arterial thrombectomy. *PLoS One* 2018;13:e0197492.
89. Choi MH, Park GH, Lee JS, et al. Erythrocyte fraction within retrieved thrombi contributes to thrombolytic response in acute ischemic stroke. *Stroke* 2018;49:652-659.
90. Puig J, Pedraza S, Demchuk A, et al. Quantification of thrombus hounsfield units on noncontrast CT predicts stroke subtype and early recanalization after intravenous recombinant tissue plasminogen activator. *AJNR Am J Neuroradiol* 2012;33:90-96.
91. Yamamoto N, Satomi J, Tada Y, et al. Two-layered susceptibility vessel sign on 3-Tesla T2*-weighted imaging is a predictive biomarker of stroke subtype. *Stroke* 2015;46:269-271.

92. Horie N, Tateishi Y, Morikawa M, et al. Acute stroke with major intracranial vessel occlusion: characteristics of cardioembolism and atherosclerosis-related in situ stenosis/occlusion. *J Clin Neurosci* 2016;32:24-29.
93. Brinjikji W, Duffy S, Burrows A, et al. Correlation of imaging and histopathology of thrombi in acute ischemic stroke with etiology and outcome: a systematic review. *J Neurointerv Surg* 2017;9:529-534.
94. Bourcier R, Détraz L, Serfaty JM, et al. MRI interscanner agreement of the association between the susceptibility vessel sign and histologic composition of thrombi. *J Neuroimaging* 2017;27:577-582.
95. Yu H, Shimakawa A, McKenzie CA, Brodsky E, Brittain JH, Reeder SB. Multiecho water - fat separation and simultaneous R2* estimation with multifrequency fat spectrum modeling. *Magn Reson Med* 2008;60:1122-1134.
96. Hernando D, Kellman P, Haldar J, Liang ZP. Robust water/fat separation in the presence of large field inhomogeneities using a graph cut algorithm. *Magn Reson Med* 2010;63:79-90.
97. Liu J, Drangova M. Method for B0 off-resonance mapping by non-iterative correction of phase-errors (B0-NICE). *Magn Reson Med* 2015;74:1177-1188.
98. Jain V, Abdulmalik O, Propert KJ, Wehrli FW. Investigating the magnetic susceptibility properties of fresh human blood for noninvasive oxygen saturation quantification. *Magn Reson Med* 2012;68:863-867.
99. de Rochefort L, Liu T, Kressler B, et al. Quantitative susceptibility map reconstruction from MR phase data using bayesian regularization: validation and application to brain imaging. *Magn Reson Med* 2010;63:194-206.
100. Sun H, Kate M, Gioia LC, Emery DJ, Butcher K, Wilman AH. Quantitative susceptibility mapping using a superposed dipole inversion method: application to intracranial hemorrhage. *Magn Reson Med* 2016;76:781-791.
101. Liu J, Liu T, de Rochefort L, et al. Morphology enabled dipole inversion for quantitative susceptibility mapping using structural consistency between the magnitude image and the susceptibility map. *NeuroImage* 2012;59:2560-2568.

102. Bourcier R, Pautre R, Mirza M, et al. MRI quantitative T2* mapping to predict dominant composition of in vitro thrombus. *AJNR Am J Neuroradiol* 2019;40:59-64.
103. Chang S, Zhang J, Liu T, et al. Quantitative susceptibility mapping of intracerebral hemorrhages at various stages: mapping of intracerebral hemorrhages. *J Magn Reson Imaging* 2016;44:420-425.
104. Shinohara Y, Kato A, Yamashita E, Ogawa T. R2* map by IDEAL IQ for acute cerebral infarction: compared with susceptibility vessel sign on T2*-weighted imaging. *Yonago Acta Med* 2016;59:204.
105. Di Meglio L, Desilles J-P, Ollivier V, et al. Acute ischemic stroke thrombi have an outer shell that impairs fibrinolysis. *Neurology* 2019;93:e1686-e1698.
106. Fernández-Delgado M, Cernadas E, Barro S, Amorim D. Do we need hundreds of classifiers to solve real world classification problems? *J Mach Learn Res* 2014;15:3133-3181.
107. Breiman L. Random forests. *Mach Learn* 2001;45:5-32.
108. Gillies RJ, Kinahan PE, Hricak H. Radiomics: images are more than pictures, they are data. *Radiology* 2016;278:563-577.
109. Haralick RM, Shanmugam K, Dinstein IH. Textural features for image classification. *IEEE Trans Syst Man Cybern* 1973:610-621.
110. Brynolfsson P, Nilsson D, Torheim T, et al. Haralick texture features from apparent diffusion coefficient (ADC) MRI images depend on imaging and pre-processing parameters. *Sci Rep* 2017;7:1-11.
111. Aerts HJWL, Velazquez ER, Leijenaar RTH, et al. Decoding tumour phenotype by noninvasive imaging using a quantitative radiomics approach. *Nat Commun* 2014;5:1-9.
112. Zhou H, Vallières M, Bai HX, et al. MRI features predict survival and molecular markers in diffuse lower-grade gliomas. *Neuro Oncol* 2017;19:862-870.
113. Vallières M, Freeman CR, Skamene SR, El Naqa I. A radiomics model from joint FDG-PET and MRI texture features for the prediction of lung metastases in soft-tissue sarcomas of the extremities. *Phys Med Biol* 2015;60:5471-5496.

114. Kim HS, Kim YJ, Kim KG, Park JS. Preoperative CT texture features predict prognosis after curative resection in pancreatic cancer. *Sci Rep* 2019;9:1-9.
115. Rajini NH, Bhavani R. Computer aided detection of ischemic stroke using segmentation and texture features. *Measurement* 2013;46:1865-1874.
116. Betrouni N, Yasmina M, Bombois S, et al. Texture features of magnetic resonance images: an early marker of post-stroke cognitive impairment. *Transl Stroke Res* 2020;11:643-652.
117. Gonzalez AV, Buerke B, Görlich D, et al. Clot analog attenuation in non-contrast CT predicts histology: an experimental study using machine learning. *Transl Stroke Res* 2020;11:940-949.
118. Bretzner M, Lopes R, McCarthy R, et al. Texture parameters of R2* maps are correlated with iron concentration and red blood cells count in clot analogs: a 7-T micro-MRI study. *J Neuroradiol* 2019;47:306-311.
119. Qiu W, Kuang H, Nair J, et al. Radiomics-based intracranial thrombus features on CT and CTA predict recanalization with intravenous alteplase in patients with acute ischemic stroke. *AJNR Am J Neuroradiol* 2019;40:39-44.
120. Hofmeister J, Bernava G, Rosi A, et al. Clot-based radiomics predict a mechanical thrombectomy strategy for successful recanalization in acute ischemic stroke. *Stroke* 2020;51:2488-2494.
121. Rosenblatt F. The perceptron: a probabilistic model for information storage and organization in the brain. *Psychol Rev* 1958;65:386.
122. LeCun Y, Bottou L, Bengio Y, Haffner P. Gradient-based learning applied to document recognition. *Proc IEEE*. Volume 86; 1998. p. 2278-2324.
123. Zhang C, Platt JC, Viola PA. Multiple instance boosting for object detection. *Adv Neural Inf Process Syst*; 2006. p. 1417-1424.
124. Krizhevsky A, Sutskever I, Hinton GE. Imagenet classification with deep convolutional neural networks. *Adv Neural Inf Process Syst*; 2012. p. 1097-1105.
125. Charron O, Lallement A, Jarnet D, Noblet V, Clavier J-B, Meyer P. Automatic detection and segmentation of brain metastases on

- multimodal MR images with a deep convolutional neural network. *Comput Biol Med* 2018;95:43-54.
126. Alzubaidi L, Fadhel MA, Oleiwi SR, Al-Shamma O, Zhang J. DFU_QUTNet: diabetic foot ulcer classification using novel deep convolutional neural network. *Multimed Tools Appl* 2020;79:15655-15677.
 127. Liu L, Chen S, Zhang F, Wu F-X, Pan Y, Wang J. Deep convolutional neural network for automatically segmenting acute ischemic stroke lesion in multi-modality MRI. *Neural Comput Appl* 2019:1-14.
 128. Wang K, Shou Q, Ma SJ, et al. Deep learning detection of penumbral tissue on arterial spin labeling in stroke. *Stroke* 2020;51:489-497.
 129. Choi Y, Kwon Y, Lee H, Kim BJ, Paik MC, Won J-H. Ensemble of deep convolutional neural networks for prognosis of ischemic stroke. *International Workshop on Brainlesion: Glioma, Multiple Sclerosis, Stroke and Traumatic Brain Injuries: Springer; 2016. p. 231-243.*
 130. Nielsen A, Hansen MB, Tietze A, Mouridsen K. Prediction of tissue outcome and assessment of treatment effect in acute ischemic stroke using deep learning. *Stroke* 2018;49:1394-1401.
 131. Ho KC, Speier W, El-Saden S, Arnold CW. Classifying acute ischemic stroke onset time using deep imaging features. *AMIA Annual Symposium Proceedings: American Medical Informatics Association; 2017. p. 892.*

CHAPTER 2

Simultaneous R_2^* and QSM measurement enables differentiation of thrombus hematocrit and age: an *in vitro* study at 3T

2.1 Introduction

Recanalization has been established as the definitive treatment for acute ischemic stroke,¹ however the efficacy of common fibrinolytic and endovascular thrombectomy therapies is influenced by underlying thrombus composition.^{2,3} Stroke thrombi consist principally of red blood cells, fibrin and platelets, though relative proportions vary widely.⁴ In certain cases, calcium or cholesterol crystals may be incorporated within, or even form the majority of, an embolic thrombus;^{5,6} calcium interferes with fibrinolytic therapy,⁷ and both calcium and cholesterol affect thrombus mechanical properties.⁶ Thrombus age may also affect lysis rate and indicate underlying etiology.^{8,9} Magnetic resonance imaging (MRI) has demonstrated utility in the detection and staging of ischemic stroke,¹⁰ but an evolving understanding of the implications of thrombus composition motivates the development of imaging-based thrombus characterization methods, which offer to non-invasively aid decision-making in acute stroke treatment and support determination of the embolic source.

Imaging-based characterization of thrombi *in vivo* has largely been achieved through qualitative metrics such as the appearance of a susceptibility-based

blooming artifact on MRI or a hyperdense sign on computed tomography (CT).^{11,12} Though shown to be correlated to red blood cell proportion, such signs have proven inconsistent when applied towards association with underlying thrombus etiology,¹³ may be mimicked by the appearance of calcium¹⁴ and are insensitive to lipidic components. Quantitative MRI characterization methods utilizing diffusion or relaxation parameters have been successfully applied in preclinical models, but require lengthy scan times that are prohibitive in the clinic.^{15,16} Relaxation and quantitative susceptibility mapping (QSM) parameters have been measured for experimental blood clots *in vitro*,^{17,18} but did not include calcified or lipidic components and either compared multiple clots of different composition at one time or measured changes in a single clot over time. Because clinical thrombi vary in both composition and age, and each affects MR characteristics, both aspects must be considered if knowledge gained from *in vitro* characterization is to be extended to clinical application.

Three-dimensional (3D) multi-echo gradient echo (GRE) acquisitions offer an opportunity to derive multiple quantitative imaging parameters in the form of quantitative maps from a single scan. The acquisition of multiple early echoes at various fat-water phase shifts allows for simultaneous proton-density fat fraction (FF), R_2^* and B_0 mapping through Dixon MRI post-processing,¹⁹ while the acquisition of multiple echoes at late echo times is required for sufficient susceptibility weighting to perform QSM mapping.²⁰ Recently, a novel multi-echo GRE acquisition and analysis approach has combined an early, short-echo-spacing echo train (to enable Dixon MRI) with a large-echo-spacing echo train (to capture susceptibility variation and additional R_2^* information).²¹ Together, the post-processing algorithms and dual-echo-train GRE acquisition have the potential to provide multiple quantitative imaging parameters (FF, R_2^* , B_0 , QSM) suitable for characterization of thrombus from a single 3D scan. In this study, we

examine the ability of R_2^* , QSM and FF values to characterize blood clot of varying hematocrit formed *in vitro*, some containing calcified and lipidic components, across an age range relevant to thrombi causing stroke. Specifically, we quantified R_2^* and QSM values of *in vitro* clot throughout ageing up to 6 days, examined the ability of the derived values to discriminate between various clot hematocrit and age, and finally assessed the ability to predict clot hematocrit and age from measured R_2^* and QSM values. Additionally, we compared the ability of standard clinical MRI thrombus assessment techniques (*i.e.* late-echo GRE magnitude) to R_2^* , QSM and FF maps for detecting calcified and lipidic components within clots of various hematocrit and age.

2.2 Materials and methods

2.2.1 Phantom preparation

Thrombus phantoms were constructed using arterial porcine blood collected from a local abattoir and anti-coagulated with 0.109 M buffered sodium citrate (Medicago AB; Danmark, Sweden) in a 1:9 ratio. The anti-coagulated blood was centrifuged at 300 *g* for 10 minutes, the supernatant plasma was extracted and spun again at 300 *g* for 10 minutes to derive platelet-rich and platelet-poor plasma (PRP and PPP, respectively). Separate whole blood samples were spun at 775 *g* for 15 minutes to isolate red blood cells (RBCs). Blood samples of controlled hematocrit (10, 20, 30, 50, 40 and 60%) were prepared by mixing RBCs and PRP; two 5 mL samples of each hematocrit were placed inside 1 cm diameter polystyrene vials (chosen to have a minimal effect on QSM, <0.005 ppm shifts observed in water samples). Antibiotic (100X stock, Gibco Antibiotic-Antimycotic; Thermo Fisher Scientific; Waltham, MA) and 500 mmol/L calcium chloride (Caledon Laboratory

Chemicals; Georgetown, Canada) solutions were added to each sample achieving final dilutions of 1/100 and 1/45, respectively. Finally, clotting was induced by thromboplastin (Thermo Fisher Scientific; Waltham, MA) at a 1/3000 final dilution. To mitigate clot retraction, clots were left undisturbed in the vials throughout the experiment. The time at which thromboplastin was added was considered to be the time of clot formation ($t = 0$). All clot vials were placed vertically into a preformed agar-filled container (3.5% agar, 8% glycerol, 2% formalin solution (neutral buffered, 10%)); samples were arranged concentrically within the phantom, and a vial containing peanut oil was placed in its centre to act as a control sample during FF mapping. The phantom was kept in a 37 °C water bath between scans to replicate biological conditions for clot ageing and will be referred to as the 'blood-only' thrombus phantom.

To emulate clinical thrombi containing lipid, a separate thrombus phantom was prepared using identical methodology (hematocrit of 0, 20, 40 and 60%) but a piece of lard (~2.5 mm cube; local abattoir) was added to each of the blood samples (2 mL) immediately following the injection of thromboplastin. In this case the samples were left to coagulate at room temperature for one hour following thromboplastin injection, at which point 3 mL of PPP was added to fill the remaining air space above the formed multi-component clots within each vial. A sample containing a whole-blood clot (approximately 30% hematocrit) with an added piece of agar containing 5M calcium carbonate to simulate the presence of calcified tissue¹⁴ was also prepared.

2.2.2 Image acquisition

All imaging experiments were performed on a 3.0 T whole-body MRI scanner (GE 750, GE Medical Systems, Milwaukee, WI) using a 32-channel receive head coil. B_0 and B_1 shimming were performed prior to each imaging session. Scans were acquired using a 3D multi-echo bipolar GRE sequence designed

for clinical imaging *in vivo*; the sequence includes two 5-echo trains: the first train was optimized for chemical shift imaging (first echo time (TE) = 3.20 ms, echo spacing = 1.46 ms); the second train was optimized to highlight susceptibility-related contrast at the level commonly observed within human brain *in vivo* (first TE = 16.75 ms, echo spacing = 7.15 ms). The remaining scan parameters were repetition time = 47.6 ms, bandwidth = 142.86 kHz, flip angle = 10°; field of view = 18 cm; matrix size = 192 × 192 × 42, for a final voxel dimension of 0.94 × 0.94 × 1.0 mm³. Bipolar readout enabled the in-and-out of phase fat/water acquisition during the first echo train. No acceleration or averaging was used; the total acquisition time was 6 minutes 28 seconds.

All phantoms were scanned in the coronal plane, with the vials aligned perpendicular to B₀; clots were thus kept vertical throughout the experiment, limiting retraction and the introduction of air bubbles. The blood-only thrombus phantom was initially scanned every 15 minutes without repositioning from 30 minutes to 6 hours to investigate the MRI properties of acute thrombi; scans were then acquired at 22 and 26 hours and 2, 3 and 6 days post clotting to represent chronic thrombus. The thrombus phantom containing lard was scanned at 3, 7 and 18 hours, then daily for one week; the calcium-containing clot was scanned at 2 hours and at 2 days post clotting.

2.2.3 Image reconstruction and multi-parameter mapping

Image reconstruction and multi-parameter map generation were performed in Matlab (Matlab 8 R2015a; Mathworks, Natick, MA). Raw image data were reconstructed off-line using the Orchestra Software Development Kit (GE Healthcare; Milwaukee, WI). Complex channel combination was performed using singular value decomposition and phase errors resulting from the bipolar acquisition were removed.²¹ Fat fraction, B₀ and R₂^{*} maps were generated using the B0-NICE algorithm.¹⁹ Briefly, the B0-NICE algorithm

utilizes magnitude data processed independently to generate FF and R_2^* estimate maps, unwrapped phase data to generate initial phase-based B_0 and FF maps, and then uses the derived magnitude-based FF map to correct for phase errors existing in phase-based B_0 and FF maps to generate the final B_0 and FF maps. The algorithm was used with the first 5 acquired echoes to produce FF and B_0 maps, and all 10 echoes for the generation of R_2^* maps. QSM maps were generated using the MEDI QSM algorithm²⁰ implemented on all 10 echoes of the channel-combined complex data, with the λ regularization parameter set to 1000 and maximum iterations set to 10. The Laplacian boundary value method was used for background field removal, with tolerance, depth and peel set to 0.005, -1 and 0, respectively.

The performance of the reconstruction and mapping algorithms described above was evaluated using a calibration phantom with known FF, QSM and R_2^* . Details pertaining to calibration phantom fabrication, analysis, and associated results are presented in *Supplementary Material*.

2.2.4 Image analysis

Segmentation of the blood-only clots and blood-only regions of clots containing lard or calcium was completed by using cylindrical regions of interest (ROIs) (~7-mm diameter and ~10-mm tall) to derive sample mean and standard deviation values for all measured parameters; care was taken to position ROIs to contain only clotted blood and exclude added lard or calcium when present, as well as slices showing clot retraction. The calcium and lard were segmented via thresholding applied within the clot on QSM and FF maps, respectively; the threshold for FF was 0.5 and that for QSM maps was -0.1 ppm. Image analysis was performed using Matlab.

2.2.5 Data analysis

The ability of simultaneously measured R_2^* and QSM values to estimate the age and hematocrit of the clots was evaluated. Clots aged ≤ 6 hours were considered acute and those aged >6 hours were considered chronic. Receiver operator characteristic (ROC) analysis was performed to derive the R_2^* and QSM thresholds that optimally differentiate acute from chronic clots. To estimate hematocrit in acute clots, linear regression was applied to determine the relationship between hematocrit and QSM values, while for chronic clots hematocrit was fitted as a decaying exponential function of the R_2^*/QSM ratio; all fitting was performed using data from six of the twelve clots (one from each pair, of each hematocrit). The remaining six clots were used to evaluate the performance of the derived relationships to predict hematocrit in both acute and chronic states. All data analysis was performed using GraphPad Prism (v7.0; GraphPad Software, La Jolla, CA).

2.3 Results

2.3.1 Acute clot (≤ 6 hours)

Figure 2-1 illustrates representative R_2^* and QSM maps and values derived from the blood-only thrombus phantom in the acute phase (*i.e.* first 6 hours post clotting). R_2^* increased with hematocrit but was nearly identical for the 40-60% hematocrit clots (Figure 2-1C). A small, consistent increase in R_2^* was observed over time, with the slope increasing markedly between the 10% and 20% clots ($0.04 \text{ s}^{-1}\text{hr}^{-1}$ and $0.31 \text{ s}^{-1}\text{hr}^{-1}$, respectively); the slope plateaued at approximately $0.5 \text{ s}^{-1}\text{hr}^{-1}$ for the 40-60% hematocrit clots. Over the six-hour period clot QSM values remained constant (Figure 2-1D) and were linearly proportional to hematocrit. The consistency of R_2^* and QS values between

clots of the same composition at the six-hour time point is shown in Figures 2-1E and F; similar consistency was observed at all acute time points, as expected.

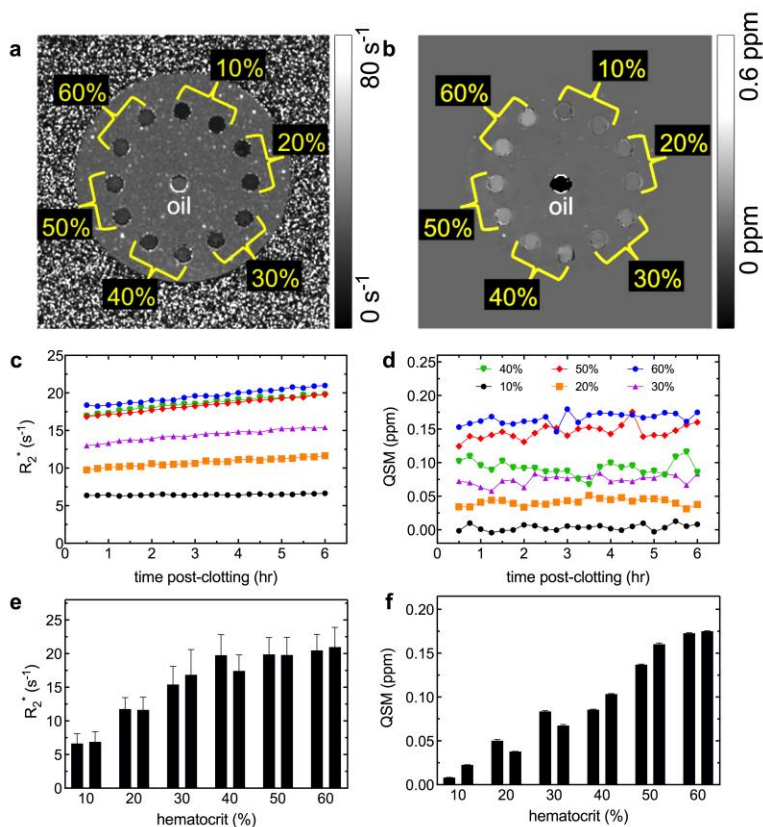


Figure 2-1: Acute blood clot relaxation and magnetic susceptibility quantification; shown are the central coronal slices of the (A) R_2^* [0 s⁻¹, 80 s⁻¹] and (B) QSM [-0.5 ppm, 0.5 ppm] maps for the blood-only thrombus phantom at 6 hours post clotting. The mean (C) R_2^* and (D) QSM values of an individual clot from each pair (10 to 60% hematocrit) are shown over the first 6 hours post clotting; error bars were omitted for clarity. The mean and standard deviation of each clot pair with the same nominal hematocrit at the six hour time point are shown for (E) R_2^* and (F) QSM, demonstrating reproducibility.

2.3.2 Chronic clot (>6 hours)

The effects of chronic ageing (up to six days) on mean R_2^* and QSM values are shown in Figure 2-2. R_2^* increased rapidly over the first 40 hours (up to 4.0 s⁻¹

$^1\text{hr}^{-1}$ for 40-60% hematocrit), before reaching a plateau after the 44 hour scan (Figure 2-2A). High hematocrit clots (over 40%) were indistinguishable from each other on the basis of R_2^* . Measured QSM increased in proportion to clot hematocrit over the first 44 hours and remained constant for the remainder of the experiment (Figure 2-2B). Unlike R_2^* , QSM was linearly related to clot hematocrit at all time points. Because both R_2^* and QSM changed over time, neither could be used alone to infer hematocrit in a thrombus of unknown age. A plot of R_2^* against QSM (Figure 2-2C), demonstrates a linear relationship with a unique slope at all hematocrits – decreasing from 325 to 173 $\text{s}^{-1}\text{ppm}^{-1}$ as hematocrit increased from 10 to 60%, suggesting that hematocrit may be estimated from the R_2^*/QSM ratio.

2.3.3 Acute and chronic clot differentiation

The receiver-operating-characteristic analysis used to derive R_2^* and QSM thresholds that differentiate between acute and chronic clots yielded a QSM threshold of 0.165 ppm with a corresponding sensitivity and specificity of 85 and 92%, respectively; the area under the curve (AUC) was 0.932 (95% CI 0.892 to 0.972; $p < 0.0001$). All acute clots had mean R_2^* below 22 s^{-1} , while chronic clots had an R_2^* greater than 24 s^{-1} (*i.e.* 100% sensitivity and specificity; AUC = 1).

2.3.4 Clot hematocrit prediction

The ability to use measured R_2^* and QSM to predict clot hematocrit at any age is demonstrated in Figure 2-3. For acute clots, Figure 2-3A shows that hematocrit can be estimated from QSM ($\text{HCT} = 260 * \text{QSM} + 9\%$; where HCT is the hematocrit percentage; $R^2 = 0.97$). For chronic clots, Figure 2-3B shows that hematocrit can be estimated from the R_2^*/QSM ratio ($\text{HCT} = 125.3 * \exp(-0.007 * R_2^*/\text{QSM}) + 4.2\%$; $R^2 = 0.77$). Evaluation of the ability to predict clot hematocrit, calculated for the remaining six clots in the phantom, yielded a

mean absolute error of $4.9 \pm 3.1\%$ for the acute clots and $8.3 \pm 5.4\%$ for the chronic clots.

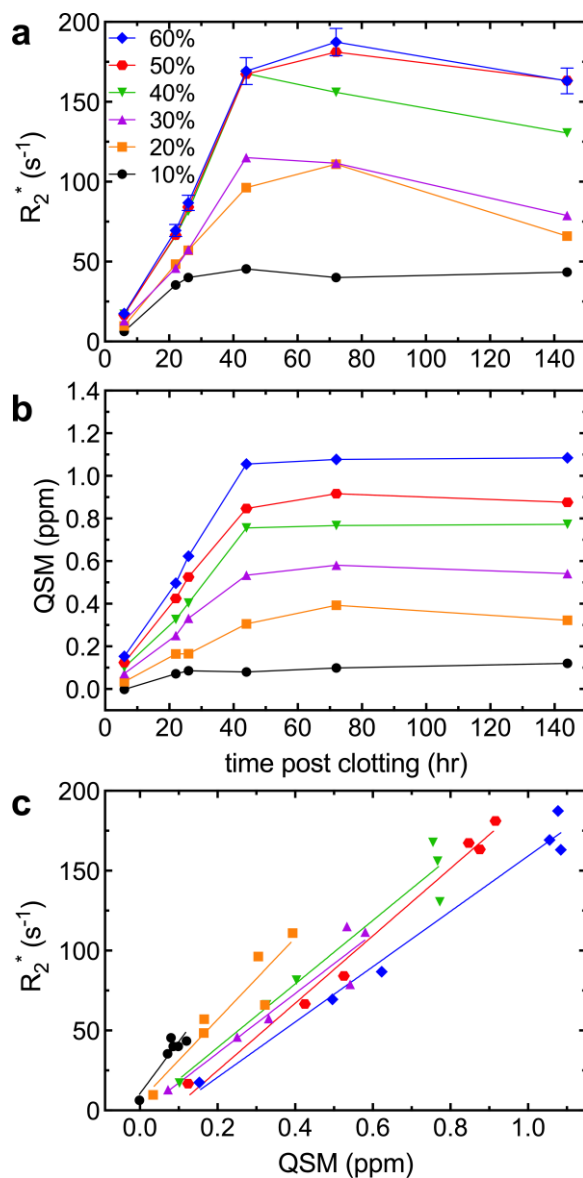


Figure 2-2: Blood clot R_2^* and QSM of chronic clots throughout ageing; (A) R_2^* and (B) QSM values of blood-only clots from 6 up to 144 hours post clotting (the 6-hr time point is included in order to relate these results to those of the acute clots of Figure 2-1). Plotted are mean values of individual clots; standard deviation error bars of only the 60% hematocrit clots are shown for clarity, error bars for QSM were smaller than the symbols. (C) Scatter plot and linear regression of R_2^* versus QSM values at all time points for clots of each hematocrit.

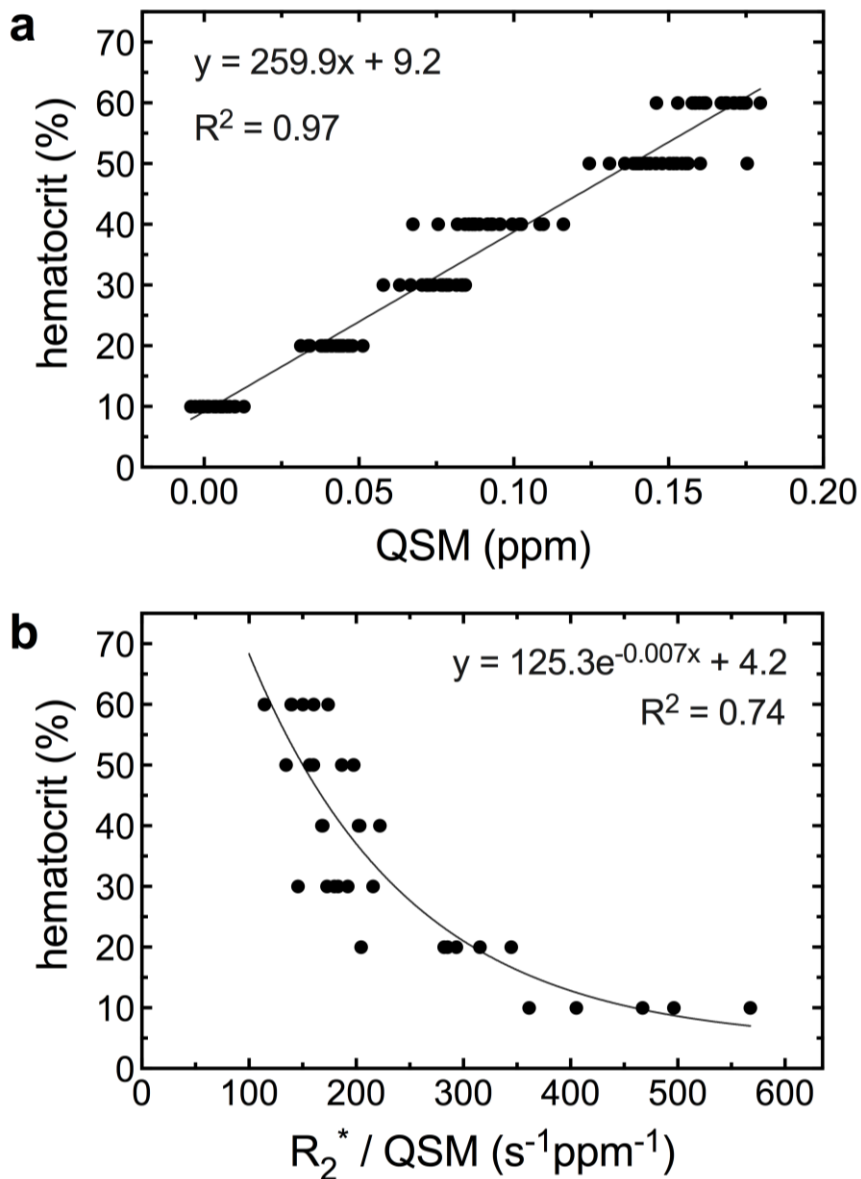


Figure 2-3: Relationship between hematocrit and measured quantitative imaging values in acute (≤ 6 hours) and chronic (> 6 hours) clot. (A) Acute clot hematocrit can be estimated linearly from measured QSM values, while (B) chronic clot hematocrit can be estimated from an exponential relation of the ratio of R_2^* / QSM . Shown are data points from the same 6 clots (one from each pair of 10 to 60% hematocrit) plotted in Figures 2-1 and 2-2.

2.3.5 Identification of lipid and calcifications within clot

Representative images from the lard clot phantom are displayed in Figure 2-4. Results from two time points are shown – the 7-hour time point representing acute (Figures 2-4A, C) and the 4-day time point representing chronic clot (Figures 2-4B, D). The magnitude images (Figures 2-4A, B) are representative of GRE acquisitions commonly used for thrombus characterization. As expected, the TE=4.2 ms magnitude images show no ability to differentiate hematocrit, while the TE=31 ms magnitude images demonstrate a decrease in signal intensity with increasing hematocrit in the chronic clot (Figure 2-4B). However, this signal loss eliminates contrast between the clot and lard. The quantitative R_2^* , QSM and FF maps (Figures 2-4C, D) demonstrate that differentiation between clot and lipid components is possible independent of the clot age or hematocrit; the lard is clearly distinguishable based on its high FF (mean: 0.78 ± 0.02). Similar results are observed in the clot containing agar with 5M calcium carbonate (Figure 2-5), where the calcium is readily distinguishable from clot due to its diamagnetic QSM value (mean: -0.34 ± 0.08 ppm) at both two hours and two days post clotting (Figures 2-5A, B).

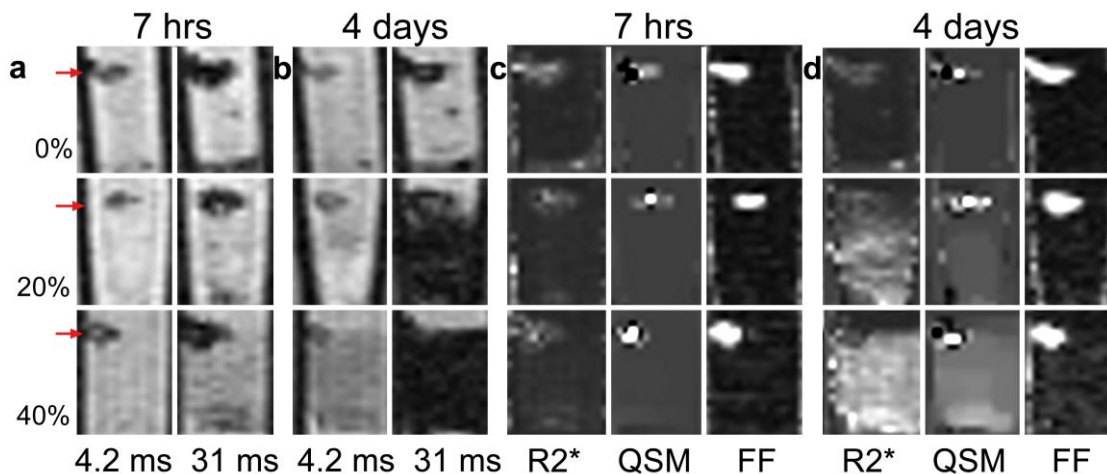


Figure 2-4: Regions (1.2×1.4 mm) from representative sagittal slices through select clots (0, 20, 40% hematocrit) in the lard clot phantom demonstrating discriminability of the added component; shown are early and late echo magnitude images of clots within the phantom at (A) 7 hours and (B) 4 days post clotting. These images represent the current standard technique for thrombus characterization; lard is either visible within clot as a nondescript area of low signal (red arrows) or is undetectable because of signal void produced by chronic clot (B; 20 and 40% clots at 31 ms). R_2^* , QSM and fat fraction (FF) maps of the phantom are shown at (C) 7 hours and (D) 4 days post clotting. Lipid is readily distinguishable from clot by its elevated FF value in clots of all hematocrits whether acute or chronic. Noticeable differences in R_2^* and QSM values between clots of different hematocrit can also be observed in the chronic clots in (D).

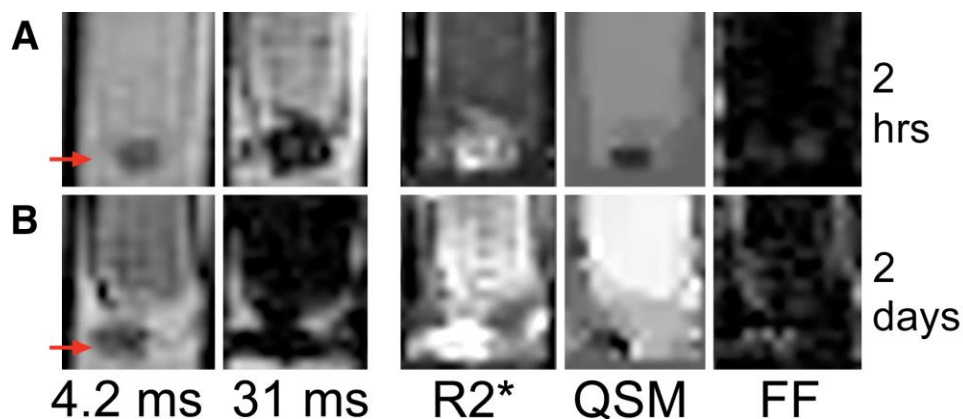


Figure 2-5: Regions (1.2×1.4 mm) from representative sagittal slices through a single whole-blood clot with an added piece of agar containing 5M calcium carbonate (red arrows); shown are early and late echo magnitude images at (A) 2 hours and (B) 2 days post clotting. Similar to the appearance of the lard

added to clot, calcium carbonate shows low signal on early and late magnitude images, but differs with high R_2^* , low QSM and low FF values. The calcium carbonate is definitively identified within both acute and chronic clot by its negative QSM values (black in the QSM maps of (B)).

2.4 Discussion

This study demonstrates the use of R_2^* , QSM and FF maps to characterize and differentiate blood clot based on hematocrit and age, as well as to identify calcified and lipidic components when present. Such quantitative information provides a non-invasive tool to characterize thrombus composition, and to potentially inform decisions in the management and treatment of acute ischemic stroke. The hematocrit of acute clot (≤ 6 hours) could be determined directly from QSM, but as the clots aged beyond the 6-hour time point, knowledge of the relationship between R_2^* and QSM was required to estimate hematocrit. Calcified and lipidic components were easily identifiable in clot of any hematocrit and age through QSM and FF mapping, respectively.

A blood-only thrombus phantom was scanned serially every 15 minutes over the initial 6 hours post clot formation, and then intermittently thereafter for up to 6 days. The 6-hour timeframe for more rigorous examination was chosen because it is the commonly accepted treatment window for thrombolytic and endovascular therapies for acute ischemic stroke;²² clots examined over this period therefore give insight into the parameter values expected in spontaneously formed, immediately occluding thrombi, as well as how these values may evolve over the treatment window. R_2^* and QSM values showed clear differences between the acute clots of different hematocrit, indicating that even newly formed (and thus well-oxygenated) clots may be differentiated by quantitative measurements of relaxation and

susceptibility. In terms of the change in values over the 6-hour time period, only a small increasing trend was observed in R_2^* while no trend was observed in QSM values, implying little change in hemoglobin oxygenation status. This is significant because it suggests that 6 hours may not be enough time for thrombi to deoxygenate under ischemic conditions *in vivo*, and therefore that thrombi that are deoxygenated upon clinical presentation (indicated by the presence of a blooming artifact) have become so only after considerable ageing at the site of thrombus formation, prior to embolization.

Observation of these same clots over the next 6 days of ageing, in contrast, demonstrated considerable changes over the course of the experiment. Both R_2^* and QSM values of clots increased in proportion to hematocrit over time, reaching a plateau after 44 hours. Increasing R_2^* and QSM values within the first few days of *in vitro* clot formation have been observed previously.^{17,18} RBC homeostasis is maintained through the metabolism of glucose;²³ the limited supply of naturally present glucose *in vitro* inevitably results in the oxidative denaturation of oxyhemoglobin to paramagnetic deoxy- and methemoglobin forms,²⁴ increasing QSM values, and consequently heightening local field inhomogeneity and thereby increasing R_2^* . The delay from clotting to when the rapid increase in R_2^* and QSM values was observed is likely linked to the time taken for RBCs to exhaust the local glucose supply. Because the clot R_2^* increase is driven primarily by a change in magnetic susceptibility inhomogeneity, we would additionally expect the clots with a similar heterogeneity of components (hematocrit between 40 to 60% in this study) to demonstrate similar R_2^* values. Indeed, R_2^* values of the 40, 50 and 60% clots were comparable throughout the experiment, matching previous measurements of deoxygenated blood.²⁵ The observed decrease in R_2^* observed at the 140 hour time point is likely due to a drop in R_2 that occurs in excessively aged blood following lysis of the RBC membrane.²⁵

The quantitative imaging values derived in this *in vitro* study strongly suggest that simultaneous measurement of R_2^* and QSM could be used to infer hematocrit and age in clinical thrombi. Our results suggest that a thrombus presenting with R_2^* and QSM values below 22 s^{-1} and 0.165 ppm, respectively, can be considered to be acutely formed, and for these thrombi hematocrit can be inferred directly from QSM. When R_2^* or QSM values are above these thresholds, the thrombus can be assumed to be chronic and R_2^* or QSM values alone will not be able to discriminate between a moderately aged thrombus of high hematocrit and one of advanced aged with low hematocrit. This study suggests that once a thrombus is identified as chronic, the R_2^*/QSM ratio can be used to estimate hematocrit regardless of age. We tested a number of parametric fitting methods to derive an equation relating imaging values to hematocrit, including fitting to exponential and power functions, as well as multiple linear regression; exponential fitting was chosen because it provided the best performance, however no underlying model was considered to justify this choice and it may not represent the best possible method. Our hematocrit prediction accuracy of better than 10% suggests that even clots of hematocrit between 40-60%, which showed similar R_2^* , varied enough in their QS values to be differentiable by the R_2^*/QSM ratio.

Of course, the derived values and relationships in this study of *in vitro* clots may not be directly applicable to the clinic and must be validated in excised human thrombi. Validation of the R_2^* and QSM thresholds for differentiating between acute and chronic thrombus also needs to be performed *in vivo*, however this is difficult to achieve as thrombus age is rarely known. It must be further stressed that the age threshold of 6 hours defined here to differentiate acute and chronic clot is unlikely to directly correspond to the time period in which similar changes occur within thrombus imaging values *in vivo*, as the rate of thrombus degradation is likely to differ and vary

between subjects. Nonetheless, the evidence provided here strongly suggests that R_2^* and QSM, measured simultaneously, are able to act as imaging biomarkers that can identify thrombus age and hematocrit.

Additional clot phantoms were constructed to investigate the ability of the quantitative maps to distinguish calcified and lipidic components within clots of varied hematocrit and age, and to compare that to the ability of current thrombus characterization methods. For acute clot, GRE magnitude images have the ability to detect the calcified or lipidic components, but both give an identical, low signal appearance; the GRE images are also unable to discriminate between clots of different hematocrit. In contrast, lard shows elevated FF compared to all clots and to calcium, while calcium shows unique negative QSM values. In chronic clots, late-echo-magnitude images can roughly tell apart clots of low vs. high hematocrit by the extent and degree of signal loss, but this signal loss removes contrast between the clot and additional components, eliminating the possibility of their detection. Applied together, the quantitative R_2^* , QSM and FF maps distinguish between clots of different hematocrit, as expected, while also providing the ability to identify calcium and lipid components from the QSM and FF maps, respectively.

Unavoidable imperfections of an *in vitro* clot phantom for representing thrombi should be considered as limitations for transferring our findings to future *in vivo* studies. Clots were formed statically through the addition of thromboplastin, which has been shown to yield clots that are more homogeneous than clinical thrombi,²⁶ were assessed in a phantom that did not incorporate the effects of blood flow, and were larger (10 mm diameter) than those typically observed *in vivo*. During the first six hours, clots were kept at room temperature within the MRI bore, which may have affected parameter values. Chosen scan parameters and acquisition hardware were

selected to be directly translatable to *in vivo* head imaging, and hence were not optimized for *in vitro* samples. No histology was performed to confirm that initial sample hematocrit was maintained throughout the experiment; some retraction was observed in the 20 and 30% hematocrit clots and this could have affected their true hematocrit, and measured imaging values, as the experiment progressed. The lipid and calcium components do not perfectly mimic *in vivo* thrombus cholesterol and calcifications. Cholesterol within thromboemboli have been reported to consist of numerous small crystals rather than a singular mass.²⁷ Similarly, thrombus calcifications, often derived from embolized calcifications within atherosclerotic plaque, are composed primarily of calcium apatite,²⁸ which is slightly less diamagnetic than calcium carbonate and will therefore yield reduced QSM contrast.²⁹ Blood-related flow artifacts and signal contamination from the venous system may affect the quantitative maps *in vivo*, particularly for QSM processing,³⁰ but can be minimized through flow compensation and increasing spatial resolution.³¹ Variable flip angle turbo spin echo sequences have also been proposed as method for rapid, single-scan thrombus characterization,³² and while they possess advantages of inherent black blood properties and variable T₁-weighting, these techniques provide only qualitative information and often require contrast administration.³³

2.5 Conclusion

The 10-echo GRE sequence and post-processing algorithms used in this study generated accurate R₂^{*}, QSM and FF maps, which enabled quantitative characterization of blood clot including the ability to estimate hematocrit and age, while also distinguishing lipidic and calcified components. The protocol is readily translatable to the emergency clinic as all quantitative maps were generated from a single, contrast-free six-minute scan.

2.6 References

1. Sharma VK, Teoh HL, Wong LY, Su J, Ong BK, Chan BP. Recanalization therapies in acute ischemic stroke: pharmacological agents, devices, and combinations. *Stroke Res Treatment* 2010;2010:1-8.
2. Niessen F, Hilger T, Hoehn M, Hossmann KA. Differences in clot preparation determine outcome of recombinant tissue plasminogen activator treatment in experimental thromboembolic stroke. *Stroke* 2003;34:2019-2024.
3. Yuki I, Kan I, Vinters H, et al. The impact of thromboemboli histology on the performance of a mechanical thrombectomy device. *AJNR Am J Neuroradiol* 2012;33:643-648.
4. Niesten JM, van der Schaaf IC, van Dam L, et al. Histopathologic composition of cerebral thrombi of acute stroke patients is correlated with stroke subtype and thrombus attenuation. *PLoS One* 2014;9:e88882.
5. Almekhlafi MA, Hu WY, Hill MD, Auer RN. Calcification and endothelialization of thrombi in acute stroke. *Ann Neurol* 2008;64:344-347.
6. Chueh J, Wakhloo A, Hendricks G, Silva C, Weaver J, Gounis M. Mechanical characterization of thromboemboli in acute ischemic stroke and laboratory embolus analogs. *AJNR Am J Neuroradiol* 2011;32:1237-1244.
7. Halloran JI, Bekavac I. Unsuccessful tissue plasminogen activator treatment of acute stroke caused by a calcific embolus. *J Neuroimaging* 2004;14:385-387.
8. Weisel JW, Litvinov RI. The biochemical and physical process of fibrinolysis and effects of clot structure and stability on the lysis rate. *Cardiovasc Hematol Agents Med Chem* 2008;6:161-180.
9. Laridan E, Denorme F, Desender L, et al. Neutrophil extracellular traps in ischemic stroke thrombi. *Ann Neurol* 2017;82:223-232.
10. Schellinger P, Bryan R, Caplan L, et al. Evidence-based guideline: the role of diffusion and perfusion MRI for the diagnosis of acute ischemic stroke Report of the Therapeutics and Technology Assessment

Subcommittee of the American Academy of Neurology. *Neurology* 2010;75:177-185.

11. Liebeskind DS, Sanossian N, Yong WH, et al. CT and MRI early vessel signs reflect clot composition in acute stroke. *Stroke* 2011;42:1237-1243.
12. Kim S, Yoon W, Kim T, Kim H, Heo T, Park M. Histologic analysis of retrieved clots in acute ischemic stroke: correlation with stroke etiology and gradient-echo MRI. *AJNR Am J Neuroradiol* 2015;36:1756-1762.
13. Brinjikji W, Duffy S, Burrows A, et al. Correlation of imaging and histopathology of thrombi in acute ischemic stroke with etiology and outcome: a systematic review. *J Neurointerv Surg* 2017;9:529-534.
14. Walker BS, Shah LM, Osborn AG. Calcified cerebral emboli, a “do not miss” imaging diagnosis: 22 new cases and review of the literature. *AJNR Am J Neuroradiol* 2014;35:1515-1519.
15. Phinikaridou A, Andia ME, Saha P, Modarai B, Smith A, Botnar RM. In vivo magnetization transfer and diffusion-weighted magnetic resonance imaging detects thrombus composition in a mouse model of deep vein thrombosis. *Circ Cardiovasc Imaging* 2013;6:433-440.
16. Saha P, Andia ME, Modarai B, et al. Magnetic resonance T1 relaxation time of venous thrombus is determined by iron processing and predicts susceptibility to lysis. *Circulation* 2013;128:729-736.
17. Clark RA, Watanabe AT, Bradley WG, Roberts JD. Acute hematomas: effects of deoxygenation, hematocrit, and fibrin-clot formation and retraction on T2 shortening. *Radiology* 1990;175:201-206.
18. Chang S, Zhang J, Liu T, et al. Quantitative susceptibility mapping of intracerebral hemorrhages at various stages: mapping of intracerebral hemorrhages. *J Magn Reson Imaging* 2016;44:420-425.
19. Liu J, Drangova M. Method for B0 off-resonance mapping by non-iterative correction of phase-errors (B0-NICE). *Magn Reson Med* 2015;74:1177-1188.
20. Liu J, Liu T, de Rochefort L, et al. Morphology enabled dipole inversion for quantitative susceptibility mapping using structural consistency between the magnitude image and the susceptibility map. *NeuroImage* 2012;59:2560-2568.

21. Liu J, Christiansen SD, Drangova M. Single multi-echo GRE acquisition with short and long echo spacing for simultaneous quantitative mapping of fat fraction, B0 inhomogeneity, and susceptibility. *NeuroImage* 2018;172:703-717.
22. Casaubon LK, Boulanger J-M, Blacquièrè D, et al. Canadian stroke best practice recommendations: hyperacute stroke care guidelines, update 2015. *Int J Stroke* 2015;10:924-940.
23. Rous P, Turner J. The preservation of living red blood cells in vitro. *J Exp Med* 1916;23:219-237.
24. Bradley WG, Schmidt PG. Effect of methemoglobin formation on the MR appearance of subarachnoid hemorrhage. *Radiology* 1985;156:99-103.
25. Janick PA, Hackney DB, Grossman RI, Asakura T. MR imaging of various oxidation states of intracellular and extracellular hemoglobin. *AJNR Am J Neuroradiol* 1991;12:891-897.
26. Robbie L, Young S, Bennett B, Booth N. Thrombi formed in a Chandler loop mimic human arterial thrombi in structure and RAI-1 content and distribution. *Thromb Haemost* 1997;77:510-515.
27. Masuda J, Yutani C, Ogata J, Kuriyama Y, Yamaguchi T. Atheromatous embolism in the brain: a clinicopathologic analysis of 15 autopsy cases. *Neurology* 1994;44:1231-1237.
28. Schmid K, McSharry WO, Pameijer CH, Binette JP. Chemical and physicochemical studies on the mineral deposits of the human atherosclerotic aorta. *Atherosclerosis* 1980;37:199-210.
29. Hopkins JA, Wehrli FW. Magnetic susceptibility measurement of insoluble solids by NMR: magnetic susceptibility of bone. *Magn Reson Med* 1997;37:494-500.
30. Haacke EM, Liu S, Buch S, Zheng W, Wu D, Ye Y. Quantitative susceptibility mapping: current status and future directions. *Magn Reson Imaging* 2015;33:1-25.
31. Rastogi R, Ding Y, Xia S, et al. Recent advances in magnetic resonance imaging for stroke diagnosis. *Brain Circulation* 2015;1:26-37.
32. Yang Q, Duan J, Fan Z, et al. Early detection and quantification of cerebral venous thrombosis by magnetic resonance black-blood thrombus imaging. *Stroke* 2016;47:404-409.

33. Kim J, Park JE, Nahrendorf M, Kim D-E. Direct Thrombus Imaging in Stroke. *J Stroke* 2016;18:286-296.

2.7 Supplementary material

2.7.1 Methods

A calibration phantom was constructed to validate derived fat fraction (FF), quantitative susceptibility mapping (QSM) and R_2^* maps, and included a range of fat-water emulsions stabilized with agar, and aqueous gadolinium (Gd) solutions. Samples with fat fractions of 0.1, 0.2 and 0.5 were prepared by dispersing appropriate amounts of peanut oil into water with 43 mmol/L sodium dodecyl sulfate (Sigma-Aldrich; St. Louis, MO). Samples were emulsified using a sonifier (Branson S-450; Branson Ultrasonics; Danbury, CT) for 2 minutes while heat was applied using a heat gun. Separately, a 4% agar solution (Sigma-Aldrich; St. Louis, MO) was prepared and kept at 70°C using a hot plate. The emulsified oil solution was added dropwise to the agar solution with the mixture being heated and under sonication. An equivalent volume of emulsified oil solution was added to the agar solution such that the final concentration of agar was 2% in all cases. Separately, aqueous Gadolinium solutions (Magnevist; Berlex Laboratories; Wayne, NJ) were prepared at 0.125, 0.25, 0.5, 1, 1.5, 2 and 2.5% of the raw (0.5 mmol/mL Gd) contrast agent, yielding magnetic susceptibility shifts of 0.20, 0.40, 0.81, 1.63, 2.45, 3.26 and 4.08 ppm at room temperature.¹ Control samples of water (FF = 0) and pure peanut oil (FF = 1) were also prepared. All samples were transferred into 1 cm diameter, 5 mL polystyrene vials and placed vertically inside an agar-filled container.

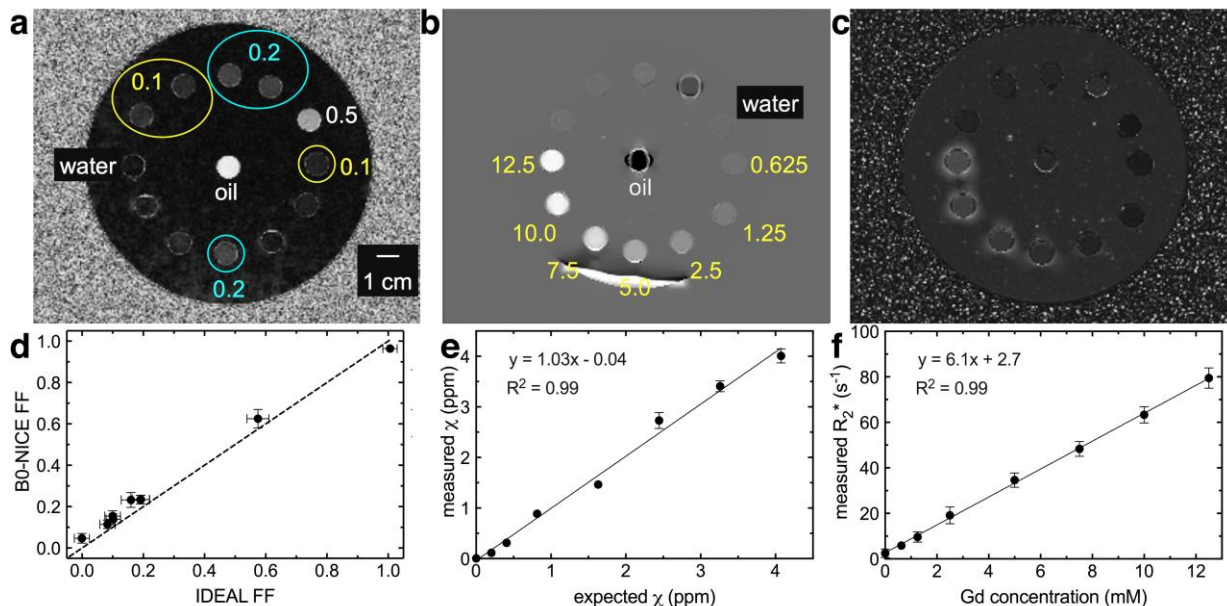
The calibration phantom was scanned with the same 10-echo GRE sequence used for the thrombus phantoms. An additional scan was also performed using the spoiled gradient-echo version of the IDEAL sequence to provide an accepted-standard assessment of the fat fraction of the prepared samples.² IDEAL FF maps were reconstructed on the scanner. Parameters for this scan were as follows: $TE_1 = 1.60$ ms, echo spacing = 0.86 ms, number of echoes = 9,

repetition time = 13.6 ms, bandwidth = 142.86 kHz, flip angle = 5° , field of view = 18 cm, matrix size = 160 x 160 x 20, slice thickness = 4 mm. No averaging was performed.

Following reconstruction and multi-parametric map generation, segmentation of the FF calibration samples was accomplished by placing a 7-mm diameter, 12-mm length cylinder across the middle slices of both the 10-echo maps and the IDEAL FF maps. A 7-mm diameter circular cylindrical region of interest (ROI) drawn across the central slice of the QSM map was used for segmentation of the susceptibility calibration samples. Mean and standard deviation values of the segmented pixels were recorded.

2.7.2 Results

Representative slices from FF, QSM and R_2^* maps and sample values derived from the calibration phantoms are displayed in supplementary Figure 2-1. Agreement was observed between the mean fat fraction values of the FF calibration samples as determined by B0-NICE and IDEAL (supplementary Figure 2-1D), though a slight overestimation of the B0-NICE FF is present (max overestimation = 0.05) for the mixed fat-water emulsions as compared to the IDEAL FF. This discrepancy is likely due to the flip-angle-dependent T_1 effect that biases scans with higher flip angles towards yielding larger FF estimates (FA: 5° and 10° for IDEAL and B0-NICE, respectively).³ A linear trend with a slope approaching unity (slope = 1.03, $R^2 = 0.99$) was observed between the expected and measured susceptibility values for the QSM calibration samples (supplementary Figure 2-1E), indicating the QSM method can perform accurate quantification of susceptibility across a broad range of susceptibility shifts (up to 4.08 ppm). Lastly, a linear relationship was observed between B0-NICE R_2^* and Gd concentration up to 12.5 mmol/L ($R^2 = 0.99$) within the QSM samples (supplementary Figure 2-1F).



Supplementary Figure 2-1: Central coronal slices of the (A) B0-NICE fat fraction (FF) [0, 1], (B) MEDI quantitative susceptibility mapping (QSM) [-1.25 ppm, 3.25 ppm] and (C) B0-NICE R_2^* [0 s⁻¹, 350 s⁻¹] maps. For the FF phantom (A) the nominal fat fraction of each vial is identified; unlabeled vials contain both fat and Gadolinium (Gd) and were not analyzed. For the susceptibility phantom (B, C), labels show Gd concentration (mM); unlabeled vials contain oil/water emulsions. (D) B0-NICE FF plotted against FF measured using the IDEAL sequence; (E) measured QSM against expected sample susceptibility; (F) B0-NICE-derived R_2^* is plotted against Gd concentration. Error bars represent the standard deviation of all pixels within each region of interest. Note that the oil vial displays an artifactual diamagnetic susceptibility on the QSM map because of the varying fat-water phase shifts in the processed echoes.

2.7.3 References

1. de Rochefort L, Liu T, Kressler B, *et al.* Quantitative susceptibility map reconstruction from MR phase data using bayesian regularization: validation and application to brain imaging. *Magn Reson Med* 2010;63:194-206.
2. Reeder SB, McKenzie CA, Pineda AR, *et al.* Water-fat separation with IDEAL gradient-echo imaging. *J Magn Reson Imaging* 2007;25:644-52.
3. Liu C-Y, McKenzie CA, Yu H, *et al.* Fat quantification with IDEAL gradient echo imaging: correction of bias from T1 and noise. *Magn Reson Med* 2007;58:354-64.

CHAPTER 3

Quantitative prediction of stroke thrombus erythrocyte content from ex vivo multiparametric MRI using deep learning

3.1 Introduction

The desired outcome of acute ischemic stroke (AIS) treatment is to achieve rapid recanalization, and yet despite improvements in thrombolytic agents and reperfusion devices, successful recanalization is not achieved in approximately 25% of patients.¹ Thrombus composition has emerged as a significant factor influencing the success of AIS treatment.² Particularly, the proportion of thrombus erythrocyte (red blood cell (RBC)) content has been linked to the efficacy of both recombinant tissue plasminogen activator (rtPA) and endovascular thrombectomy (EVT) therapies.^{3,4} Non-invasive prediction of thrombus RBC content prior to acute treatment would provide a valuable tool for stroke interventionalists, and has been sought through medical imaging.

The presence of qualitative susceptibility vessel and hyperdense artery signs in MR and CT imaging, respectively, have each demonstrated capability for characterizing RBC content categorically, distinguishing between groups such as RBC vs. fibrin-dominant.^{4,5} However, such signs have proven inconsistent in their predictions of thrombus amenability to rtPA and EVT therapies⁶ and have noted issues with inter-scanner variability.⁷ Quantitative imaging techniques utilizing MR R_2^* , quantitative susceptibility

mapping (QSM) values, or CT Hounsfield units have shown promise for more robust, quantitative prediction of RBC content,^{3,8,9} as well as for predicting efficacy of rtPA and EVT therapies.^{10,11} However, these techniques remain limited by their use of a single imaging value or metric to represent entire thrombi. Histological studies have consistently demonstrated that thrombi are heterogeneous and complex in structure,¹² and that complexities such as the distribution of fibrin and RBC components have a material impact on treatment efficacy.¹³

To account for these structural complexities, machine learning techniques have recently started being applied towards thrombus analysis. Past techniques generated models from MR or CT imaging texture features, and have demonstrated sensitivity to clot RBC content *in vitro*^{14,15} as well as an ability to predict clinical features such as response to rtPA.¹⁶ Concerns linger however about the reproducibility of calculated texture features and the generalizability of these techniques.¹⁷ Further still, machine learning techniques are limited by the need to initially handpick extractable features for study; the histomorphological basis underlying the distinguishing ability of imaging texture features is an ongoing area of research.¹⁸

Deep learning neural networks provide a complimentary tool to machine learning techniques with the primary advantage being that featurization, the process of turning raw signal into a modellable predictor, is fully automated. Convolutional neural networks (CNNs) have been successfully applied towards medical imaging problems where relevant imaging features are difficult to define, such as for predicting brain age and aneurysm stability.^{19,20} CNNs have also demonstrated utility in AIS, in areas such as predicting ischemic tissue fate and thrombus detection.^{21,22} However, CNNs have not yet been applied towards analysis of the thrombus itself. In this study, we assess the capability of CNNs for prediction of stroke thrombus RBC content using MR images. Specifically, we trained a CNN on

quantitative MR R_2^* , QSM maps as well as T_2^* -weighted gradient echo (GRE) images of *ex vivo* AIS thrombi retrieved by EVT, investigated the use of data augmentation techniques to improve network performance, and quantitatively assessed the accuracy of the trained CNN for numerical prediction of RBC content.

The methods for prediction of RBC content directly from mean clot R_2^* and QSM, described in Chapter 2, were tested on the human thrombi included in this study but ultimately failed to produce accurate predictions. Thrombus RBC content was consistently underestimated and a Bland-Altman plot of these predictions is shown in this chapter's supplementary material (supplementary Figure 3-1). More advanced image analysis techniques were necessitated, and deep learning was chosen because of its ability to interpret multiple image types simultaneously, a feature found to be important in Chapter 2 wherein the relationship between clot R_2^* and QSM was used to derive RBC predictions.

3.2 Materials and methods

3.2.1 Thrombus collection and storage

Institutional research ethics board approval was obtained for this study. AIS patients who were treated with EVT at the local stroke centre were consecutively enrolled between the periods of February 2016 to November 2017. Retrieved thrombi were stored and transferred to an attached institution for *ex vivo* MR imaging and histological analysis. Patients were excluded if insufficient thrombus material was retrieved for study (>2 mm in all dimensions) or if younger than 18 years old. Informed consent was obtained following the EVT procedure and samples were discarded if consent was refused.

A total of 109 thrombi were collected from 65 AIS patients. Thrombi were stored inside a 150 mL plastic jar containing a non-adherent pad (Telfa; Covidien, Mansfield, MA) wetted with heparinized saline to retain moisture. Those retrieved during the daytime were kept at room temperature and scanned within 6 hours of retrieval, otherwise thrombi were kept inside a refrigerator overnight until the following workday. It was observed that thrombi which had been placed in a fridge and stored overnight had significantly lower R_2^* and QSM values than those kept at room temperature (supplementary Figure 3-2). Due to this effect, only those stored at room temperature were histologically analyzed and included in the study; final sample size was 48 thrombi. Clinical details associated with each group of stored thrombi are listed in Table 3-1.

Table 3-1: Clinical details of the patient cohort for each thrombus storage group

Storage type	Room temperature (n = 31)	Refrigerator (n = 32)
Age (mean \pm SD)	67 \pm 17	70 \pm 12*
Sex, female	14 (45%)	13 (43%)*
Number of thrombi	48	61
Etiology		
Large artery atherosclerosis	6 (20%)	3 (9%)
Cardioembolism	21 (68%)	22 (69%)
Dissection	2 (6%)	1 (3%)
Undetermined	2 (6%)	6 (19%)
Occlusion site		
MCA	25 (81%)	27 (85%)
ICA	1 (3%)	3 (9%)
Vertebrobasilar	5 (16%)	2 (6%)
EVT technique		
Stent	26 (84%)	29 (91%)
Aspiration	5 (16%)	3 (9%)
IV rtPA	15 (48%)	11 (34%)

*n=2 missing data

MCA, middle cerebral artery; ICA, internal carotid artery; IV rtPA, intravenous recombinant tissue plasminogen activator.

3.2.2 *Ex vivo* thrombus imaging

Following storage, the retrieved thrombi were scanned inside 1 cm diameter polystyrene vials containing porcine plasma and vertically inserted into a 15-cm diameter agar-filled container.⁸ A small agar plug was added to the bottom of the vials so that the thrombi sat flat on their surface. When more than one specimen was obtained from a single participant, thrombus pieces were scanned in individual tubes and analyzed separately. Scanning was performed at 3.0 T using a whole-body MRI scanner (GE 750; GE Medical Systems, Milwaukee, WI) with a 32-channel receive head coil. Scans were acquired using a 3D multi-echo bipolar GRE sequence designed for clinical imaging *in vivo*;²³ the sequence includes two 5-echo trains: the first train was optimized for chemical shift imaging (first echo time (TE) = 3.20 ms, echo spacing = 1.46 ms); the second train was optimized to highlight susceptibility-related contrast (first TE = 16.75 ms, echo spacing = 7.15 ms). The remaining scan parameters were repetition time = 47.6 ms, bandwidth = 142.86 kHz, flip angle = 10°; field of view = 18 cm; matrix size = 192 × 192 × 36, for a final voxel dimension of 0.94 × 0.94 × 1.0 mm³. Total acquisition time was 5 minutes 33 seconds. Balanced steady-state gradient echo (FIESTA-C) images with identical resolution and bandwidth were also acquired to facilitate thrombus segmentation (TE = 3 ms, TR: 6.1 ms, flip angle: 40°, phase cycles = 4, scan time = 2 min 47 sec). All scans were acquired in the coronal plane, with the phantom laying flat along the MR table and vials aligned perpendicular to B₀. Thrombi sat horizontal relative to the long axis of the vials, and were also aligned perpendicular to B₀.

3.2.3 Image processing

Image reconstruction was performed in Matlab (Matlab R2019a; Mathworks, Natick, MA) using the Orchestra Software Development Kit (GE Healthcare; Milwaukee, WI). Complex channel combination was performed using singular

value decomposition from which GRE magnitude images were derived. R_2^* and QSM maps were generated using the B0-NICE and MEDI QSM algorithms.^{24,25} Thrombi were segmented from the FIESTA-C images, which were inherently co-registered with the GRE sequence. Thrombus R_2^* , QSM and GRE magnitude pixel values were each separately z-score normalized according to distributions derived from all segmented thrombi.

3.2.4 Histological analysis

Immediately following imaging, thrombi were formalin fixed, embedded in paraffin and arranged for sectioning along the MR slice-encoding direction. Thrombi were sectioned at 5 μm thickness and stained with hematoxylin & eosin. The first 14 were sectioned in 4 evenly spaced regions throughout the thrombi (3 – 4 mm thick on average); it was observed that RBC content varied minimally between thrombus slices, concurring with the findings of Staessens et al.,²⁶ so remaining thrombi were sectioned only once through the middle of each sample (supplementary Figure 3-3). Stained slides were scanned at $\times 40$ magnification. The color segmentation plugin (EPFL, Lausanne, Switzerland) in ImageJ (National Institutes of Health, Bethesda, MD) with post-processing correction for outlying pixels in Matlab was used to quantify thrombus RBC percentage by area.

3.2.5 Deep learning network

3.2.5.1 Network architecture

Using the acquired thrombus MR images, a convolutional neural network (CNN) was trained in Matlab to predict histological RBC content. Two-dimensional slices of the segmented, normalized R_2^* , QSM and late echo GRE magnitude images (TE = 31 ms) were fed into the network as 3-channel RGB images; each image was 49×56 pixels in size. 188 segmented 3-channel slices were available from the 48 analyzed thrombi for training and testing. It was

assumed that all slices from a single thrombus had the same RBC content derived from histology. The network architecture – shown in the schematic illustration in Figure 3-1 – consisted of 2 repeated blocks of a convolutional layer (3×3 , stride of 1, zero-padded), a rectified linear unit (ReLU) and an average-pooling layer (2×2 , stride of 1), followed by a final convolutional layer and ReLU layer, a dropout layer and a fully connected layer with a single output connected to the regression layer. The number of feature channels for each of the convolutional layers was set to 16, 16, and 32, respectively. The Adam optimizer was used with an initial learning rate of 0.001; L2 regularization was implemented with a λ of 0.01. Network parameter weights were trained by minimizing the half mean squared error using stochastic gradient descent.

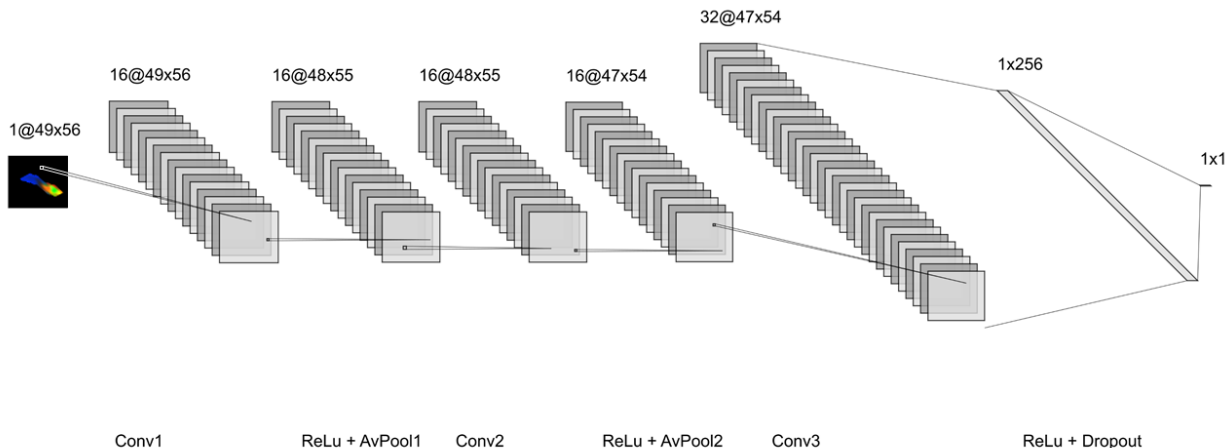


Figure 3-1: Schematic diagram of the CNN. Three-dimensional RGB images consisting of segmented, normalized thrombus R_2^* , QSM and GRE magnitude images are fed into a network consisting of 3 convolutions layers with average pooling layers in between and a dropout layer at the end, before a final fully-connected layer. Padding is employed to retain image size in the convolutional layers.

3.2.5.2 Data augmentation

Given the relatively small thrombus MR slice dataset available for network evaluation, overfitting of the training data was a concern. In light of this,

image data augmentation was employed and implemented to various degrees in order to observe its effect on network performance. Augmentation consisted of three distinct components: input sampling equalization, image transformation, and dataset duplication.

For input sampling equalization, oversampling of training data was performed to equalize the distribution of thrombus RBC content. Thrombus MR slices randomly selected to be in the training set were first binned based on RBC content in 5% intervals, and underrepresented bins had all slices repeatedly sampled until their count equaled the nearest integer multiple of the bins original slice count less than or equal to the most represented bin. This resampling strategy is similar to the class-aware sampling strategy that has previously been employed on categorical data.²⁷ A representative training set RBC distribution before and after input sampling equalization is shown in Figure 3-2.

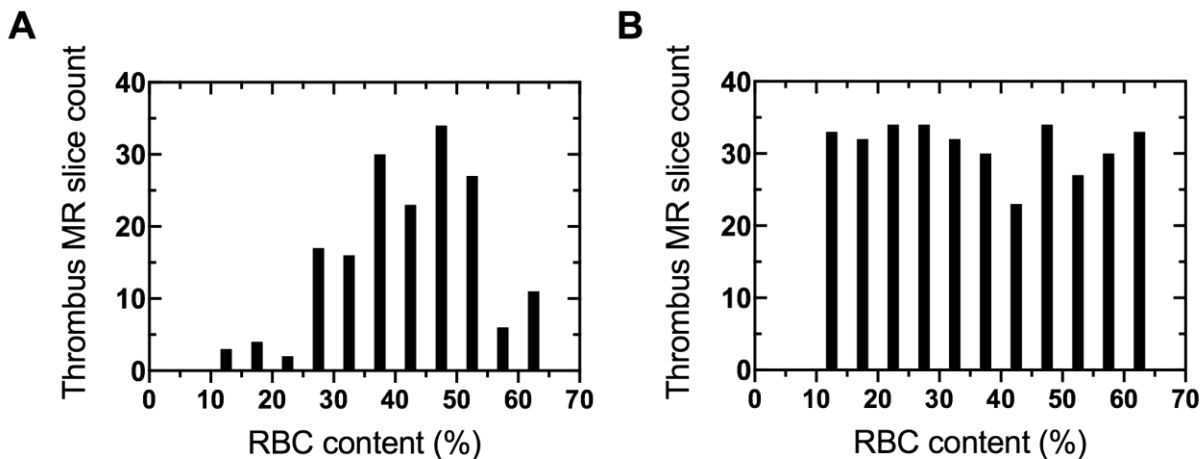


Figure 3-2: Representative training set thrombus RBC content distribution (A) before and (B) after input sampling equalization.

For image transformation, a group of geometric transformations were randomly applied to both the training and testing datasets. Random transformations were performed within predefined ranges: rotations between -90 to 90° , integer vertical and horizontal translations up to 5 pixels,

reflections across the X and Y axis, scaling between 0.7 to 1.3 and shearing between -30 to 50° . An example 3-channel thrombus input slice before and after transformation, with its base images, is shown in Figure 3-3.

Finally, for dataset duplication the entire training set was copied at up to a $\times 5$ multiple prior to network training. When employed, it was implemented after input sampling equalization and before image transformation, so that all slices inputted into the network were unique.

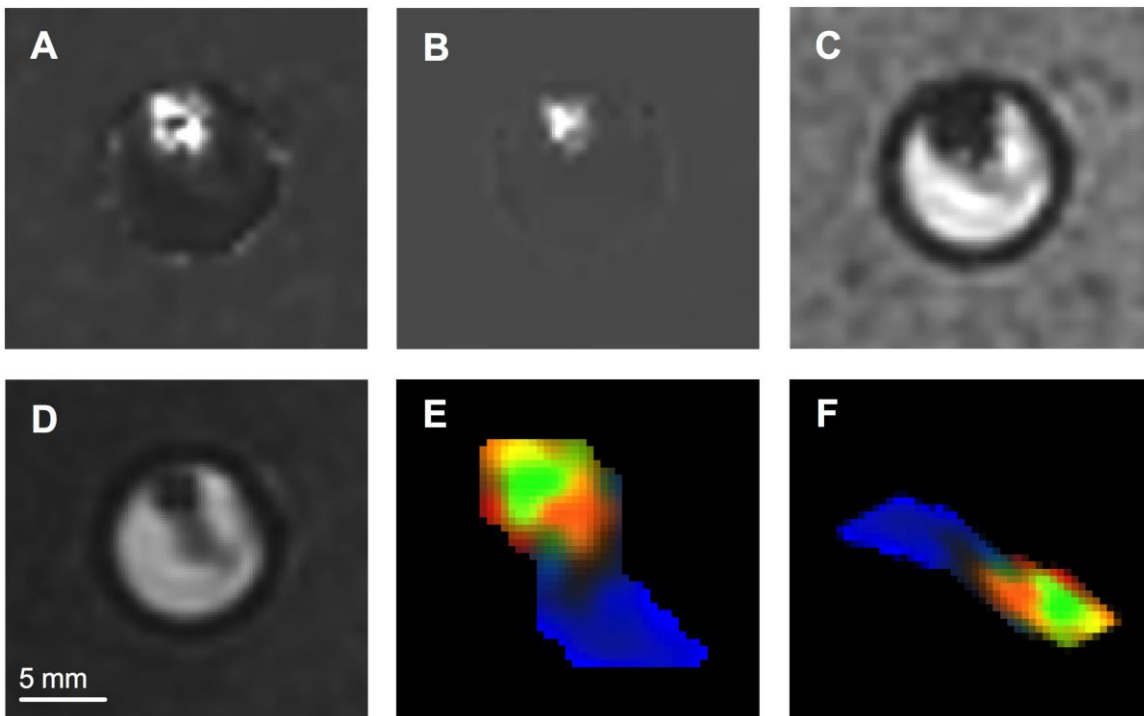


Figure 3-3: An example thrombus (A) R_2^* , (B) QSM, (C) GRE magnitude image slice, shown inside its scanning vial, along with the (D) FIESTA-C image used for segmentation. The resulting normalized, segmented thrombus RGB image slice used as CNN input is shown (E) before and (F) after random image transformation. R_2^* , QSM and GRE magnitude pixel values represent the red, green and blue image color channels, respectively.

3.2.5.3 Network evaluation

The network was evaluated using 8-fold cross validation, where the mean accuracy (proportion of predictions within 10% of histology), absolute error

and root mean square error (RMSE) across all folds were used for network assessment. Care was taken to ensure no slices associated with the same thrombus were mixed between the training and testing subsets within each cross-validation fold. The network was separately trained and evaluated with 8 different data augmentation strategies: no augmentation, input sampling equalization or image transformation only, input sampling equalization and image transformation, and input sampling equalization and image transformation with dataset duplication of $\times 2 - \times 5$ multiples. Across each of these network implementations hyperparameters sensitive to the size of the input dataset were iteratively tested: training epochs were varied between 4 to 9 in steps of 1, batch size was varied between 6, 8 and 12, and dropout was varied between 0 to 0.4 in steps of 0.1. Results from the best network iteration associated with each data augmentation strategy were recorded. The training time for a single 8-fold cross validation experiment was as fast as 86 seconds for the unaugmented dataset to as long as 32 minutes for the $\times 5$ duplicated, equalized, transformed dataset on a dual-core CPU (Intel Core i5) with 16 Gb of RAM.

3.2.6 Statistical analysis

In addition to accuracy, absolute error and RMSE, network performance was also evaluated as the correlation between histological and predicted RBC content, using Pearson's r and slope. Statistical analysis was performed using GraphPad Prism (v8.2.1; GraphPad Software, La Jolla, CA).

3.3 Results

The mean thrombus RBC content determined from histological analysis was $39 \pm 13\%$ (median: 38%; interquartile range: 30 – 49%; min: 12%, max: 61%). Results from the best-performing network iterations for predicting

histological RBC content at each level of data augmentation are shown in Table 3-2.

In general, the networks correctly predicted thrombus RBC content, with an accuracy and error that improved as more extensive augmentation was performed, as expected. In particular, a large improvement in network accuracy was seen after both input sampling equalization and image transformation were applied, increasing it from 66% to approximately 72%. With both equalization and transformation applied, increased training set duplication did not further increase accuracy but minorly improved RMSE from 10.3% to approximately 9.8%. For reference, a naive prediction (prediction of the overall mean histological RBC percentage for all thrombi) would produce an accuracy, absolute error and RMSE of 54.2, 10.5 and 12.4%, respectively.

Table 3-2: Performance of the CNN for thrombus histological RBC content prediction (T/F: true/false; ×n: training set duplication by a factor of n)

Input equalization	Image transformation	Training set duplication	Accuracy (%)	Absolute error (%)	RMSE (%)	r	Slope
F	F	×1	66.1	8.26	9.83	0.51	0.25
T	F	×1	66.5	8.22	10.06	0.40	0.22
F	T	×1	67.5	8.06	10.03	0.27	0.08
T	T	×1	73.9	7.99	10.33	0.46	0.24
T	T	×2	72.1	8.07	9.85	0.53	0.29
T	T	×3	71.0	7.85	9.91	0.53	0.33
T	T	×4	72.2	8.01	9.83	0.55	0.32
T	T	×5	72.2	8.15	9.82	0.57	0.34

Regression curves plotting the median predicted thrombus RBC content against that determined through histology were used to determine correlation coefficients and linear regression slopes, and are listed for each best-performing network iteration in Table 3-2. Here, input equalization and image transformation applied individually decreased correlation and regression slopes compared to the unmodified dataset, but with both applied

training set duplication improved correlation and slope up to 0.57 and 0.34, respectively, in the $\times 5$ duplicated dataset.

Regression plots from the network iterations with the best accuracy, absolute error and RMSE (bold in Table 3-2) are shown in Figures 3-4A – C. Despite the highest accuracy achieved being the network iteration trained on augmented data at only $\times 1$ duplication, its distribution of RBC content predictions is noticeably flatter than those trained on larger datasets, implying the network learned to make predictions only within a narrow range of RBC content. This yields poor prediction accuracy in thrombi with very high or low RBC content, resulting in a high RMSE value of 10.33%, the largest in Table 3-2. RMSE weighs large individual residuals more heavily than absolute error; the discrepancy between this network iteration's high accuracy and poor RMSE underscores the need to consider multiple descriptive statistics when evaluating network ability.

In general, all networks predicted RBC content more accurately in thrombi whose histological values were closer to the mean than in those further outside it. When the thrombi included in the regression plots are limited to a narrower range of RBC content closer to the mean (20 – 45%), slopes of the prediction curves increase substantially, reaching up to 0.89 in the network trained on the $\times 5$ duplicated dataset (Figures 3-4D – F). Network performance results corresponding to this trimmed subset of predictions are listed in Table 3-3. In this subset network performance is greatly improved compared to that achieved on the entire dataset, suggesting that this network may be capable of producing more accurate RBC content predictions when trained on larger data sets, but is hindered here by the limited data available for thrombi with less common RBC content.

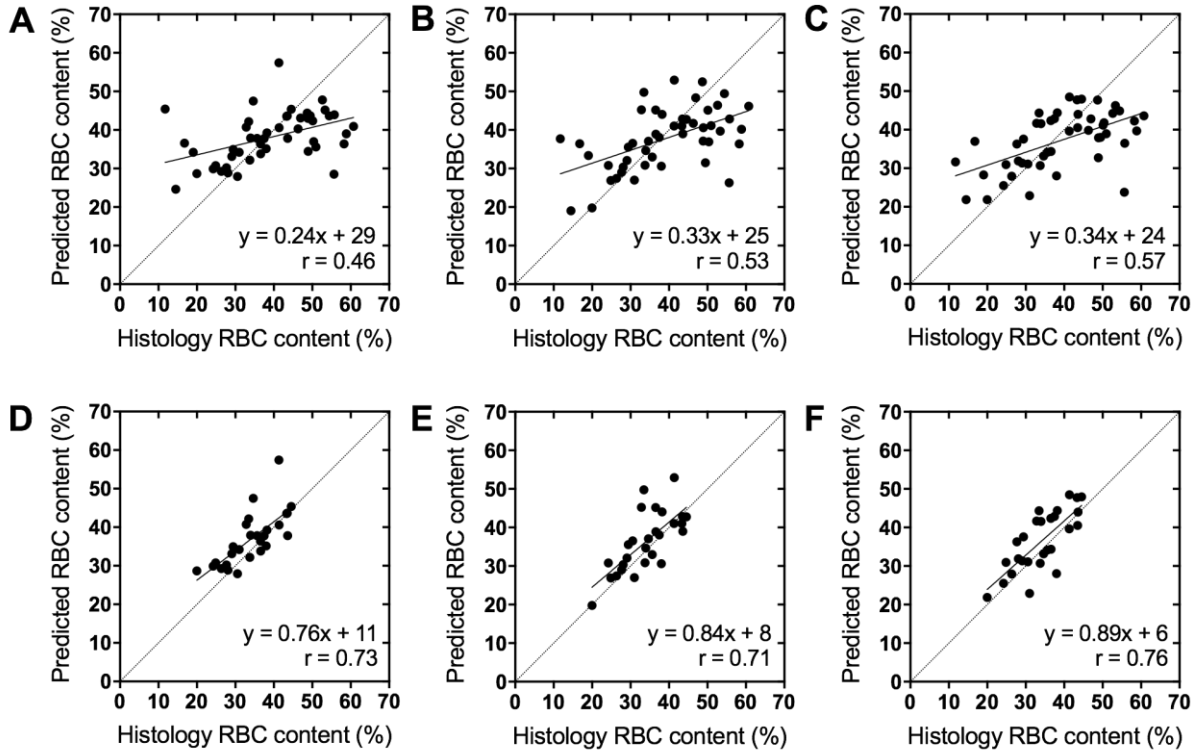


Figure 3-4: Linear regression plots of the CNN predicted thrombus RBC content against the histological value for best-performing network iterations on the equalized, transformed dataset with (A) $\times 1$, (B) $\times 3$, and (C) $\times 5$ duplication, respectively. Plotted are the median predictions from all MR slices available for each thrombus. These same predictions replotted with only thrombi with histological RBC content between 20 – 45% are shown in (D), (E) and (F), respectively.

Table 3-3: Performance of the CNN for thrombus histological RBC content prediction when limited to thrombi between 20 – 45% RBC content (T/F: true/false; $\times n$: training set duplication by a factor of n)

Input equalization	Image transformation	Training set duplication	Accuracy (%)	Absolute error (%)	RMSE (%)	r	Slope
F	F	$\times 1$	77.8	5.51	7.38	0.48	0.44
T	F	$\times 1$	77.8	6.82	7.87	0.52	0.59
F	T	$\times 1$	59.3	8.42	10.69	0.08	0.03
T	T	$\times 1$	92.6	4.07	5.64	0.73	0.76
T	T	$\times 2$	88.9	4.48	5.49	0.73	0.8
T	T	$\times 3$	88.9	4.31	5.87	0.71	0.84
T	T	$\times 4$	92.6	4.77	6.01	0.68	0.76
T	T	$\times 5$	96.3	4.65	5.58	0.76	0.89

3.4 Discussion

In order to evaluate the ability of CNNs to predict AIS thrombus RBC content, we trained a 3-layer CNN on segmented thrombus MR images acquired *ex vivo*. Even with a modest dataset of 48 thrombi (188 slices) for training, this study demonstrates that a CNN is capable of predicting RBC content in AIS thrombi solely from MR images with an average accuracy above 70%. This was achieved by using data augmentation strategies designed to increase the effective size of the dataset and reduce overfitting. In spite of augmentation, predictions of RBC content in thrombi with histological values closer to the mean were more accurate than those outside of it, suggesting the CNN did not have sufficient training data available to learn to accurately predict across the full range of thrombus RBC content.

Our CNN was trained on *ex vivo* images of retrieved AIS thrombi. We chose to perform this study *ex vivo* to allow easier patient recruitment while minimizing patient burden. Our *ex vivo* imaging protocol is similar to that of previous *in vitro* blood clot imaging experiments,^{8,9} and *ex vivo* thrombus MR microscopy studies.²⁸ However, unlike previous *ex vivo* thrombus imaging studies, we noted a significant storage effect on the MR values of retrieved thrombi. Stroke thrombi retrieved at night were stored in a refrigerator until they could be scanned the next available workday, and these thrombi had significantly lower R_2^* and QSM values than those scanned within the same day and kept at room temperature. Cold temperatures increase hemoglobin's oxygen affinity, which may have led to thrombus reoxygenation resulting in reduced MR R_2^* and QSM values.²⁹ An explicit examination into the effect of various storage conditions on the MR imaging values of stroke thrombi is outside the scope of this report and warrants closer study.

Due to the abovementioned storage effect limiting our dataset to just 188 segmented thrombus slices available for training and testing, we investigated

the use of data augmentation techniques for improving CNN performance. Data augmentation is a widely used method for increasing the diversity and depth of input data to improve deep learning network performance, largely by reducing network overfitting of training data.³⁰ Here, we oversampled our dataset such that thrombi of all RBC contents were equally represented in the training dataset. Input sampling equalization through oversampling is one of the most common methods for dealing with class imbalance in deep learning, and forces the network to learn features relevant to the entire dataset rather than just the most common entries.³¹ Additionally, we applied a multitude of random image transformations to our dataset, which has shown to outperform single transformations applied on their own.^{32,33} We used geometric transformations specifically to avoid the network focusing on irrelevant characteristics of the thrombi such as orientation and shape, the latter of which can be altered during thrombectomy. Finally, we increased the size of the training dataset directly by duplicating the entire set prior to image transformation, which has proven to improve the performance of CNNs trained on small datasets.³³ We applied these data augmentation techniques sequentially, and it is notable that the largest improvements in network performance relative to the original, unaugmented dataset were observed only after input equalization and image transformation were applied together. This highlights the benefit of having both balanced and varied datasets when training a CNN for thrombus RBC content prediction.

With the use of data augmentation techniques, the CNN was able to learn to predict RBC content in thrombi with approximately 72% accuracy and 8% mean absolute error. It is difficult to precisely define what level of accuracy would be required for a thrombus RBC content predictor to be clinically useful. Studies examining the relationship between histological thrombus RBC content and successful recanalization following EVT have found an average RBC content difference of approximately 17%,^{3,34} while in one study

the difference between rtPA-resistant thrombi and those untreated was approximately 10%.³⁵ A mean absolute error less than the average difference between these clinical groups suggests that even a CNN trained on a small dataset has the potential to be clinically useful, particularly considering that an improvement in the network's performance would reasonably be expected if trained directly for these tasks.

Despite the respectable overall accuracy, weaknesses were apparent in that the predictive ability of the CNN was noticeably poorer for thrombi with RBC content outside the mean histological value. We showed regressive plots of the most accurate portion of the thrombus predictions to demonstrate the CNNs potential capability when given a richer dataset, but the cut-offs to where CNN accuracy decreased are instructive. RBC content prediction accuracy was poor in thrombi with a less than 20% or greater than 45% RBC percentage. Just 4 thrombi had RBC content less than 20%, so it is reasonable that the CNN would perform poorly in this subset due to a lack of representative data, even after input sampling equalization. In contrast however, 17 of the 48 thrombi had an RBC content greater than 45%. This bound could instead be reflective of the fact that blood clots with 40-60% RBC content have similar R_2^* rates due to their similarly heterogeneous composition; this may have reduced their distinguishability within the CNN.⁸ While it is expected that the CNN performance would improve with additional thrombi available for study, this suggests that predicting RBC content of thrombi in the range of 40-60% in particular may be more challenging. Studies have not demonstrated a benefit, however, for finely differentiating between RBC-rich thrombi; current research suggests that all thrombi in this RBC content range would likely yield successful recanalization when treated with EVT, for example.^{3,34}

This study has a number of limitations. We made the assumption that all 2D imaging slices from same thrombus had an RBC content equal to the single

value derived from histology. While there is evidence suggesting that composition varies little throughout thrombi,²⁶ slight variations in RBC content across each MR slice would limit the CNN accuracy. We used an 8-fold cross validation to evaluate our network instead of defining a distinct testing set. Doing so means the generalizability of the network maybe be overestimated, but cross-validation has been recommended for datasets that are too small to include a test set of meaningful size.³⁶ Finally, we performed our imaging *ex vivo* after thrombi had been retrieved through EVT. This allowed us to perform our imaging study without impacting the course of patient treatment, but introduces potential confounding factors which could affect imaging results such as the effect of thrombus storage outside the body, potential alterations in the thrombus structure during the EVT procedure, and differences in temperature and field inhomogeneity relative to *in vivo* imaging. Chosen scan parameters and acquisition hardware were selected to be directly translatable to *in vivo* head imaging, and hence were not optimized for *ex vivo* samples. Performing the study *ex vivo* also meant that the samples were limited to stroke thrombi that were retrievable by EVT and that did not resolve following rtPA administration. While evaluation of this technique *in vivo* with a larger sample size is ultimately required to demonstrate utility in AIS patients, the results presented here suggest CNNs are capable of predicting stroke thrombus RBC content using MR images.

3.5 Conclusion

In this study, we demonstrated that a 3-layer CNN is capable of RBC content prediction in AIS thrombi using *ex vivo* R_2^* , QSM and late-echo GRE magnitude MR images. We improved CNN performance by employing data augmentation involving equalized input sampling, geometric transformation and duplication of the dataset. Our trained network predicted thrombus RBC

content with an overall accuracy of approximately 72% and an absolute error of approximately 8%. The rapid imaging protocol and straightforward network design used in this study enables ready translation towards *in vivo* imaging for prediction of thrombus RBC content in AIS patients.

3.6 References

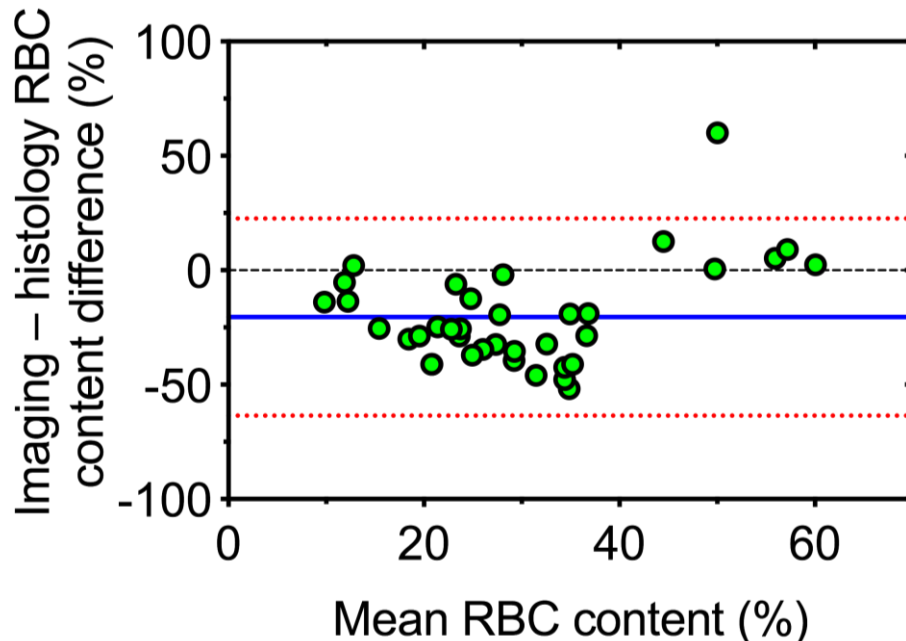
1. Ferrigno M, Bricout N, Leys D, et al. Intravenous recombinant tissue-type plasminogen activator: influence on outcome in anterior circulation ischemic stroke treated by mechanical thrombectomy. *Stroke* 2018;49:1377-1385.
2. Heo JH, Nam HS, Kim YD, et al. Pathophysiologic and therapeutic perspectives based on thrombus histology in stroke. *J Stroke* 2020;22:64.
3. Sporns PB, Hanning U, Schwindt W, et al. Ischemic stroke: histological thrombus composition and pre-interventional CT attenuation are associated with intervention time and rate of secondary embolism. *Cerebrovasc Dis* 2017;44:344-350.
4. Choi MH, Park GH, Lee JS, et al. Erythrocyte fraction within retrieved thrombi contributes to thrombolytic response in acute ischemic stroke. *Stroke* 2018;49:652-659.
5. Liebeskind DS, Sanossian N, Yong WH, et al. CT and MRI early vessel signs reflect clot composition in acute stroke. *Stroke* 2011;42:1237-1243.
6. Yamamoto N, Satomi J, Harada M, Izumi Y, Nagahiro S, Kaji R. Is the susceptibility vessel sign on 3-Tesla magnetic resonance T2*-weighted imaging a useful tool to predict recanalization in intravenous tissue plasminogen activator? *Clin Neuroradiol* 2014;26:317-323.
7. Bourcier R, Détraz L, Serfaty JM, et al. MRI interscanner agreement of the association between the susceptibility vessel sign and histologic composition of thrombi. *J Neuroimaging* 2017;27:577-582.
8. Christiansen SD, Liu J, Boffa MB, Drangova M. Simultaneous R2* and quantitative susceptibility mapping measurement enables differentiation of thrombus hematocrit and age: an in vitro study at 3 T. *J Neurointerv Surg* 2019;11:1155-1161.
9. Bourcier R, Pautre R, Mirza M, et al. MRI quantitative T2* mapping to predict dominant composition of in vitro thrombus. *AJNR Am J Neuroradiol* 2019;40:59-64.
10. Bourcier R, Brecheteau N, Costalat V, et al. MRI quantitative T2* mapping on thrombus to predict recanalization after endovascular

- treatment for acute anterior ischemic stroke. *J Neuroradiol* 2017;44:241-246.
11. Bouchez L, Altrichter S, Pellaton A, et al. Can clot density predict recanalization in acute ischemic stroke treated with intravenous tPA? *Clin Transl Neurosci* 2017;1:1-6.
 12. Staessens S, De Meyer SF. Thrombus heterogeneity in ischemic stroke. *Platelets* 2020; doi: 10.1080/09537104.2020.1748586 [Epub ahead of print: 20 Apr 2020].
 13. Autar AS, Hund HM, Ramlal SA, et al. High-resolution imaging of interaction between thrombus and stent-retriever in patients with acute ischemic stroke. *J Am Heart Assoc* 2018;7:e008563.
 14. Bretzner M, Lopes R, McCarthy R, et al. Texture parameters of R2* maps are correlated with iron concentration and red blood cells count in clot analogs: a 7-T micro-MRI study. *J Neuroradiol* 2019;47:306-311.
 15. Gonzalez AV, Buerke B, Görlich D, et al. Clot analog attenuation in non-contrast CT predicts histology: an experimental study using machine learning. *Transl Stroke Res* 2020;11:940-949.
 16. Qiu W, Kuang H, Nair J, et al. Radiomics-based intracranial thrombus features on CT and CTA predict recanalization with intravenous alteplase in patients with acute ischemic stroke. *AJNR Am J Neuroradiol* 2019;40:39-44.
 17. Berenguer R, Pastor-Juan MdR, Canales-Vázquez J, et al. Radiomics of CT features may be nonreproducible and redundant: influence of CT acquisition parameters. *Radiology* 2018;288:407-415.
 18. Penzias G, Singanamalli A, Elliott R, et al. Identifying the morphologic basis for radiomic features in distinguishing different Gleason grades of prostate cancer on MRI: preliminary findings. *PLoS One* 2018;13:e0200730.
 19. Cole JH, Poudel RP, Tsagkrasoulis D, et al. Predicting brain age with deep learning from raw imaging data results in a reliable and heritable biomarker. *NeuroImage* 2017;163:115-124.
 20. Bhurwani MMS, Waqas M, Podgorsak AR, et al. Feasibility study for use of angiographic parametric imaging and deep neural networks for intracranial aneurysm occlusion prediction. *J Neurointerv Surg* 2020;12:714-719.

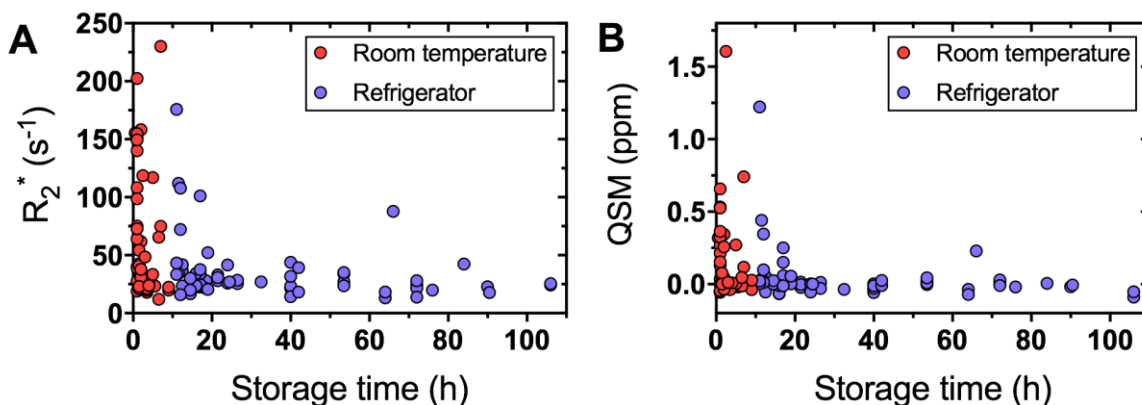
21. Nielsen A, Hansen MB, Tietze A, Mouridsen K. Prediction of tissue outcome and assessment of treatment effect in acute ischemic stroke using deep learning. *Stroke* 2018;49:1394-1401.
22. Lisowska A, Beveridge E, Muir K, Poole I. Thrombus detection in CT brain scans using a convolutional neural network. *Proc BIOSTEC*; 2017. p. 24-33.
23. Liu J, Christiansen SD, Drangova M. Single multi-echo GRE acquisition with short and long echo spacing for simultaneous quantitative mapping of fat fraction, B0 inhomogeneity, and susceptibility. *NeuroImage* 2018;172:703-717.
24. Liu J, Drangova M. Method for B0 off-resonance mapping by non-iterative correction of phase-errors (B0-NICE). *Magn Reson Med* 2015;74:1177-1188.
25. Liu J, Liu T, de Rochefort L, et al. Morphology enabled dipole inversion for quantitative susceptibility mapping using structural consistency between the magnitude image and the susceptibility map. *NeuroImage* 2012;59:2560-2568.
26. Staessens S, Fitzgerald S, Andersson T, et al. Histological stroke clot analysis after thrombectomy: technical aspects and recommendations. *Int J Stroke* 2019;15:467-476.
27. Shen L, Lin Z, Huang Q. Relay backpropagation for effective learning of deep convolutional neural networks. *European conference on computer vision*: Springer; 2016. p. 467-482.
28. Vidmar J, Bajd F, Milosevic ZV, Kocijancic IJ, Jeromel M, Sersa I. Retrieved cerebral thrombi studied by T2 and ADC mapping: preliminary results. *Radiol Oncol* 2019;53:427-433.
29. Spees WM, Yablonskiy DA, Oswood MC, Ackerman JJH. Water proton MR properties of human blood at 1.5 Tesla: magnetic susceptibility, T1, T2, T* 2, and non-Lorentzian signal behavior. *Magn Reson Med* 2001;45:533-542.
30. Shorten C, Khoshgoftaar TM. A survey on image data augmentation for deep learning. *J Big Data* 2019;6:60.
31. Buda M, Maki A, Mazurowski MA. A systematic study of the class imbalance problem in convolutional neural networks. *Neural Networks* 2018;106:249-259.

32. Dosovitskiy A, Springenberg JT, Riedmiller M, Brox T. Discriminative unsupervised feature learning with convolutional neural networks. *Adv Neural Inf Process Syst*; 2014. p. 766-774.
33. Perez F, Vasconcelos C, Avila S, Valle E. Data augmentation for skin lesion analysis. *arXiv preprint* 2018.
34. Shin JW, Jeong HS, Kwon H-J, Song KS, Kim J. High red blood cell composition in clots is associated with successful recanalization during intra-arterial thrombectomy. *PLoS One* 2018;13:e0197492.
35. Qureshi AI, Qureshi MH, Lobanova I, et al. Histopathological characteristics of IV recombinant tissue plasminogen -resistant thrombi in patients with acute ischemic stroke. *J Vasc Interv Neurol* 2016;8:38-45.
36. Dreiseitl S, Ohno-Machado L. Logistic regression and artificial neural network classification models: a methodology review. *J Biomed Inf* 2002;35:352-359.

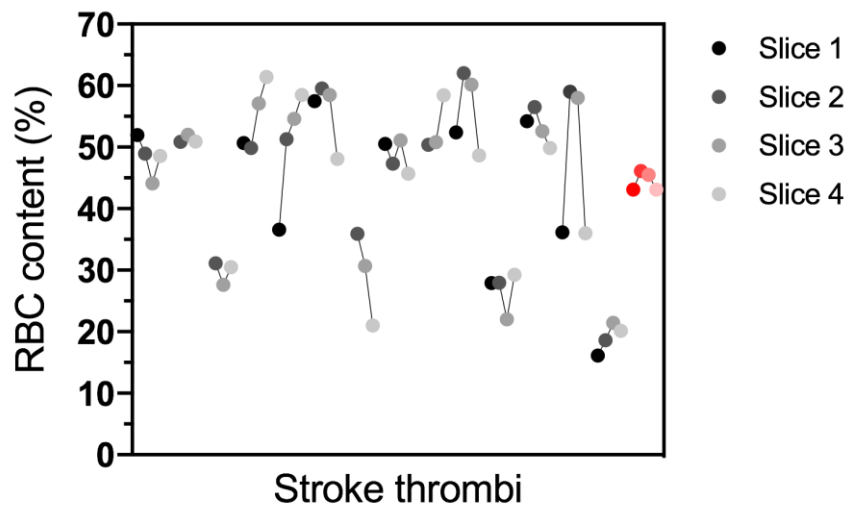
3.7 Supplementary material



Supplementary Figure 3-1: Bland-Altman plot showing the difference between thrombus histological RBC content and that predicted through mean R_2^* and QSM values using the methods described in Chapter 2. Predicted RBC content consistently underestimated the histological values, yielding a mean error of $20 \pm 22\%$ and a mean absolute error of $25 \pm 16\%$.



Supplementary Figure 3-2: Effect of storage method and time between thrombus retrieval and MR imaging on mean thrombus (A) R_2^* and (B) QSM values. Thrombi were either stored at room temperature and scanned within the same workday, or stored in a fridge until the next available workday. Two-tailed T-tests between the two groups R_2^* and QSM values yielded significant differences with $p = 0.0005$ and $p = 0.02$, respectively.



Supplementary Figure 3-3: Thrombus multi-section histological results. Mean RBC content is shown at 3 or 4 evenly spaced intervals through the retrieved stroke thrombi. Red dots indicate the average RBC content values at each slice for all thrombi.

CHAPTER 4

Ex vivo thrombus MR imaging features and patient clinical data enable prediction of acute ischemic stroke etiology

4.1 Introduction

Determination of acute ischemic stroke etiology is a critical component of reducing stroke recurrence risk, but in current clinical practice etiology remains undetermined in approximately one third of cases.¹ Histological analysis of retrieved thrombi has demonstrated that thrombus composition, particularly red blood cell (RBC) content, can be used to differentiate between etiologies, but histological analysis is impractical as a rapid diagnostic tool.²⁻⁴ Medical imaging offers the potential to non-invasively infer information, including but not limited to thrombus composition, supporting the prompt determination of stroke etiology.

Magnetic resonance (MR) imaging and computed tomography (CT) have each demonstrated sensitivity to thrombus RBC content, through the qualitative susceptibility vessel and hyperdense artery signs, respectively.⁵⁻⁷ However, a recent meta-analysis found no significant association between these signs and stroke etiology, and an analysis of the THRACE randomized controlled trial found the diagnostic accuracy of the susceptibility vessel sign for etiology determination to be just 49%.^{8,9} Quantitative MR and CT techniques, in particular those measuring R_2^* and quantitative susceptibility mapping (QSM) or Hounsfield units, respectively, have demonstrated ability to

quantitatively assess the RBC content of prepared blood clots *in vitro*,¹⁰⁻¹³ but these values too have failed to produce significant associations with stroke etiology *in vivo*.^{14,15} Past imaging approaches for stroke thrombus characterization may be limited by their use of a single imaging value or metric to represent entire thrombi, which is discordant with histological studies demonstrating that the structure of stroke thrombi is complex and heterogeneous.¹⁶

Radiomics is the conversion of medical images to mineable high-dimensional data, from which quantitative imaging features can be derived.¹⁷ Such imaging features may be used as input into machine learning algorithms, enabling analysis of information within contexts beyond that perceptible to the human eye. Imaging features related to object texture, in particular, have demonstrated aptitude for characterization of tissues with heterogeneous structure, such as tumours.¹⁸⁻²¹ In the field of stroke imaging, texture features have been used to predict post-stroke impairment and in lesion detection.^{22,23} They have also been applied towards the characterization of thrombi, showing sensitivity to RBC content *in vitro* on R_2^* maps as well as for predicting response to intravenous recombinant tissue plasminogen activator (rtPA) and endovascular therapies (EVT) in stroke thrombi *in vivo* on non-contrast CT.²⁴⁻²⁶ However, texture features have not been previously applied in stroke thrombi towards the determination of etiology.

In this study, we evaluate the ability of radiomics features applied to quantitative MR images of retrieved ischemic stroke thrombi, in combination with patient clinical data, for the prediction of stroke etiology using machine learning. Specifically, we extract image size, shape and texture features from *ex vivo* thrombus R_2^* , QSM and fat fraction (FF) maps, and mine clinical characteristics of the stroke patients, to train random forest classifiers which discriminate between cardioembolic (CE) and large artery atherosclerotic (LAA) stroke.

In contrast to the deep learning methods described in Chapter 3, machine learning was used in this study because it more readily allows the derivation of models that incorporate thrombus MR imaging and patient clinical data together.

4.2 Materials and methods

4.2.1 Study design and inclusion criteria

Institutional research ethics board approval was obtained for this study. Acute ischemic stroke patients treated with EVT at London Health Sciences Centre University Campus were consecutively enrolled between the periods of February 2016 to November 2017 and October 2019 to March 2020. Data from the earlier (training) cohort were used to select relevant imaging and clinical features and train the machine learning models, while data from the later (validation) cohort were used to evaluate their performance against an independent dataset. Patients or their substitute decision makers were made aware of the study at the time consent was given for EVT, and gave informed consent after the procedure was completed and a thrombus was retrieved. EVT was performed using a stentriever or Penumbra System® at the interventionalist's discretion. Inclusion criteria for the study were age greater than 18 years old, CE or LAA stroke etiology, no recent prior stroke and sufficient thrombus material retrieved for study (>2 mm in all dimensions). Thrombi were saved upon retrieval for subsequent MR imaging.

Patient clinical data was collected and used as additional input in the machine learning models. Clinical history parameters obtained for the study included: age, gender, prior stroke history, hypertension, diabetes, hyperlipidemia, coronary artery disease, cardiac valve disease, peripheral artery disease, smoking history, prior deep vein thrombosis, chronic kidney

disease, obesity, prior infections, active cancer, antiplatelet usage, anticoagulant usage, and stroke etiology as determined by the Trial of ORG 10172 in Acute Stroke Treatment (TOAST) criteria.²⁷ Procedural parameters included: rtPA administration, intracerebral hemorrhage, stroke recurrence, final TICI score, arrival NIHSS, occlusion side, occlusion location, number of EVT passes, and EVT duration. Blood work parameters included: triglycerides, cholesterol, high-density lipoprotein, low-density lipoprotein, glucose, leukocytes, and troponin.

With the exception of stroke etiology, all clinical parameters included in this study are obtainable within a few days of acute stroke; this was to ensure that derived models are applicable within the acute to subacute stage of stroke treatment. A summary of basic clinical data for both the training and validation cohorts is given in Table 4-1.

4.2.2 Thrombus storage and imaging

Thrombi retrieved in the training cohort were stored inside a 150 mL plastic jar containing a gauze pad (TELFTM) wetted with heparinized saline to retain moisture. Those retrieved during the daytime were kept at room temperature and scanned within 6 hours of retrieval; otherwise thrombi were kept in a refrigerator until the following workday. All thrombi retrieved in the validation cohort were kept at room temperature and scanned within 6 hours of retrieval.

Table 4-1: Summary of clinical details for each patient cohort

Patient cohort	Training (n = 49)	Validation (n = 9)
Age (mean \pm SD)	72 \pm 15	74 \pm 17
Sex, female	20 (41%)	4 (44%)
Etiology		
Large artery atherosclerosis	8 (16%)	4 (44%)
Cardioembolism	41 (84%)	5 (56%)
Number of thrombi	76	15
Large artery atherosclerosis	15 (20%)	7 (47%)
Cardioembolism	61 (80%)	8 (53%)
IV tPA	18 (37%)	4 (44%)
Occlusion site		
ICA	3 (7%)	0 (0%)
ICA + MCA M1	9 (18%)	3 (33%)
MCA M1	20 (41%)	4 (44%)
MCA M1 + M2	3 (6%)	1 (11%)
MCA M2	9 (18%)	1 (11%)
Vertebrobasilar	5 (10%)	0 (0%)
EVT technique		
Stent	43 (88%)	9 (100%)
Aspiration	6 (12%)	0 (0%)
Prior stroke	10 (20%)	2 (22%)
Hypertension	34 (69%)	7 (78%)
Diabetes	6 (12%)	3 (33%)
Obesity	2 (4%)	0 (0%)
Smoking, past 5 years	5 (10%)	4 (44%)
Hyperlipidemia	23 (47%)	7 (78%)
Coronary artery disease	10 (20%)	4 (44%)
Cardiac valve disease	4 (8%)	1 (11%)
Chronic kidney disease	0 (0%)	2 (2%)

Thrombi were scanned inside 1 cm diameter polystyrene vials containing porcine plasma, inserted vertically into an agar-filled container. A small agar plug was placed at the bottom of the vials so that the thrombi sat flat on their surface. When more than one thrombus specimen was obtained from a patient, each piece was scanned in a separate vial and analyzed individually. Scanning was performed at 3.0 T using a whole-body MRI scanner (GE 750, GE Medical Systems, Milwaukee, WI) with a 32-channel receive head coil. Scans were acquired using a 3D multi-echo bipolar GRE sequence designed for clinical imaging in vivo;²⁸ the sequence includes two 5-echo trains: the

first train was optimized for chemical shift imaging (first echo time (TE) = 3.20 ms, echo spacing = 1.46 ms); the second train was optimized to highlight susceptibility-related contrast (first TE = 16.75 ms, echo spacing = 7.15 ms). The remaining scan parameters were repetition time = 47.6 ms, bandwidth = 142.86 kHz, flip angle = 10°; field of view = 18 cm; matrix size = 192 × 192 × 36, for a final voxel size of 0.94 × 0.94 × 1.0 mm³. Total acquisition time was 5 minutes 33 seconds. A FIESTA-C sequence with identical resolution and bandwidth was also acquired to facilitate thrombus segmentation (TE = 3 ms, TR: 6.1 ms, flip angle: 40°, phase cycles = 4, scan time = 2 min 47 sec). All scans were acquired in the coronal plane, with the phantom lying flat along the MR table and vials aligned perpendicular to B₀. Thrombi sat horizontal relative to the long axis of the vials, and were also aligned perpendicular to B₀.

4.2.3 Image post processing

Raw image data were reconstructed in Matlab (Matlab 8 R2015a; Mathworks, Natick, MA) using the Orchestra Software Development Kit (GE Healthcare; Milwaukee, WI). Complex channel combination was performed using singular value decomposition and phase errors resulting from the bipolar acquisition were removed.²⁹ R₂^{*}, FF and QSM maps were generated using the B0-NICE and MEDI QSM algorithms.^{29,30} Thrombi were segmented semi-automatically on the FIESTA-C images, which are naturally co-registered with the quantitative maps.

4.2.4 Radiomics analysis and machine learning models

A radiomics and machine learning Matlab method previously developed by Vallières et al. was adapted for use in this study.²⁰ The code includes a feature selection portion and a random forest model derivation portion using the selected features. Three random forest classifier models were prepared;

one each using thrombus imaging and patient clinical data only, and one derived from the combined set of imaging and clinical features. For the imaging model, multivariate logistic regression (MLR) as provided in the code was used to select features, while for the clinical model statistical analysis was performed to select features individually based on statistical significance.

4.2.4.1 Feature extraction and selection

To select imaging features, a total of 4 shape (size, volume, solidity, eccentricity) and 43 texture features (supplementary Table 4-1) were extracted from each segmented thrombus' R_2^* , QSM and FF maps. Feature extraction was performed under the possible 8 combinations of the following extraction parameters: 8, 16, 32 or 64 total gray levels, with uniform or equal-probability quantization. Images of a representative thrombus before and after quantization are shown in Figure 4-1. Imaging features were selected using imbalanced-adjusted MLR, where models were derived of 1 to 10 variables (model order) by maximizing the receiver-operating characteristic (ROC) curve using the 0.632+ bootstrap method (AUC_{632+})³¹ to differentiate between CE and LAA stroke.²⁰ Features included in the model with highest AUC_{632+} of the lowest model order were selected to build the imaging random forest model.

For clinical variables, individual clinical parameters found to differ between CE and LAA patients within the training cohort to a level of $P < .1$ were selected as the features for the clinical random forest model. The combined random forest model utilized the selected features from both models.

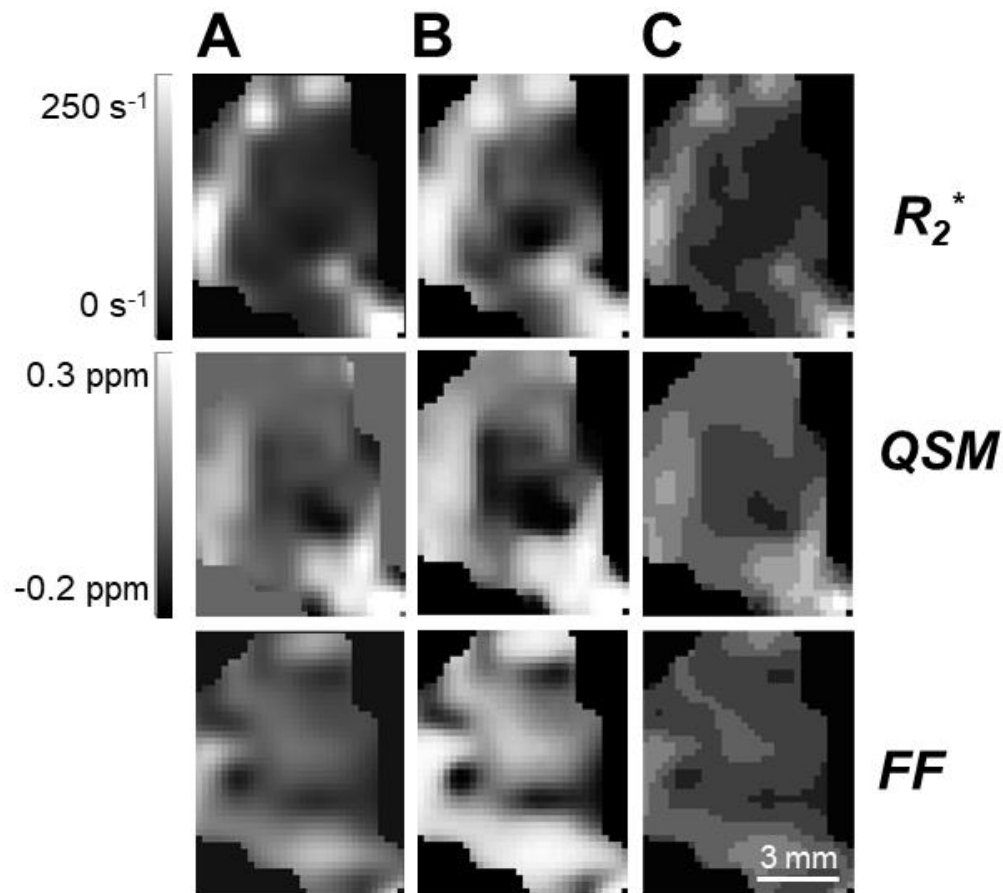


Figure 4-1: Representative segmented thrombus R_2^* (top), QSM (middle) and FF (bottom) images shown in (A) original form, (B) after equal-probability quantization with 64 bins and (C) after uniform quantization with 8 bins. These extraction parameters control the pixel distribution and coarseness under which features are extracted, respectively.

4.2.4.2 Random forest analysis

The random forest classifier was used as it is capable of incorporating numerical and categorical data and has been shown to create highly generalizable models.³² Random forest classifiers were built using 500 trees trained on bootstrapped samples from the training cohort, and were tested on the “out-of-bag” measurements from the training cohort and using all trees on the validation cohort. Overall AUC, sensitivity, specificity and accuracy of the predicted, compared to clinically determined, stroke etiology were recorded for each classifier model.

4.2.5 Statistical analysis

Clinical data are displayed as mean \pm standard deviation and count (percentage) for numerical and categorical variables, respectively. One-way analysis of variance and chi-squared tests were used to assess differences in numerical and categorical clinical variables, respectively, between CE and LAA strokes in the training cohort. Statistical analysis was performed using SPSS (version 23; IBM, Armonk, NY); $P < .05$ was considered statistically significant.

4.3 Results

In this study 128 thrombi were collected from 78 patients, however after excluding patients based on refused consent (n=1), recent prior stroke (n=3) or non-CE or LAA etiology (embolic stroke of undetermined source: n=12; dissection: n=2; unknown: n=2), a total of 91 thrombi from 58 patients were available. 76 thrombi from 49 patients were included in the training cohort while 15 thrombi from 9 patients were included in the validation cohort. Differences in clinical characteristics between CE and LAA stroke within the training cohort are shown in Table 4-2. Patients with CE stroke were significantly older, and had significantly lower incidence of smoking, triglyceride levels and trended towards lower incidence of hemorrhagic transformation; these four variables were selected as features for the clinical random forest model.

Multivariate logistic regression performed on the image features extracted from thrombus R_2^* , QSM and FF maps in the training cohort yielded an optimal model order of 4. The identified features selected for the imaging random forest model and are listed in Table 4-3. Notably, only features from thrombus QSM and FF maps were selected. A CE stroke etiology was

associated with higher skewness in overall QSM values, lower variance in overall FF values, higher variance in QSM gray-level run lengths, and more outliers in QSM size zone matrices. Hence, CE stroke was associated with lower variability in thrombus FF values and higher variability and inconsistency in QSM values.

The performance of the imaging, clinical and combined models for stroke etiology prediction in both cohorts is listed in Table 4-4; respective ROC curves are shown in Figure 4-2. AUC values of each model were always higher when forming predictions on the training cohort than the validation cohort, as expected. Within each cohort, the combined model produced the highest AUC value, followed by the clinical and then image-texture model. The combined classifier achieved an AUC and accuracy of 0.893 and 93%, respectively, for predicting stroke etiology in the validation cohort.

Table 4-2: Clinical details of CE and LAA strokes within the training cohort

Characteristic	CE (n = 41)	LAA (n = 8)	P value
Age (years)	74 ± 15	61 ± 10	0.028
Sex, female	18 (44%)	2 (25%)	0.320
Prior stroke	8 (20%)	2 (25%)	0.725
Prior TIA	2 (5%)	1 (13%)	0.411
Hypertension	30 (73%)	4 (50%)	0.193
Diabetes	5 (12%)	1 (13%)	0.981
Hyperlipidemia	19 (46%)	4 (50%)	0.850
Coronary artery disease	10 (24%)	0 (0%)	0.117
Cardiac valve disease	4 (10%)	0 (0%)	0.357
Peripheral artery disease	3 (7%)	0 (0%)	0.430
Smoking, past 5 years	2 (5%)	3 (38%)	0.005
Past DVT	0 (0%)	0 (0%)	-
Chronic kidney disease	0 (0%)	0 (0%)	-
Obesity	1 (2%)	1 (13%)	0.118
Infection, past 30 days	2 (5%)	0 (0%)	0.524
Active cancer	0 (0%)	0 (0%)	-
Antiplatelets	15 (37%)	4 (50%)	0.476
Anticoagulants	10 (24%)	0 (0%)	0.117
IV rtPA	14 (34%)	4 (50%)	0.395
Hemorrhagic transformation	12 (29%)	5 (63%)	0.071
Stroke recurrence	2 (25%)	5 (12%)	0.344
TICI score:			0.842
0	1 (2%)	0 (0%)	
1	2 (5%)	0 (0%)	
2A	2 (5%)	0 (0%)	
2B	10 (24%)	3 (38%)	
3	26 (63%)	5 (63%)	
Arrival NIHSS (median (IQR))	18 (15.5 - 22.5)	9 (5.25 - 9)	0.361
Occlusion side:			0.680
Right	21 (51%)	3 (38%)	
Left	16 (39%)	4 (50%)	
Unknown	4 (10%)	1 (13%)	
Occlusion site:			0.558
ICA	3 (7%)	0 (0%)	
ICA + MCA M1	7 (17%)	2 (25%)	
MCA M1	18 (44%)	2 (25%)	
MCA M1 + M2	3 (7%)	0 (0%)	
MCA M2	6 (15%)	3 (38%)	
Vertebrobasilar	4 (10%)	1 (13%)	
EVT passes	1.7 ± 1.4	1.7 ± 1.9	0.813
EVT duration (minutes)	54 ± 35	95 ± 41	0.412
Triglycerides (mM/L)	1.3 ± 0.7	3.6 ± 3.2	0.008
Cholesterol (mM/L)	3.6 ± 0.8	5.1 ± 1.3	0.325
HDL (mM/L)	1.0 ± 0.4	0.9 ± 0.3	0.259
LDL (mM/L)	1.9 ± 0.7	2.8 ± 1.0	0.531
Glucose (hemoglobin A1c; %)	5.7 ± 0.7	7.2 ± 2.2	0.276
Leukocytes (10 ⁹ /L)	8.8 ± 2.6	9.2 ± 2.1	0.494
Troponin (ng/L)	47 ± 71	14 ± 12	0.255

Abbreviations: TIA, transient ischemic attack; DVT, deep vein thrombosis; TICI, thrombolysis in cerebral infarction; NIHSS, National Institutes of Health stroke scale; MCA, middle cerebral artery; ICA, internal carotid artery; IV rtPA, intravenous recombinant tissue plasminogen activator; EVT, endovascular therapy; HDL, high-density lipoprotein; LDL, low-density lipoprotein.

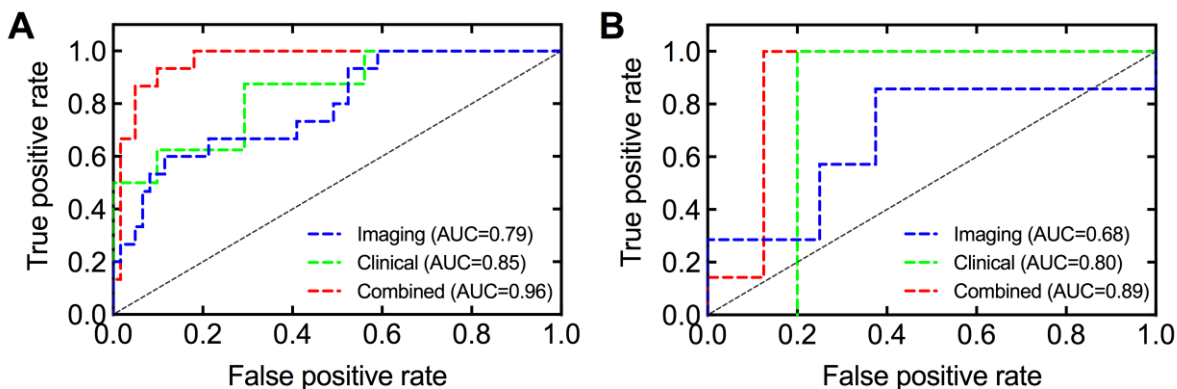
Table 4-3: Thrombus MR imaging texture features selected by MLR for differentiating CE and LAA stroke within the training cohort

Image type	Quantization algorithm	Number of gray levels	Texture type	Texture name
QSM	Equal-probability	16	Global	Skewness
FF	Equal-probability	16	Global	Variance
QSM	Uniform	32	GLRLM	RLV
QSM	Equal-probability	8	GLSZM	GLN

Abbreviations: MLR, multi-variate logistic regression; QSM, quantitative susceptibility mapping; FF, fat fraction; GLRLM, gray-level run-length matrix; RLV, run-length variance; GLSZM, gray-level size zone matrix; GLN, gray-level non-uniformity.

Table 4-4: Performance of random forest classifiers for stroke etiology prediction

Patient cohort	Features used	AUC	Sensitivity (%)	Specificity (%)	Accuracy (%)
Training	Imaging	0.79	66.7	78.7	76.3
	Clinical	0.85	62.5	90.2	83.7
	Imaging + clinical	0.96	87	95.1	93.4
Validation	Imaging	0.68	57.1	75	66.7
	Clinical	0.80	100	80	88.9
	Imaging + clinical	0.89	100	87.5	93.3

**Figure 4-2:** ROC curves for the determination of CE vs. LAA stroke etiology within the training (A) and validation (B) cohorts using the imaging, clinical and combined random forest classifier models.

4.4 Discussion

This study demonstrates the capability of both thrombus MR imaging and patient clinical data features for the prediction of ischemic stroke etiology. Our imaging texture features were derived from thrombi scanned *ex vivo*, obviating the need to perform *in vivo* imaging on vulnerable stroke patients, while all clinical data included in this study can be accessed through a review of patient clinical history, outcome of stroke therapy, and a blood test. Features from each of these data types alone were sufficient to predict stroke etiology with reasonable accuracy, but when combined yielded a model which predicted stroke etiology in an independent test set with a high degree of accuracy.

Thrombus imaging texture models have previously been developed to form predictions related to stroke. Thrombus CT texture features were used in two studies to predict early recanalization following rtPA and EVT therapies, respectively;^{25,26} neither study involved patient clinical data in their analysis. Recently, a study by Chung et al. used features extracted from transverse line profiles of thrombus GRE blooming artifact to predict stroke etiology.³³ This study tested multiple machine learning classifiers and also did not incorporate clinical data. Their highest AUC of 0.93 was reached using random forest and logistic regression models, but achieved accuracies of only 75 and 77%, respectively. Thrombus GRE blooming artifact appearance has been shown to vary between scanners,³⁴ suggesting that measurements obtained from these qualitative images may not be widely generalizable. In contrast, the current study uses features extracted from quantitative MR maps, and incorporates information beyond susceptibility-based information (fat fraction). Multiple studies have examined associations between patient clinical variables and stroke etiology, and older age and lower incidence of smoking have consistently been associated with cardioembolism.³⁵⁻³⁸ These

studies did not assess triglyceride levels or intracerebral hemorrhage occurrence, but separate studies examining hemorrhagic transformation incidence following ischemic stroke treatment have identified lipid levels and etiology as associated risk factors.^{39,40}

In this study we created random classifier models using four imaging, four clinical and eight combined total features. Both the imaging and clinical-only models were able to form accurate predictions of stroke etiology, however the imaging-only model was outperformed by the clinical-only model in both the training and validation cohorts. This suggests that the thrombus texture features may not be as predictive or generalizable as clinical features when considered independently. Conflicting results have been reported on the associations between thrombus composition and etiology,^{3,5,6} which would affect imaging features, while CT texture features have been questioned for their inter-scanner variability and sensitivity to acquisition parameters.⁴¹ Nonetheless, the combined model outperformed both isolated models in the training and validation cohorts, suggesting that the imaging and clinical features provided independent and complimentary information for forming etiology predictions.

Of the thrombus features selected in the imaging model, only features from QSM and FF maps were selected, while R_2^* went unused. Similar to QSM, R_2^* is sensitive to hemoglobin-induced susceptibility effects but holds a quadratic relationship with RBC content, unlike QSM which is linear.^{10,42} It is possible that information derived from thrombus R_2^* pixel distributions is less informative of RBC content than those from QSM, due to similarity in R_2^* values of thrombi in the region between 40-60% RBC content.¹⁰ The higher variance and presence of outliers within QSM values of CE thrombi suggests that their RBCs may be more deoxygenated than those of LAA thrombi. In contrast to R_2^* and QSM, FF provides a unique assessment of thrombus lipid content; the finding of higher variance in FF values of LAA thrombi and

higher triglyceride levels in LAA patients suggests that LAA thrombi may be composed of higher, more variable amounts of lipid due to high triglyceride levels in the blood. The few studies that have identified lipid content within histologically analyzed stroke thrombi have done so exclusively with LAA thrombi.⁴³⁻⁴⁵

For this study, we used *ex vivo* imaging features derived from retrieved stroke thrombi, and clinical features available as part of standard stroke patient assessment. We have therefore demonstrated our models' utility only for *ex vivo* thrombus examination, but with this method it is easier to recruit patients and avoids the challenges associated with scanning acute stroke patients prior to treatment. All clinical features utilized in this paper are readily accessible through a review of patients' clinical history, outcome of stroke treatment, and the results of blood tests. Taken together, all components of the developed models are relatively easily accessible to clinicians, do not require *in vivo* stroke patient scans, and provide accurate predictions of etiology which may enable differentiation of CE and LAA stroke much sooner than with long term electrocardiographic monitoring.

This study has a number of limitations. Our sample size was small, particularly for the validation cohort. Recruitment for this cohort was cut short due to the COVID-19 pandemic, and sample size was further limited by including only patients with known CE or LAA etiologies. Thrombus imaging was conducted *ex vivo*, meaning we cannot assess the capability of this method for *in vivo* scans. Chosen scan parameters and acquisition hardware were selected to be directly translatable to *in vivo* head imaging, and hence were not optimized for *ex vivo* samples. It is possible the retrieved stroke thrombi could have different imaging feature values if scanned *in vivo*, due to the forces exerted on the thrombus by vessel occlusion which may influence texture features, physical alterations to the thrombus during and following the EVT procedure, and differences in temperature and field inhomogeneity

from performing scans *ex vivo*. The fact that only successfully retrieved thrombi were included in the study introduces bias through excluding thrombi which could not be retrieved by EVT or which resolved following rtPA administration. Multiple thrombi retrieved from patients were analyzed separately and treated as independent, though correlation between their imaging values is likely. Assessment of thrombus histological RBC content may have improved model performance but was not included. A prospectively recruited cohort of patients is required to evaluate the clinical utility of the stroke etiology predictions made by the machine learning models.

4.5 Conclusion

In this study, we demonstrated that features derived from *ex vivo* thrombus MR imaging and patient clinical data can be used independently or in combination to differentiate between CE and LAA ischemic stroke. Our combined machine learning model generated highly accurate predictions of stroke etiology, and outperformed the models derived from imaging and clinical data alone. The rapid *ex vivo* imaging protocol and readily available clinical features used in this study makes this method widely applicable for aiding acute ischemic stroke etiology diagnosis.

4.6 References

1. Nam HS, Kim HC, Kim YD, et al. Long-term mortality in patients with stroke of undetermined etiology. *Stroke* 2012;43:2948-2956.
2. Boeckh-Behrens T, Kleine JF, Zimmer C, et al. Thrombus histology suggests cardioembolic cause in cryptogenic stroke. *Stroke* 2016;47:1864-1871.
3. Ahn SH, Hong R, Choo IS, et al. Histologic features of acute thrombi retrieved from stroke patients during mechanical reperfusion therapy. *Int J Stroke* 2016;11:1036-1044.
4. Sporns PB, Hanning U, Schwindt W, et al. Ischemic stroke: what does the histological composition tell us about the origin of the thrombus? *Stroke* 2017;48:2206-2210.
5. Liebeskind DS, Sanossian N, Yong WH, et al. CT and MRI early vessel signs reflect clot composition in acute stroke. *Stroke* 2011;42:1237-1243.
6. Kim S, Yoon W, Kim T, Kim H, Heo T, Park M. Histologic analysis of retrieved clots in acute ischemic stroke: correlation with stroke etiology and gradient-echo MRI. *AJNR Am J Neuroradiol* 2015;36:1756-1762.
7. Shin JW, Jeong HS, Kwon H-J, Song KS, Kim J. High red blood cell composition in clots is associated with successful recanalization during intra-arterial thrombectomy. *PLoS One* 2018;13:e0197492.
8. Brinjikji W, Duffy S, Burrows A, et al. Correlation of imaging and histopathology of thrombi in acute ischemic stroke with etiology and outcome: a systematic review. *J Neurointerv Surg* 2017;9:529-534.
9. Bourcier R, Derraz I, Delasalle B, et al. Susceptibility vessel sign and cardioembolic etiology in the THRACE trial. *Clin Neuroradiol* 2019;29:685-692.
10. Christiansen SD, Liu J, Boffa MB, Drangova M. Simultaneous R2* and quantitative susceptibility mapping measurement enables differentiation of thrombus hematocrit and age: an in vitro study at 3 T. *J Neurointerv Surg* 2019;11:1155-1161.
11. Bourcier R, Pautre R, Mirza M, et al. MRI quantitative T2* mapping to predict dominant composition of in vitro thrombus. *AJNR Am J Neuroradiol* 2019;40:59-64.

12. Brinjikji W, Michalak G, Kadirvel R, et al. Utility of single-energy and dual-energy computed tomography in clot characterization: an in-vitro study. *Interv Neuroradiol* 2017;23:279-284.
13. Borggrefe J, Kottlors J, Mirza M, et al. Differentiation of clot composition using conventional and dual-energy computed tomography. *Clin Neuroradiol* 2018;28:515-522.
14. Shinohara Y, Kato A, Yamashita E, Ogawa T. R2* map by IDEAL IQ for acute cerebral infarction: compared with susceptibility vessel sign on T2*-weighted imaging. *Yonago Acta Med* 2016;59:204.
15. Jagani M, Kallmes DF, Brinjikji W. Correlation between clot density and recanalization success or stroke etiology in acute ischemic stroke patients. *Interv Neuroradiol* 2017;23:274-278.
16. Staessens S, De Meyer SF. Thrombus heterogeneity in ischemic stroke. *Platelets* 2020; doi: 10.1080/09537104.2020.1748586 [Epub ahead of print: 20 Apr 2020].
17. Gillies RJ, Kinahan PE, Hricak H. Radiomics: images are more than pictures, they are data. *Radiology* 2016;278:563-577.
18. Aerts HJWL, Velazquez ER, Leijenaar RTH, et al. Decoding tumour phenotype by noninvasive imaging using a quantitative radiomics approach. *Nat Commun* 2014;5:1-9.
19. Zhou H, Vallières M, Bai HX, et al. MRI features predict survival and molecular markers in diffuse lower-grade gliomas. *Neuro Oncol* 2017;19:862-870.
20. Vallières M, Freeman CR, Skamene SR, El Naqa I. A radiomics model from joint FDG-PET and MRI texture features for the prediction of lung metastases in soft-tissue sarcomas of the extremities. *Phys Med Biol* 2015;60:5471-5496.
21. Kim HS, Kim YJ, Kim KG, Park JS. Preoperative CT texture features predict prognosis after curative resection in pancreatic cancer. *Sci Rep* 2019;9:1-9.
22. Rajini NH, Bhavani R. Computer aided detection of ischemic stroke using segmentation and texture features. *Measurement* 2013;46:1865-1874.

23. Betrouni N, Yasmina M, Bombois S, et al. Texture features of magnetic resonance images: an early marker of post-stroke cognitive impairment. *Transl Stroke Res* 2020;11:643-652.
24. Bretzner M, Lopes R, McCarthy R, et al. Texture parameters of R2* maps are correlated with iron concentration and red blood cells count in clot analogs: a 7-T micro-MRI study. *J Neuroradiol* 2019;47:306-311.
25. Qiu W, Kuang H, Nair J, et al. Radiomics-based intracranial thrombus features on CT and CTA predict recanalization with intravenous alteplase in patients with acute ischemic stroke. *AJNR Am J Neuroradiol* 2019;40:39-44.
26. Hofmeister J, Bernava G, Rosi A, et al. Clot-based radiomics predict a mechanical thrombectomy strategy for successful recanalization in acute ischemic stroke. *Stroke* 2020;51:2488-2494.
27. Adams HP, Bendixen BH, Kappelle LJ, et al. Classification of subtype of acute ischemic stroke. Definitions for use in a multicenter clinical trial. TOAST. Trial of Org 10172 in Acute Stroke Treatment. *Stroke* 1993;24:35-41.
28. Liu J, Christiansen SD, Drangova M. Single multi-echo GRE acquisition with short and long echo spacing for simultaneous quantitative mapping of fat fraction, B0 inhomogeneity, and susceptibility. *NeuroImage* 2018;172:703-717.
29. Liu J, Drangova M. Method for B0 off-resonance mapping by non-iterative correction of phase-errors (B0-NICE). *Magn Reson Med* 2015;74:1177-1188.
30. Liu J, Liu T, de Rochefort L, et al. Morphology enabled dipole inversion for quantitative susceptibility mapping using structural consistency between the magnitude image and the susceptibility map. *NeuroImage* 2012;59:2560-2568.
31. Jiang W, Simon R. A comparison of bootstrap methods and an adjusted bootstrap approach for estimating the prediction error in microarray classification. *Stat Med* 2007;26:5320-5334.
32. Fernández-Delgado M, Cernadas E, Barro S, Amorim D. Do we need hundreds of classifiers to solve real world classification problems? *J Mach Learn Res* 2014;15:3133-3181.

33. Chung JW, Kim YC, Cha J, et al. Characterization of clot composition in acute cerebral infarct using machine learning techniques. *Ann Clin Transl Neurol* 2019;6:739-747.
34. Bourcier R, Détraz L, Serfaty JM, et al. MRI interscanner agreement of the association between the susceptibility vessel sign and histologic composition of thrombi. *J Neuroimaging* 2017;27:577-582.
35. Grau AJ, Weimar C, Buggle F, et al. Risk factors, outcome, and treatment in subtypes of ischemic stroke: the German stroke data bank. *Stroke* 2001;32:2559-2566.
36. Montaner J, Perea-Gainza M, Delgado P, et al. Etiologic diagnosis of ischemic stroke subtypes with plasma biomarkers. *Stroke* 2008;39:2280-2287.
37. Horie N, Tateishi Y, Morikawa M, et al. Acute stroke with major intracranial vessel occlusion: characteristics of cardioembolism and atherosclerosis-related in situ stenosis/occlusion. *J Clin Neurosci* 2016;32:24-29.
38. Pierik R, Algra A, van Dijk E, et al. Distribution of cardioembolic stroke: a cohort study. *Cerebrovasc Dis* 2020;49:97-104.
39. Terruso V, D'Amelio M, Di Benedetto N, et al. Frequency and determinants for hemorrhagic transformation of cerebral infarction. *Neuroepidemiology* 2009;33:261-265.
40. Lee YB, Yoon W, Lee YY, et al. Predictors and impact of hemorrhagic transformations after endovascular thrombectomy in patients with acute large vessel occlusions. *J Neurointerv Surg* 2019;11:469-473.
41. Berenguer R, Pastor-Juan MdR, Canales-Vázquez J, et al. Radiomics of CT features may be nonreproducible and redundant: influence of CT acquisition parameters. *Radiology* 2018;288:407-415.
42. Janick PA, Hackney DB, Grossman RI, Asakura T. MR imaging of various oxidation states of intracellular and extracellular hemoglobin. *AJNR Am J Neuroradiol* 1991;12:891-897.
43. Ogata J, Yutani C, Otsubo R, et al. Heart and vessel pathology underlying brain infarction in 142 stroke patients. *Ann Neurol* 2008;63:770-781.

44. Hashimoto T, Hayakawa M, Funatsu N, et al. Histopathologic analysis of retrieved thrombi associated with successful reperfusion after acute stroke thrombectomy. *Stroke* 2016;47:3035-3037.
45. Donnerstag F, Götz F, Dadak M, et al. Interventional stroke treatment – is it also safe for arteries? Looking at thrombectomy wall damage through clot histology. *Interv Neuroradiol* 2020; doi: 10.1177/1591019920976673 [Epub ahead of print 4 Mar 2021].

4.7 Supplementary material

Supplementary Table 4-1: Texture features used in this study; more detail available in Vallières et al. 2015

Texture type	Texture name
Global	Variance Skewness Kurtosis
Gray-level co-occurrence matrix (GLCM)	Energy Contrast Correlation Homogeneity Variance Sum Average Entropy Autocorrelation
Gray-level run-length matrix (GLRLM)	Short Run Emphasis (SRE) Long Run Emphasis (LRE) Gray-Level Non-uniformity (GLN) Run-Length Non-uniformity (RLN) Run Percentage (RP) Low Gray-Level Run Emphasis (LGRE) High Gray-Level Run Emphasis (HGRE) Short Run Low Gray-Level Emphasis (SRLGE) Short Run High Gray-Level Emphasis (SRHGE) Long Run Low Gray-Level Emphasis (LRLGE) Long Run High Gray-Level Emphasis (LRHGE) Gray-Level Variance (GLV) Run-Length Variance (RLV)
Gray-level size zone matrix (GLSZM)	Small Zone Emphasis (SZE) Large Zone Emphasis (LZE) Gray-Level Non-uniformity (GLN) Zone-Size Non-uniformity (ZSN) Zone Percentage (ZP) Low Gray-Level Zone Emphasis (LGZE) High Gray-Level Zone Emphasis (HGZE) Small Zone Low Gray-Level Emphasis (SZLGE) Small Zone High Gray-Level Emphasis (SZHGE) Large Zone Low Gray-Level Emphasis (LZLGE) Large Zone High Gray-Level Emphasis (LZHGE) Gray-Level Variance (GLV) Zone-Size Variance (ZSV)
Neighbourhood gray-tone difference matrix (NGTDM)	Coarseness Contrast Busyness Complexity Strength

CHAPTER 5

Conclusions and Future Directions

5.1 Conclusions

Stroke thrombus MR imaging has been previously examined as means to provide additional information to improve the treatment of acute ischemic stroke. However, past methods tested *in vivo* have utilized unreliable qualitative metrics, while more advanced, quantitative techniques have thus far been limited almost exclusively to *in vitro* or preclinical experiments. The work of this thesis serves to expand the capability of MR in stroke thrombus imaging, specifically by exploiting quantitative information and advanced artificial intelligence techniques applied to thrombus *ex vivo* images for the prediction of ischemic stroke etiology.

In Chapter 2, I demonstrate that blood clot R_2^* and QSM values are each sensitive to RBC content and oxygenation. This accords with the findings of previous *in vitro* clot studies, however this work was the first to examine these MR parameters on clots of simultaneously varied composition and oxygenation. I show that clot R_2^* and QSM values vary drastically as their oxygenation evolves throughout ageing, and importantly that these changes dominate the inherent differences found between clots of different RBC content. Because of this, the examination of either R_2^* or QSM alone will not be sufficient to determine RBC content in acute stroke thrombi, where oxygenation is never known. I devised a metric using the ratio of clot R_2^* to QSM values and showed that it allowed prediction of RBC content independent of oxygenation, suggesting that a multiparametric approach

may enable accurate RBC content determination in stroke thrombi. Additionally, I demonstrated that FF and QSM mapping are capable of detecting lipidic and calcified components within blood clots, respectively, regardless of composition or oxygenation; the identification of these uncommon components within stroke thrombi would be directly informative of etiology. Overall, this work established the potential of our multiparametric, quantitative MR imaging method for the characterization of ischemic stroke thrombi.

In Chapter 3, I applied a deep learning CNN to *ex vivo* stroke thrombus R_2^* , QSM and GRE images to predict histological RBC content. To my knowledge, this is the first study to use deep learning to analyze MR images of stroke thrombi. I demonstrate that CNNs are capable of leveraging the information available within our multiparametric MR dataset to form accurate predictions of thrombus RBC content, specifically with a mean absolute error of approximately 8%. The small number of thrombi available for this study and the improvements in network accuracy observed when applying data augmentation suggest that greater network performance is achievable if trained on a larger dataset.

Finally, in Chapter 4, I present a machine learning approach employing radiomics texture features extracted from thrombus R_2^* , QSM and FF maps along with clinical patient data to predict stroke etiology. Similar methods have been employed on thrombus CT images to predict response to rtPA and endovascular therapies,^{1,2} however to my knowledge this was the first application of machine learning on thrombus texture features for stroke etiology prediction. The models achieved accurate etiology prediction with AUC and accuracy values of 0.68 and 67%, respectively, using thrombus texture information alone, 0.8 and 89% using clinical information alone, and 0.89 and 93% when using both sets of features. Relative to previous work utilizing qualitative imaging signs for etiology prediction which have

achieved accuracies of 49%,³ and clinical models which have achieved AUC values of 0.85,⁴ the combined model outperformed past attempts and has yielded a novel, promising method to improve clinical etiology determination in acute ischemic stroke.

5.2 Limitations

5.2.1 Analysis of blood clot RBC, lipid and calcium content

The limitations of the study presented in Chapter 2 stem largely from its *in vitro* design; each component included in clot construction was mimicking a pathological human process. In particular, clots were prepared from porcine blood and thus may possess innately different relaxation and susceptibility values than that of human thrombi. Additionally, the mechanisms underlying human thrombus formation are various and complex, and yield thrombi of heterogeneous structure.^{5,6} The clots prepared for this study were comparatively simplistically derived, large and homogeneous in structure.

Another key facet of this study was allowing the initially fully oxygenated arterial clots' oxygenation to change naturally through *in vitro* ageing, which was meant to traverse the breadth of possible oxygenation values observable in human thrombi. While measurement of stroke thrombus oxygenation *in vivo* has not been previously investigated, it is likely to be affected by the environment in which thrombosis occurs, the age of the thrombus prior to embolization, and the duration and severity of the stroke at the time of imaging. It is unlikely that all plausible stroke thrombus oxygenation states were represented through our static *in vitro* clot ageing procedure.

Finally, I used lab materials to represent the lipid and calcified components that can be found within stroke thrombi. Despite similar MR properties, these

materials do not exactly mimic the components found in stroke thrombi, nor is their inclusion as a single large piece of material representative of the all possible component distributions, which may also be diffuse or punctate.

5.2.2 Prediction of stroke thrombus RBC content

The principle limitation of the 3rd Chapter study is that the thrombi were scanned *ex vivo*, following endovascular retrieval, rather than in stroke patients *in vivo*. While our MR sequence was designed for *in vivo* imaging and may be translated without alteration of any sequence parameters, differences in field inhomogeneity, shimming and temperature could all affect observed thrombus MR parameters. Scanning *in vivo* presents additional challenges to scan acquisition including flow artifact and patient movement.

Our study is biased by the ability to only include thrombi retrievable by endovascular therapy, and which did not resolve following rtPA administration if given. As part of the retrieval thrombus breakage or alterations to its size and shape may have occurred which could influence observed MR parameters. Additionally, alterations to thrombus oxygenation or structure can occur during storage, the time between thrombus retrieval and *ex vivo* scanning. Thrombus segmentation was also not fully automatic and additional bias could have been introduced in this step.

The study was further limited by its small sample size. The inclusion of just under 50 thrombi meant that I did not have enough samples to apportion a meaningful test set, and instead used cross-validation to evaluate the network; this may result in overestimation of the generalizability of the model.⁷ Small sample size is a common limitation for deep learning studies in general, which are notorious for using massive datasets to derive generalizable models; the improvements observed when using data

augmentation to increase effective dataset size suggest that a larger sample cohort would be highly beneficial to the performance of the network.

Our study relied on histological analysis to derive ground-truth values of thrombus RBC content. These were derived from a single histology slice and I made the assumption that the measured RBC content was representative of each thrombus overall, and that the RBC content within every MR slice of each thrombus was identical to the histological value.

5.2.3 Prediction of stroke etiology

With the exception of an independent test dataset and the use of histology, all limitations of the study detailed in Chapter 3 also apply to the study described in Chapter 4. This was also an *ex vivo* imaging study, but here radiomics texture features and clinical data were used to form predictions of stroke etiology using machine learning. Radiomics texture features can be influenced by a number of factors including acquisition parameters and the scanner used;⁸ features extracted from *ex vivo* thrombus images may vary from those acquired *in vivo*. As with any machine learning study, model performance is influenced by the particular texture and clinical features chosen *a priori* for study. Sample size is also a limitation (n = 91 thrombi), though more samples were able to be included in this study than that of Chapter 3 because histological analysis was not required.

5.3 Future directions

This thesis presents a quantitative, multiparametric MR technique for thrombus analysis to aid in the treatment and management of acute ischemic stroke. It is motivated by *in vitro* work demonstrating capability of our sequence for thrombus analysis, and is followed by *ex vivo* work

demonstrating utility in human stroke thrombi. Besides translation of the technique to *in vivo* studies to directly assess clinical utility, there are a multitude of additional applications where our quantitative thrombus imaging technique may prove useful, as well as areas where the technique may be improved. These are detailed in the following sections ordered by the types of experiments to be performed.

5.3.1 *In vitro*

Histological studies have reported that CE thrombi have lower RBC content than LAA thrombi,^{9,10} yet MR imaging studies have consistently found a higher presence of susceptibility signs in CE compared to LAA stroke.^{3,11,12} This suggests that, in spite of lower overall RBC content, RBCs in CE thrombi tend to be drastically more deoxygenated than those found in LAA thrombi. Measurement of RBC oxygenation state could therefore provide an additional means to predict stroke etiology which complements assessment of RBC proportion.

Measurement of the T_1 relaxation rate in RBCs can indicate methemoglobin content, one of the two forms of deoxygenated hemoglobin found within thrombi.¹³ Because R_2^* and QSM are sensitive to deoxygenated hemoglobin but insensitive to form (deoxy- or methemoglobin), the addition of the T_1 parameter to the multiparametric analysis may allow explicit determination of the proportions of oxy-, deoxy- and methemoglobin content in thrombi. An *in vitro* blood study which related the MR parameters of oxygenated (arterial), deoxygenated (venous) and methemoglobin-rich (aged) blood to an independent oximetry technique such as blood gas analysis could allow mapping of MR parameters to the amount of each hemoglobin form in blood clots. Applied to stroke thrombi, such analyses may be indicative of thrombus age and provide an additional means to infer etiology. The inclusion of T_1

measurement would require an additional sequence to be added to the protocol however, necessitating increased scan time.

5.3.2 *Ex vivo*

A number of additional parameters related to stroke treatment remain to be studied for associations with thrombus MR imaging. Our technique is sensitive to thrombus RBC content, which has been directly related to response to endovascular therapy (procedure time, number of passes, recanalization score).^{9,14,15} Machine learning applied to CT thrombus texture features, as well as mean thrombus R_2^* values have each been previously used to predict response to endovascular therapy,^{2,16} however multiparametric MRI and more advanced data analysis techniques such as deep learning have not been used for this application and may yield superior predictions. Though likely correlated to therapy response, associations between thrombus properties and long term stroke outcome is an understudied area of research where MR machine learning or deep learning analysis could also be informative.

5.3.3 *In vivo*

Despite demonstrating potential, our study of etiology prediction from thrombus MR features needs to be replicated prospectively *in vivo* to accurately assess its capability to aid in acute ischemic stroke care. MR images from a pilot study showing time of flight (TOF) angiography and R_2^* , QSM and FF maps of an ischemic stroke patient with intracranial thrombus *in vivo* are shown in Figure 5-1. *In vivo* imaging studies additionally enable the study of thrombi which could not be retrieved for *ex vivo* study, allowing associations with complications including secondary embolism or intracerebral hemorrhage, or failed retrieval by endovascular therapy or successful thrombolysis to be drawn. The latter has been examined in

machine learning studies of thrombus CT texture features,^{1,2} but to my knowledge has never been investigated with quantitative MR imaging.

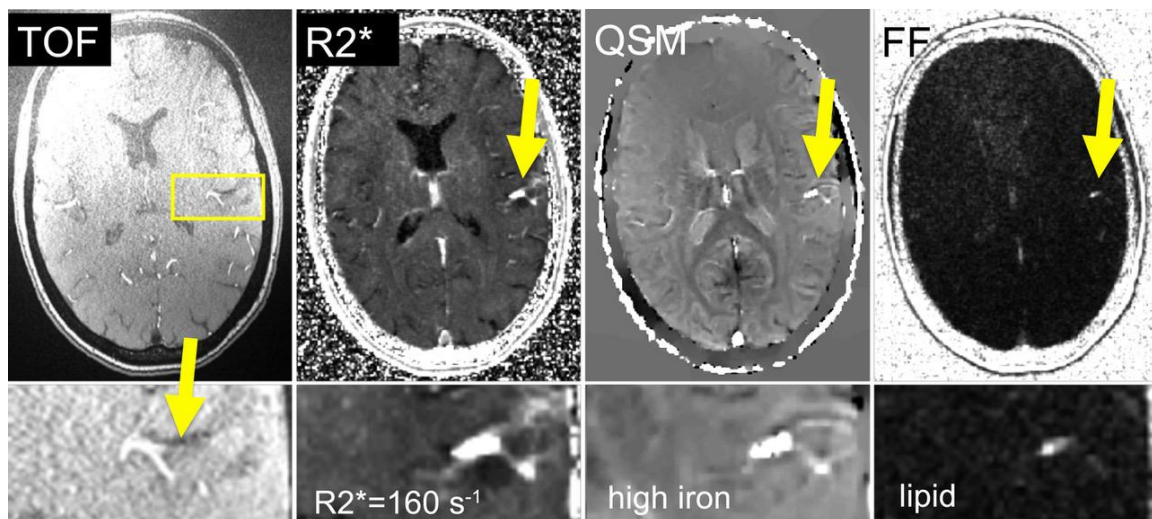


Figure 5-1: Axial time of flight (TOF) angiography, R_2^* , QSM and FF maps of an ischemic stroke patient with intracranial thrombus (arrow) of atherothrombotic origin. High R_2^* and QSM indicate a deoxygenated, RBC-rich thrombus, while a high FF suggests the presence of lipid (from plaque core).

For any *in vivo* analysis technique to be useful in the acute stroke setting, rapid derivation of results is required. To this end, the use of semi-automated segmentation is the biggest limitation of the work described in this thesis; automated *in vivo* thrombus segmentation is a necessary step for the development of a clinically practical thrombus MR analysis tool. Secondary processing steps including the image post-processing required to derive our quantitative MR parameters could be hastened by translating our Matlab code to more efficient programming languages and using more powerful processors for computation. While both machine and deep learning models are computationally expensive to derive, once trained they are extremely efficient for analyzing new data.

Even if a rapid, fully automated thrombus analysis tool existed, ischemic stroke is a challenging application as, in Canada, acute stroke patients are

not typically triaged using MRI. While the utilization of MR imaging in acute ischemic stroke care is expected to increase following recent changes to clinical guidelines,¹⁷ its use is still rare due to its relatively long scan times compared to CT and so additional clinical applications lacking rigid time restrictions should be considered. Thrombus age in deep vein thrombosis influences the success rate of fibrinolysis, but remains challenging to determine;¹⁸ the use of imaging to predict deep vein thrombosis thrombus age is an active area of study that has currently seen little employment of quantitative techniques.¹⁹ Atherosclerotic plaque imaging and cerebral venous thrombosis are other areas where knowledge of associated thrombus age and composition may be useful for determining the course of therapy.

5.4 References

1. Qiu W, Kuang H, Nair J, et al. Radiomics-based intracranial thrombus features on CT and CTA predict recanalization with intravenous alteplase in patients with acute ischemic stroke. *AJNR Am J Neuroradiol* 2019;40:39-44.
2. Hofmeister J, Bernava G, Rosi A, et al. Clot-based radiomics predict a mechanical thrombectomy strategy for successful recanalization in acute ischemic stroke. *Stroke* 2020;51:2488-2494.
3. Bourcier R, Derraz I, Delasalle B, et al. Susceptibility vessel sign and cardioembolic etiology in the THRACE trial. *Clin Neuroradiol* 2019;29:685-692.
4. Kamel H, Navi BB, Parikh NS, et al. Machine learning prediction of stroke mechanism in embolic strokes of undetermined source. *Stroke* 2020;51:e203-e210.
5. Furie B, Furie BC. Mechanisms of thrombus formation. *New Engl J Med* 2008;359:938-949.
6. Staessens S, De Meyer SF. Thrombus heterogeneity in ischemic stroke. *Platelets* 2020; doi: 10.1080/09537104.2020.1748586 [Epub ahead of print: 20 Apr 2020].
7. Dreiseitl S, Ohno-Machado L. Logistic regression and artificial neural network classification models: a methodology review. *J Biomed Inf* 2002;35:352-359.
8. Berenguer R, Pastor-Juan MdR, Canales-Vázquez J, et al. Radiomics of CT features may be nonreproducible and redundant: influence of CT acquisition parameters. *Radiology* 2018;288:407-415.
9. Sporns PB, Hanning U, Schwindt W, et al. Ischemic stroke: histological thrombus composition and pre-interventional CT attenuation are associated with intervention time and rate of secondary embolism. *Cerebrovasc Dis* 2017;44:344-350.
10. Ahn SH, Hong R, Choo IS, et al. Histologic features of acute thrombi retrieved from stroke patients during mechanical reperfusion therapy. *Int J Stroke* 2016;11:1036-1044.
11. Zhang R, Zhou Y, Liu C, et al. Overestimation of susceptibility vessel sign: a predictive marker of stroke cause. *Stroke* 2017;48:1993-1996.

12. Kang D-W, Jeong H-G, Kim DY, Yang W, Lee S-H. Prediction of stroke subtype and recanalization using susceptibility vessel sign on susceptibility-weighted magnetic resonance imaging. *Stroke* 2017;48:1554-1559.
13. Gomori JM, Grossman RI. Mechanisms responsible for the MR appearance and evolution of intracranial hemorrhage. *Radiographics* 1988;8:427-440.
14. Liu M, Hao Z, Li R, Cai J, Jiang C, Li Y. Erythrocyte-rich thrombi related to serum iron contribute to single stent retrieval and favorable clinical outcomes in acute ischemic stroke by endovascular treatment. *Thromb Res* 2020;195:8-15.
15. Shin JW, Jeong HS, Kwon H-J, Song KS, Kim J. High red blood cell composition in clots is associated with successful recanalization during intra-arterial thrombectomy. *PLoS One* 2018;13:e0197492.
16. Bourcier R, Brecheteau N, Costalat V, et al. MRI quantitative T2* mapping on thrombus to predict recanalization after endovascular treatment for acute anterior ischemic stroke. *J Neuroradiol* 2017;44:241-246.
17. Rudkin S, Cerejo R, Tayal A, Goldberg MF. Imaging of acute ischemic stroke. *Emerg Radiol* 2018;25:659-672.
18. Theiss W, Wirtzfeld A, Fink U, Maubach P. The success rate of fibrinolytic therapy in fresh and old thrombosis of the iliac and femoral veins. *Angiology* 1983;34:61-69.
19. Yusof NNM, McCann A, Little PJ, Ta HT. Non-invasive imaging techniques for the differentiation of acute and chronic thrombosis. *Thromb Res* 2019;177:161-171.

APPENDIX A

Copyright Releases

Appendix A.1: Reprint permission- Chapter 1, Figure 1-2

RADIOLOGICAL SOCIETY OF NORTH AMERICA
 820 JORIE BLVD, OAK BROOK, IL 60523
 TEL 1-630-571-2670 FAX 1-630-571-7837
 RSNA.ORG



December 21, 2020

Spencer Christiansen
 London ON N6A 3L9
 Canada

Dear Spencer Christiansen:


The Radiological Society of North America (RSNA®) is pleased to grant you permission to reproduce the following figure in print, electronic and web formats for educational use in your dissertation/thesis, provided you give full credit to the authors of the original publication.

Figure 2
 von Kummer R, Bourguain H, Bastianello S, et al. Early prediction of irreversible brain damage after ischemic stroke at CT. *Radiology* 2001;219:95-100.

This permission is a one-time, non-exclusive grant for English-language use and is exclusively limited to the usage stated and underlined above. The requestor guarantees to reproduce the material as originally published. Permission is granted under the condition that a full credit line is prominently placed (i.e. author name(s), journal name, copyright year, volume #, inclusive pages and copyright holder).

This permission becomes effective upon receipt of this signed contract. Please sign a copy of this agreement, return a signed copy to me and retain a copy for your files. Thank you for your interest in our publication.

[Print Name]: Spencer Christiansen

SIGNATURE:  Date: December 21st, 2020

Sincerely,



Ashley E. Daly
 Senior Manager, Journal Rights & Communications
 Publications



Appendix A.2: Reprint permission- Chapter 1, Figure 1-3

12/16/2020 Rightslink® by Copyright Clearance Center

Copyright Clearance Center RightsLink® Home ? Help Email Support Spencer Christiansen

Enlargement of human cerebral ischemic lesion volumes measured by diffusion-weighted magnetic resonance imaging
 Author: Alison E. Baird, Andrew Benfield, Gottfried Schlaug, et al
 Publication: Annals of Neurology
 Publisher: John Wiley and Sons
 Date: Oct 8, 2004
 Copyright © 1997 American Neurological Association

Order Completed

Thank you for your order.

This Agreement between Western University -- Spencer Christiansen ("You") and John Wiley and Sons ("John Wiley and Sons") consists of your license details and the terms and conditions provided by John Wiley and Sons and Copyright Clearance Center.

Your confirmation email will contain your order number for future reference.

License Number 4971051260869 [Printable Details](#)

License date Dec 16, 2020

Licensed Content		Order Details	
Licensed Content Publisher	John Wiley and Sons	Type of use	Dissertation/Thesis
Licensed Content Publication	Annals of Neurology	Requestor type	University/Academic
Licensed Content Title	Enlargement of human cerebral ischemic lesion volumes measured by diffusion-weighted magnetic resonance imaging	Format	Print and electronic
Licensed Content Author	Alison E. Baird, Andrew Benfield, Gottfried Schlaug, et al	Portion	Figure/table
Licensed Content Date	Oct 8, 2004	Number of figures/tables	1
Licensed Content Volume	41	Will you be translating?	No
Licensed Content Issue	5		
Licensed Content Pages	9		

About Your Work		Additional Data	
Title	Ischemic stroke thrombus characterization through magnetic resonance imaging	Portions	Figure 3
Institution name	Western University		
Expected presentation date	Mar 2021		

12/16/2020

Rightslink® by Copyright Clearance Center

Requestor Location

Tax Details

Requestor Location
[Redacted]
London, ON N6A3L9
Canada
Attn: Western University

Publisher Tax ID EU826007151

Price

Total 0.00 CAD

Would you like to purchase the full text of this article? If so, please continue on to the content ordering system located here: [Purchase PDF](#)
If you click on the buttons below or close this window, you will not be able to return to the content ordering system.

Total: 0.00 CAD


CLOSE WINDOW

ORDER MORE

© 2020 Copyright - All Rights Reserved | Copyright Clearance Center, Inc. | Privacy statement | Terms and Conditions
Comments? We would like to hear from you. E-mail us at customer@copyright.com


Appendix A.3: Reprint permission- Chapter 1, Figure 1-6

12/16/2020 Rightslink® by Copyright Clearance Center



RightsLink®

Home
?
Email Support
Spencer Christiansen ▾



CT and MRI Early Vessel Signs Reflect Clot Composition in Acute Stroke

Author: David S. Liebeskind, Nerses Sanossian, William H. Yong, et al

Publication: Stroke

Publisher: Wolters Kluwer Health, Inc.

Date: Mar 10, 2011

Copyright © 2011, Wolters Kluwer Health

Order Completed

Thank you for your order.

This Agreement between Western University -- Spencer Christiansen ("You") and Wolters Kluwer Health, Inc. ("Wolters Kluwer Health, Inc.") consists of your license details and the terms and conditions provided by Wolters Kluwer Health, Inc. and Copyright Clearance Center.

Your confirmation email will contain your order number for future reference.

License Number 4971050946951 [Printable Details](#)

License date Dec 16, 2020

📄 Licensed Content	📄 Order Details
Licensed Content Publisher Wolters Kluwer Health, Inc.	Type of Use Dissertation/Thesis
Licensed Content Publication Stroke	Requestor type University/College
Licensed Content Title CT and MRI Early Vessel Signs Reflect Clot Composition in Acute Stroke	Sponsorship No Sponsorship
Licensed Content Author David S. Liebeskind, Nerses Sanossian, William H. Yong, et al	Format Print and electronic
Licensed Content Date Mar 10, 2011	Will this be posted online? Yes, on an unrestricted website
Licensed Content Volume 42	Portion Figures/tables/illustrations
Licensed Content Issue 5	Number of figures/tables/illustrations 2
	Author of this Wolters Kluwer article No
	Will you be translating? No
	Intend to modify/change the content No
📄 About Your Work	📄 Additional Data
Title Ischemic stroke thrombus characterization through magnetic resonance imaging	Portions Figures 1 & 2
Institution name Western University	
Expected presentation date Mar 2021	

12/16/2020

Rightslink® by Copyright Clearance Center

Requestor Location

Tax Details

Requestor Location



London, ON N6A3L9
Canada
Attn: Western University

\$ Price

Total 0.00 CAD

Total: 0.00 CAD

CLOSE WINDOW

ORDER MORE

© 2020 Copyright - All Rights Reserved | Copyright Clearance Center, Inc. | Privacy statement | Terms and Conditions
Comments? We would like to hear from you. E-mail us at customercare@copyright.com

Appendix A.4: Reprint permission- Chapter 1, Figure 1-12

Copyright Clearance Center | RightsLink®

Help | Email Support

Haralick texture features from apparent diffusion coefficient (ADC) MRI images depend on imaging and pre-processing parameters

Author: Patrik Brynolfsson et al

Publication: Scientific Reports

Publisher: Springer Nature

Date: Jun 22, 2017

Copyright © 2017, The Author(s)

Creative Commons

This is an open access article distributed under the terms of the [Creative Commons CC BY](#) license, which permits unrestricted use, distribution, and reproduction in any medium, provided the original work is properly cited.

You are not required to obtain permission to reuse this article.
To request permission for a type of use not listed, please contact [Springer Nature](#)

© 2020 Copyright - All Rights Reserved | Copyright Clearance Center, Inc. | [Privacy statement](#) | [Terms and Conditions](#)
Comments? We would like to hear from you. E-mail us at customercare@copyright.com

Appendix A.5: Reprint permission- Chapter 2

Simultaneous $R2^$ and quantitative susceptibility mapping measurement enables differentiation of thrombus hematocrit and age: an in vitro study at 3 T.*

This article has been accepted for publication in Journal of Neurointerventional Surgery (2019) following peer review, and the Version of Record can be accessed online at <http://dx.doi.org/10.1136/neurintsurg-2019-014802>

© BMJ Publishing Group Ltd 2019: Reuse of this manuscript version (excluding any databases, tables, diagrams, photographs and other images or illustrative material included where a another copyright owner is identified) is permitted strictly pursuant to the terms of the Creative Commons Attribution-Non Commercial 4.0 International (CC-BY-NC 4.0) <https://creativecommons.org/licenses/by-nc/4.0/>

APPENDIX B

Ethics Approvals



Date: 6 October 2020

To: Dr. Maria Drangova

Project ID: 106989

Study Title: Ex vivo thrombus imaging using MRI

Reference Number/ID: N/A

Application Type: HSREB Amendment Form

Review Type: Delegated

Full Board Reporting Date: 20October2020

Date Approval Issued: 06/Oct/2020 10:04

REB Approval Expiry Date: 28/Sep/2021

Dear Dr. Maria Drangova ,

The Western University Health Sciences Research Ethics Board (HSREB) has reviewed and approved the WREM application form for the amendment, as of the date noted above.

Documents Approved:

Document Name	Document Type	Document Date	Document Version
ExVivoThrombusImagingUsingMRI REDCap entries 2020-9-16	Other Data Collection Instruments	16/Sep/2020	1
Protocol Ex Vivo - Drangova - 2020-10-2 v.6.2	Protocol	02/Oct/2020	6.2
106989 2019-10-08 v6.2 - 2020-10-2	Protocol - Western	02/Oct/2020	6.2
Telephone Script 2020-10-2	Consent Form	02/Oct/2020	1
Ex Vivo LOI v6 - 2020-10-2	Consent Form	02/Oct/2020	6

Documents Acknowledged:

Document Name	Document Type	Document Date	Document Version
106989 2019-10-08 v6.2 - 2020-10-2 TC	Summary of Changes	02/Oct/2020	6.2
Protocol Ex Vivo - Drangova - 2020-10-2 v.6.2 TC	Summary of Changes	02/Oct/2020	6.2

REB members involved in the research project do not participate in the review, discussion or decision.

The Western University HSREB operates in compliance with, and is constituted in accordance with, the requirements of the TriCouncil Policy Statement: Ethical Conduct for Research Involving Humans (TCPS 2); the International Conference on Harmonisation Good Clinical Practice Consolidated Guideline (ICH GCP); Part C, Division 5 of the Food and Drug Regulations; Part 4 of the Natural Health Products Regulations; Part 3 of the Medical Devices Regulations and the provisions of the Ontario Personal Health Information Protection Act (PHIPA 2004) and its applicable regulations. The HSREB is registered with the U.S. Department of Health & Human Services under the IRB registration number IRB 00000940.

Please do not hesitate to contact us if you have any questions.

Sincerely,

Nicola Geoghegan-Morphet, Ethics Officer on behalf of Dr. Philip Jones, HSREB Vice-Chair

Note: This correspondence includes an electronic signature (validation and approval via an online system that is compliant with all regulations).

APPENDIX C

Curriculum Vitae

Spencer D. Christiansen

Education:

University of Western Ontario, London, Ontario, Canada

CAMPEP combined Ph.D./M.Sc., Medical Biophysics, April 2021

- Research Focus: Quantitative multiparametric MR-based thrombus characterization
- Supervisor: Dr. Maria Drangova

University of Guelph, Guelph, Ontario, Canada

B.Sc., Biophysics, Honours, Co-op, April 2015

Honours and awards:

2019 -2020 Ontario Graduate Scholarship (\$15 000)

2019 ISMRM Educational Stipend (\$720)

2018 Imaging Network of Ontario Oral Presentation,

Honourable Mention (\$100)

2018 ISMRM Educational Stipend (\$720)

2017 Robarts Research Retreat Oral Presentation Award (\$100)

2017 ISMRM Educational Stipend (\$720)

2016 -2017 Canadian Institutes of Health Research (CIHR)

CGS-Masters Scholarship (\$17 500)

2015 -2020 Western Graduate Research Scholarship (\$7800/y)

2015 -2019 Schulich Graduate Scholarship (\$2000/y)

2015 Harold E. Johns Summer Studentship in Medical

Physics (declined)

2014 Outstanding poster presentation at the SickKids Summer

Research Symposium

2012 NSERC Undergraduate Student Research Award (\$4500)

2010-2015 University of Guelph Dean's Honours List

2010 University of Guelph Entrance Scholarship (\$1000)

Employment:

University of Western Ontario, London, Ontario
 Graduate Student Research Assistant (Prof. Maria Drangova)
 May, 2015 - April, 2021

The Hospital for Sick Children, Toronto, Ontario
 Research Assistant (Prof. Giles Santyr)
 May - December, 2014

University of Guelph, Ridgetown Campus, Ridgetown, Ontario
 Lab Technician (Dr. Victor Limay-Rios)
 January - August, 2013

Deep River Science Academy at Atomic Energy of Canada Ltd., Deep River, Ontario
 Research Assistant/Tutor (Dr. Jeremy Pencer)
 May - August, 2012

Journal publications:

1. **Christiansen SD**, Liu J, Bres Bullrich M, Sharma M, Pandey SK, Boulton M, Sposato LA, and M Drangova. "Ex vivo thrombus MR imaging features and patient clinical data enable prediction of acute ischemic stroke etiology." Submitted to *Stroke* April 2021.

2. **Christiansen SD**, Liu J, Bres Bullrich M, Sharma M, Pandey SK, Boulton M, Sposato LA, and M Drangova. "Quantitative prediction of stroke thrombus erythrocyte content from ex vivo multiparametric MRI using deep learning." Submitted to *American Journal of Neuroradiology* March 2021.

3. **Christiansen SD**, Liu J, Boffa MB, and M Drangova. "Simultaneous R2* and QSM measurement enables differentiation of thrombus hematocrit and age: an in vitro study at 3T." *Journal of NeuroInterventional Surgery*, published online May 2019.

4. Liu J, **Christiansen SD**, and M Drangova. "Single multi-echo GRE acquisition with short and long echo spacing for simultaneous quantitative mapping of fat fraction, B0 inhomogeneity, and susceptibility." *NeuroImage* 172 (2018): 703-717.

Refereed abstracts and proceedings:

1. **Christiansen SD**, Liu J, Bres Bullrich M, Sharma M, Pandey SK, Boulton M, Sposato LA, and M Drangova. “Deep learning prediction of retrieved stroke thrombus RBC content using quantitative, multiparametric MRI.” International Society for Magnetic Resonance in Medicine (ISMRM) 29th Annual Meeting, Vancouver, Canada May 2021.

2. Qin E, **Christiansen SD** and M Drangova. “Prediction of stroke thrombus RBC content from multiparametric MRI using machine learning”. Imaging Network of Ontario 19th Annual Symposium, Toronto (remote), Ontario March 2021.

3. **Christiansen SD**, Liu J, Boffa MB, Sposato LA and M Drangova. “Radiomics prediction of ESUS etiology based on ex vivo thrombus analysis using multiparametric quantitative MRI”. European Stroke Organization and the World Stroke Organization Conference, Vienna, Austria (remote) November 2020.

4. **Christiansen SD**, Liu J, Boffa MB, Sposato LA and M Drangova. “Stroke thrombus RBC content and etiology prediction using R2* and susceptibility values ex vivo at 3T”. European Stroke Organization and the World Stroke Organization Conference, Vienna, Austria (remote) November 2020.

5. **Christiansen SD**, Liu J and M Drangova. “Deep learning prediction of stroke thrombus RBC content from multiparametric MRI ex vivo”. Robarts Research Retreat, London, Ontario June 2020.

6. Qin E, **Christiansen SD** and M Drangova. “Investigating stroke origin from thrombus cellular composition”. Robarts Research Retreat, London, Ontario June 2020.

7. **Christiansen SD**, Liu J, Boffa MB, Sposato LA and M Drangova. “Stroke thrombus RBC content and etiology prediction using R2* and susceptibility values ex vivo at 3T”. Imaging Network of Ontario 18th Annual Symposium, London, Ontario March 2020.

8. **Christiansen SD**, Liu J, Boffa MB and M Drangova. "Evaluation of blood clot MR R2* and susceptibility preservation using oxygen-impermeable wrapping and cryogenic storage in vitro at 3T". Robarts Research Retreat, London, Ontario June 2019.

9. **Christiansen SD**, Liu J, Dunmore-Buyze J, Boffa MB and M Drangova. "Comparison of room temperature, refrigerator and cryogenic storage for preservation of blood clot R2* and quantitative susceptibility values in vitro at 3T". International Society for Magnetic Resonance in Medicine (ISMRM) 27th Annual Meeting, Montreal, Canada May 2019.

10. Liu J, Sposato LA, **Christiansen SD** and M Drangova. "Initial experience of imaging stroke patients with a 5-minute whole head multi-echo GRE acquisition". International Society for Magnetic Resonance in Medicine (ISMRM) 27th Annual Meeting, Montreal, Canada May 2019.

11. **Christiansen SD**, Liu J, Boffa MB and M Drangova. "Evaluation of blood clot MR relaxivity and susceptibility preservation using room temperature, refrigerator and cryogenic storage in vitro at 3T". Imaging Network of Ontario 17th Annual Symposium, London, Ontario March 2019.

12. Liu J, **Christiansen SD** and M Drangova. "A study of flip-angle effects in simultaneous quantification of fat fraction, susceptibility and R2*". Imaging Network of Ontario 17th Annual Symposium, London, Ontario March 2019.

13. **Christiansen SD**, Liu J, Boffa MB and M Drangova. "Blood clot hematocrit and age differentiation in vitro using R2* and quantitative susceptibility mapping". Robarts Research Retreat, London, Ontario June 2018.

14. **Christiansen SD**, Liu J, Dunmore-Buyze J, Boffa MB and M Drangova. "Differentiation of blood clot hematocrit and age in vitro using R2* and quantitative susceptibility mapping at 3T ". International Society for Magnetic Resonance in Medicine (ISMRM) 26th Annual Meeting, Paris, France June 2018.

15. Liu J, **Christiansen SD** and M Drangova. "Simultaneous quantification of fat fraction, susceptibility and R2* from a single GRE

acquisition: flip-angle effects”. International Society for Magnetic Resonance in Medicine (ISMRM) 26th Annual Meeting, Paris, France June 2018.

16. **Christiansen SD**, Liu J, Boffa MB and M Drangova. “Blood clot hematocrit and age differentiation in vitro using R2* and quantitative susceptibility mapping”. London Health Research Day, London, Ontario May 2018.

17. **Christiansen SD**, Liu J, Boffa MB and M Drangova. “Blood clot hematocrit and age differentiation in vitro using R2* and quantitative susceptibility mapping”. Imaging Network of Ontario 16th Annual Symposium, Toronto, Ontario March 2018.

18. **Christiansen SD**, Liu J, Boffa MB, Sposato LA and M Drangova. “In vitro blood clot composition characterization by quantitative MRI”. 12th Annual London Imaging Discovery Day, London, Ontario June 2017.

19. **Christiansen SD**, Liu J, Boffa MB, Sposato LA and M Drangova. “In vitro blood clot composition characterization by quantitative MRI”. Roberts Research Retreat, London, Ontario June 2017.

20. Liu J, Sposato LA, Whelan T, **Christiansen SD** and M Drangova. “A 5-minute multi-echo GRE acquisition for multi-parametric imaging”. 12th Annual London Imaging Discovery Day, London, Ontario June 2017.

21. **Christiansen SD** Liu J, Wade T, Dunmore-Buyze J, Boffa MB, Sposato LA and M Drangova. “Quantitative characterization of calcified and lipid-laden blood clot in vitro at 3T”. International Society for Magnetic Resonance in Medicine (ISMRM) 25th Annual Meeting, Honolulu, United States April 2017.

22. **Christiansen SD**, Liu J, Boffa MB, Sposato LA and M Drangova. “Quantitative MR characterization of calcified and lipid-laden blood clot in vitro at 3T”. Imaging Network of Ontario 15th Annual Symposium, London, Ontario March 2017.

23. **Christiansen SD**, Liu J, Boffa MB, Sposato LA and M Drangova. “Quantitative magnetic resonance characterization of calcified and lipid-

laden blood clot in vitro at 3T". London Health Research Day, London, Ontario March 2017.

24. **Christiansen SD**, Liu J and M Drangova. "Effect of in vitro blood clot hematocrit and age in quantitative R2* MRI mapping". Robarts Research Retreat, London, Ontario June 2016.

25. **Christiansen SD**, Liu J and M Drangova. "Effect of in vitro blood clot hematocrit and age in quantitative R2* MRI mapping". London Health Research Day, London, Ontario March 2016.

26. **Christiansen SD**, Kanhere N, Lindenmaier A, Zanette B and G Santyr. "Mapping hyperpolarized ^{129}Xe polarization losses in the magnetic field of a 1.5T MRI system". The SickKids Summer Research Program Symposium, Toronto, Ontario August 2014.

Supervisory and volunteer experience:

Undergraduate 3rd and 4th year research project mentor

Supervised a Western medical biophysics undergraduate student for their 3rd year, summer and 4th research projects
January 2020 - April 2021

Western National Scholarship application ranking volunteer

Read essays and ranked high school student applications for prestigious Western entrance scholarships
February, 2020

M. M. Robinson High School, Burlington, Ontario

Guest lecture (Grade 10 Science Academic)
May, 2018